Micromachined 30 K Joule-Thomson cryogenic cooler

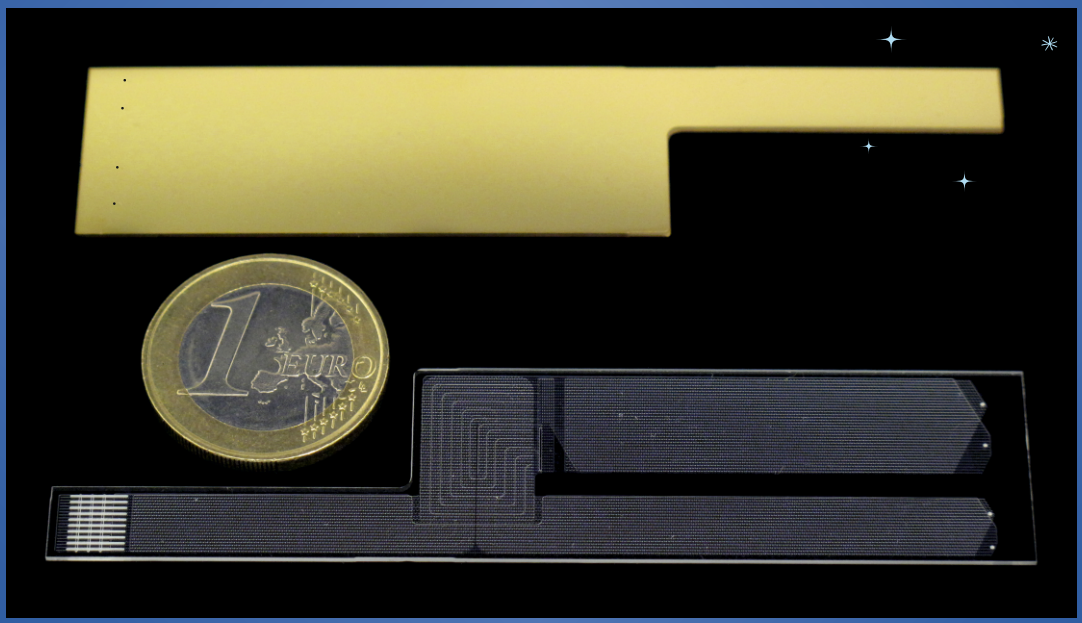

Haishan Cao

MICROMACHINED 30 K JOULE-THOMSON CRYOGENIC COOLER

Haishan Cao

Ph.D. committee:

Chairman:

prof. dr. G. van der Steenhoven	University of Twente

Promotor:

prof. dr. ir. H.J.M. ter Brake	University of Twente

Assistant promotor:

dr. ir. S. Vanapalli	University of Twente

Members:

prof. dr. D. Lohse	University of Twente
prof. dr. M.C. Elwenspoek	University of Twente
prof. dr. A.T.A.M. de Waele	Eindhoven University of Technology
prof. dr. J.G.E. Gardeniers	University of Twente
prof. dr. ir. T.H. van der Meer	University of Twente

Frontcover: An image of two-stage microcoolers with and without a gold layer. The ice crystal background designed by Ce Bian.
Backcover: A sequence of six images showing the declogging phenomenon in the restriction of a microcooler.

This research is supported by the Dutch Technology Foundation STW, which is part of the Netherlands Organisation for Scientific Research (NWO) and partly funded by the Ministry of Economic Affairs (project number 08014). It was carried out at the Energy, Materials and Systems group (EMS) of the Faculty of Science and Technology of the University of Twente.

Micromachined 30 K Joule-Thomson cryogenic cooler
H.S. Cao
Ph.D. thesis, University of Twente, Enschede, the Netherlands
ISBN: 978-90-365-0139-2
Printed by Ipskamp Drukkers, Enschede, the Netherlands

MICROMACHINED 30 K JOULE-THOMSON CRYOGENIC COOLER

DISSERTATION

to obtain
the degree of doctor at the University of Twente,
on the authority of the rector magnificus,
prof. dr. H. Brinksma,
on account of the decision of the graduation committee,
to be publicly defended
on Wednesday, 02 October 2013, at 14:45

by

Haishan Cao

Born on 09 November 1981
in Inner Mongolia, China

This dissertation has been approved by:
Promotor: prof. dr. ir. H.J.M. ter Brake
Assistant promotor: dr. ir. S. Vanapalli

To my parents

Nomenclature

Symbol	Meaning	Unit
A	Area	[m^2]
$A_{\perp}$	Cross sectional area of the CFHX body	[m^2]
$A_{\|\|}$	Contact area between fluid and material element	[m^2]
c	Concentration	[Pa m^3 m^{-3}]
c_p	Specific heat capacity	[J kg^{-1} K^{-1}]
C	Constant	[-]
C	Heat capacity	[J K^{-1}]
COP	Coefficient of performance	[-]
D	Diffusivity	[m^2 s^{-1}]
D_h	Hydraulic diameter	[m]
E	Activation energy of desorption	[J mol^{-1}]
f	Darcy-Weisbach friction factor	[-]
f	Frequency	[Hz]
f_T	Intrinsic cut-off frequency	[Hz]
g_{ds}	Drain-to-source conductance	[S]
h	Convective heat transfer coefficient	[W m^{-2} K^{-1}]
h	Height	[m]
h	Specific enthalpy	[J kg^{-1}]
$\dot{H}$	Enthalpy flow rate	[W]
k_B	Boltzmann constant	[J K^{-1}]
K	Permeability	[$Pa^{0.5 \text{ or } 0}$ m^2 s^{-1}]

Symbol	Meaning	Unit
l	Length	[m]
L_F	Flow entrance length	[m]
L_T	Thermal entrance length	[m]
$\dot{m}$	Mass-flow rate	[kg s^{-1}]
M	Molar mass	[kg mol^{-1}]
N	Surface density of water molecules	[molecules m^{-2}]
Nu	Nusselt number	[-]
$\dot{n}_{dep}$	Deposition rate	[mol m^{-2} s^{-1}]
O	Perimeter	[m]
p	Pressure	[Pa]
p_r	Reduced pressure	[-]
Pr	Prandtl Number	[-]
$\dot{Q}$	Heat-flow rate	[W]
$\dot{Q}$	Gas-flow rate per unit area	[Pa m^3 m^{-2} s^{-1}]
r_t	Total resistance	[ohm]
R	Thermal resistance	[K W^{-1}]
R	Universal gas constant	[J K^{-1} mol^{-1}]
Re	Reynolds number	[-]
s	Specific entropy	[J kg^{-1} K^{-1}]
S	Pumping speed	[m^3 s^{-1}]
t	Thickness	[m]
t	Time	[s]
T	Temperature	[K or °C]
T_d	Drain temperature	[K]
T_g	Gate temperature	[K]
T_{min}	Minimum noise temperature	[K]
U	Overall heat transfer coefficient	[W m^{-2} K^{-1}]
v	Mean fluid velocity	[m s^{-1}]
V	Volume	[m^3]
w	Width	[m]
Z_0	Characteristic impedance	[ohm]
Greek symbols		
α	Accommodation coefficient	[-]
α	Thermal diffusivity	[m^2 s^{-1}]
δ	Thickness	[m]
ε	Emissivity	[-]
ε	Lennard-Jones 12-6 potential characteristic energy	[J]
ε	Porosity	[-]
ε_r	Dielectric constant	[-]
γ	Ratio of the isobaric and isochoric specific heat capacity	[-]
λ	Thermal conductivity	[W m^{-1} K^{-1}]

Symbol	Meaning	Unit
μ	Dynamic viscosity	[Pa s]
μ_{JT}	Joule-Thomson coefficient	[K Pa^{-1}]
ν	Kinematic viscosity	[m^2 s^{-1}]
ρ	Density	[kg m^{-3}]
σ_B	Stefan-Boltzmann constant	[W m^{-2} K^{-4}]
τ_0	Nominal period of vibration	[s]
ω	Acentric factor	[-]
Ω_D	Collision integral for diffusion	[-]
Subscripts and superscripts		
I	CFHX I	[-]
II	CFHX II	[-]
III	CFHX III	[-]
a	Ambient	[-]
ave	Average	[-]
b	Channel boundary	[-]
c	Channel center	[-]
c	Conduction	[-]
c	Cold fluid	[-]
crit	Critical point	[-]
csg	Conduction via the surrounding gas	[-]
cross	Cross section	[-]
d	Diffusivity	[-]
evap	Evaporator	[-]
evapI	Evaporator I	[-]
evapII	Evaporator II	[-]
gross	Gross cooling power	[-]
gw	Convection from gas to wall	[-]
h	Hot fluid	[-]
h	Isenthalpic	[-]
k	Permeability	[-]
ms	Microstrip	[-]
in	Inlet	[-]
out	Outlet	[-]
p	Permeation	[-]
pH	High-pressure channel	[-]
pL	Low-pressure channel	[-]
pre	Pre-cooler	[-]
rad	Radiation	[-]
sat	Saturation	[-]
sl	Stripline	[-]
w	Wall or wetted area	[-]
wg	Convection from wall to gas	[-]

Contents

CHAPTER 1

Introduction

In this introductory chapter, the motivation of the research on miniaturization of Joule-Thomson (JT) cryocoolers is given. The concept of JT cooling is provided along with a brief theoretical overview. Furthermore, the development of miniaturization of JT cryocoolers is described, followed by the outline of this thesis.

1.1 Motivation and research description

Zora Neale Hurston, American writer and folklorist once said, “Research is formalized curiosity. It is poking and prying with a purpose.” So what is the purpose of the research described in this thesis — microcooling? Many electronic devices such as infrared detectors [1] and low-noise amplifiers [2] could benefit from operating at cryogenic temperatures, typically below 120 K [3]. For these electronic devices, colder is better. Besides, cryogenic temperatures also can offer some unique capabilities to superconducting devices [4], which are not available at ambient temperature. Unfortunately, existing cryogenic coolers (cryocoolers) are very large compared to sizes of these devices to be cooled and mismatch small cooling power requirements of these devices [5]. There are many applications where the performance improvement gained by cooling the device is overruled by the effort and complexity of the cryogenic burden caused by the relatively large cryocooler. Widespread use of these electronic devices requires cryocoolers that have small dimensions and cooling capacities [6]; in addition, miniature cryogenic coolers need to become cheaper and more reliable. Addressing this challenge, the miniaturization of Joule-Thomson (JT) cryocoolers has been investigated at the University of Twente for many years. In 1995, Burger et al. [7] started to explore the possibilities of designing miniaturized JT cryocoolers using Micro-Electro-Mechanical Systems (MEMS) technology and built a 165 K closed cycle JT cooler driven by a sorption compressor. The cooler operated with ethylene gas and had a cooling power of about 200 mW at 169 K. From 2002 to 2007, Lerou et al. [8] realized 100 K micromachined JT cryocoolers that were fabricated by using only MEMS technology. The utilization of the 100 K microcoolers for cooling small detector systems in future space missions was investigated by Derking et al. [9]. As a follow-up, the subject of this thesis is devoted to the realization of micromachined two-stage 30 K JT cryocoolers.

1.2 Cryogenic coolers

In 2012, I had an opportunity to attend the European Course of Cryogenics. During a lecture in Dresden University of Technology, Professor Hans Quack asked us: what did Socrates, Leonardo da Vinci and Goethe have in common? One answer among others to the question is that they did not know what a refrigerator is and how one can produce refrigeration. The science of refrigeration just begun to develop until the first and second laws of thermodynamics emerged simultaneously in the 1850s [10]. The task of refrigeration is to cool an object to a temperature below ambient temperature and to keep it at such a low temperature even if there is some heat leak from the outside or internal heat sources. Cryocoolers are refrigerators capable of providing refrigeration at cryogenic temperatures (typically 120 K or lower). The cooling principles of the cryocoolers are based on different thermodynamic cycles [11].

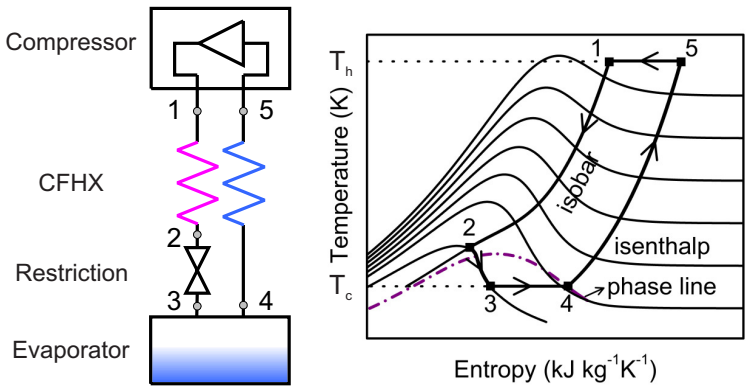

Figure 1.1: Schematic of the Linde-Hampson cooling cycle (left) and corresponding temperature versus entropy diagram (right).

A JT cryocooler is based on the Linde-Hampson cycle (see Figure 1.1). High-pressure gas undergoes JT expansion [12] when it flows through a restriction resulting in a lower temperature of the gas. The low-pressure cold gas then flows through a counter flow heat exchanger (CFHX) thereby cooling the high-pressure gas flowing in the opposite direction towards the restriction. In the steady state operation, the high-pressure gas upon JT expansion produces liquid, which is contained in the evaporator. The devices mounted on the evaporator can then be cooled by evaporation of the condensed liquid. The evaporated working fluid returns through the low-pressure line of the CFHX.

The cold-end temperature of a JT cryocooler is determined by the boiling temperature of the gas at the low pressure of the evaporator. Table 1.1 shows the normal boiling points (boiling temperature at 0.10 MPa) of a few different gases. The gross cooling power refers to the change in enthalpy of the gas at the cold end. In an ideal CFHX, the enthalpy released by the high-pressure gas is totally absorbed by the low-pressure gas in the CFHX, that is, $\Delta h_{1,2} = \Delta h_{5,4}$. The enthalpy of the gas flowing through the restriction remains constant when the process of expansion of the gas is carried out adiabatically. Therefore, the change in specific enthalpy of the gas at the warm end of the first stage ($\Delta h_{5,1}$) equals that at the cold end ($\Delta h_{4,3}$). The gross cooling power of the first stage ($\dot{Q}_{gross}$) is defined by:

$$\dot{Q}_{gross} = \dot{m}\Delta h_{4,3} = \dot{m}\Delta h_{5,1} \tag{1.1}$$

where $\dot{m}$ is the mass-flow rate.

A disadvantage of the JT expansion is that cooling only occurs if the initial temperature of the gas, prior to expansion, is below the inversion temperature of the gas. The inversion temperature is the temperature where the JT coefficient (μ_{JT}) is zero. The

Table 1.1: Normal boiling points and maximum inversion temperatures of different gases [13, 14].

Gas	Normal boiling point (K)	Maximum inversion temperature (K)
Methane	111.5	939
Oxygen	90.1	761
Argon	87.2	794
Carbon monoxide	81.5	652
Nitrogen	77.2	621
Neon	27.1	250
Hydrogen	20.3	205
Helium 4	4.2	40

JT coefficient of a gas is the change in temperature resulting from an isenthalpic pressure drop, which is defined as follows:

$$\mu_{JT} = (\partial T/\partial p)_h \tag{1.2}$$

The maximum inversion temperature is about 10 times the normal boiling point of the gas as shown in Table 1.1. In order to reach temperatures near the normal boiling points of neon, hydrogen or helium in a JT cryocooler starting from ambient temperature, a multi-stage JT cryocooler is required.

1.3 Miniaturization of JT cryogenic cooler

JT cryocoolers are suitable for miniaturization because they have no cold moving parts and therefore can be scaled down to match sizes and power consumptions of devices to be cooled. Several studies on the miniaturization of JT cryocoolers deal with the optimization of the CFHX and the various techniques for manufacturing the cold stage [15–22]. MEMS technology has been identified as one of the most promising technologies in this respect because of its high fabrication accuracy and possibility of batch processing. Garvey et al. [16] developed the first micromachined JT cryocooler. They fabricated the microcooler out of glass wafers using an abrasive etching process. Their microcooler operated with nitrogen gas and produced a cooling power of 25 mW at 88 K. Lerou et al. [22] designed microcoolers (see Figure 1.2) with cooling power ranging from 10 to 25 mW at about 100 K with nitrogen gas as the working fluid. Their microcoolers were optimized for the maximum performance in combination with the minimum size by minimizing the entropy generation of the CFHX [20].

Recent research topics of microcooling include the use of a gas mixture as the working fluid, a tunable JT restriction for flow modulation and multi-stage cooling to reach lower temperatures. Compared to pure gas, mixed gases provide an equivalent cooling power

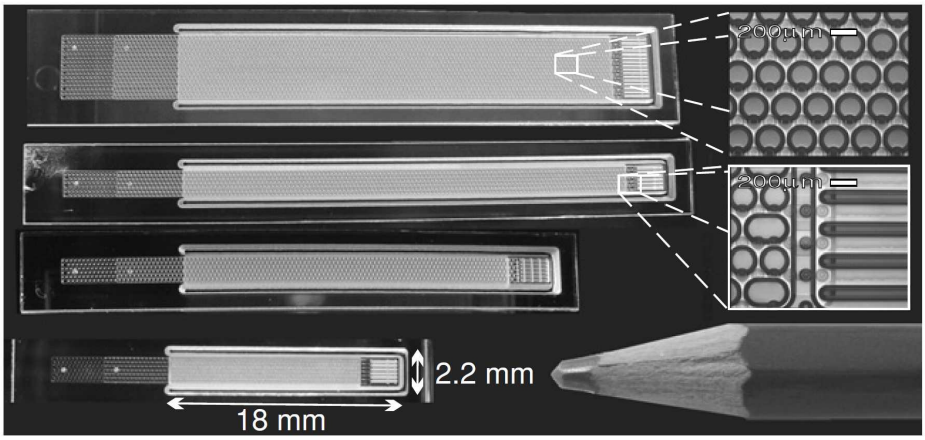

Figure 1.2: Four different micro cryogenic cold stages (left). Magnification of the micro channel with supporting pillars (top right). The end of the high-pressure flow channel, the flow restriction and a part of the evaporator (middle right) [21].

with a significantly lower pressure ratio. Lin et al. [23] used a five-component mixture in a glass capillary microcooler. At a precooling temperature of 240 K, the cold head reached a stable temperature of 140 K with low and high pressures of 0.07 and 1.4 MPa respectively. A tunable JT restriction facilitates the adjustment of the cooling power during steady operation, as well as adapting it during the cool-down of the microcooler. Park et al. [24] developed a piezoelectrically actuated microvalve with dimensions of 1 x 1 x 1 cm^3 for flow modulation at cryogenic temperatures. Zhu et al. [25] used this microvalve in a JT cooling system as a tunable restriction with a silicon/glass heat exchanger. They modulated an ethane gas flow between 80 and 100 mg s^{-1} with the cooler operating between 0.10 and 0.53 MPa. When the restriction was fully open, the cooler provided cooling powers of 75 mW at 255 K and 150 mW at 258 K. The experimental cool-down time of the JT cooling system was longer than the expected value because the thermal mass of the whole system was large compared to the cooling power. Further improvement in the integration of the tunable restriction and the heat exchanger is still necessary to eliminate the accompanying tubing and fittings to reduce the total thermal mass. To reach temperatures lower than the normal boiling point of nitrogen (77 K), it is necessary to use a multi-stage microcooler. In this thesis we present a two-stage JT microcooler operating at 30 K. The microcooler is fabricated by etching microstructures in glass wafers that are later stacked and bonded together. Bonding the stack is a crucial step and the yield in the production as well as the reliability in operation reduces drastically with increasing number of wafers in the stack. A seven-wafer stack two-stage JT cryocooler operating at 14 MPa was presented by Little [26]. He affirmed

that seven-wafer stack two-stage cryocoolers are much more difficult to fabricate with acceptable yields and good efficiency than his earlier single-stage cryocoolers built from a four-wafer stack [27]. Furthermore, high gas pressures add more stringent requirements to the bonding process and severely add complexity to the development of a compressor for closed-cycle operation of the cryocooler. The two-stage JT microcooler described here operates with modest pressures, which is realized in a stack of only three wafers.

1.4 Outline

The work that is described in this thesis focuses on the realization and utilization of a two-stage JT microcooler operating at 30 K. This thesis includes the following aspects:

- Theory and design (chapter 2);
- Fabrication and application demonstration (chapter 3);
- Characterization (chapter 4);
- Clogging phenomenon and mechanism analysis (chapter 5);
- Utilization for cooling low noise amplifiers (chapter 6);
- Long-life micro vacuum packaging (chapter 7);
- Improvement in CFHX performance (chapter 8).

In chapter 2, the optimum working fluids for both stages of the microcooler are selected by maximizing the coefficient of performance (COP) of the microcooler. A finite-element dynamic model with lumped evaporators and pre-cooler is developed for analyzing the microcooler performance and to optimize the microcooler dimensions.

The fabrication of the two-stage microcooler is briefly introduced in chapter 3. In addition, the application potential of the microcooler coupled with electronic devices is demonstrated by cooling an YBCO film through its superconducting phase transition.

Chapter 4 discusses the characterization of the microcooler. Experimental results on cool down and cooling power are compared to dynamic modeling predictions.

A critical issue for long-term operation of the microcooler is the clogging of the nitrogen stage caused by the deposition of water molecules. Based on the fact that the microcooler is made of transparent glass wafers, the deposition of water molecules and subsequent sublimation during the cryogenic operation of the microcooler could be imaged with a microscope and a high resolution camera. Results are discussed in chapter 5. These phenomena are explained by considering the combined effects of diffusion and kinetic process of water molecules.

At low temperatures, low-noise amplifiers operate with a higher signal-to-noise ratio than they do at room temperature. The utilization of microcoolers in cooling of low-noise amplifiers is discussed in chapter 6.

The microcooler needs a vacuum environment to minimize the heat loss due to heat flux via the surrounding gas. For the measurements described in this thesis, the microcooler was placed in a glass vacuum chamber with a turbo-molecular pump connected directly to it. To develop a compact, stand-alone system, the microcooler with the device to be cooled will be integrated with a micro vacuum chamber that is initially pumped to high vacuum and then sealed. In chapter 7, the possible sources of gas and the mechanisms that may cause a pressure increase in the vacuum packaging are discussed theoretically. The results can be used to guide the design of a long lifetime micro vacuum chamber without continuous mechanical pumping.

The CFHX is an essential component of the microcooler. To withstand the high pressure inside the CFHX, pillar matrices are placed in the channels of the CFHX to control the mechanical stress within limits. In chapter 8, the thermal and hydraulic performance of the channels with pillar matrices are investigated numerically, and a better flow pattern is suggested to improve the microcooler performance.

Chapter 9 presents the recommendations for future work on microcooling.

CHAPTER 2

Theory and design

In this chapter, the fluid dynamics and the heat transfer related to the performance of JT microcoolers are introduced. The conceptual design of a a two-stage JT microcooler is discussed and the working fluids are optimized by maximizing the coefficient of performance (COP) of the microcooler. The optimization of the microcooler dimensions is described based on a dynamic model. Furthermore, the discussion focuses on the cooler performance with optimized geometry and using nitrogen and hydrogen as the working fluids.

2.1 Fluid dynamics and heat transfer

2.1.1 Knudsen number

In order to describe the rarefaction of gas flow, a dimensionless parameter called Knudsen number is used. It is defined as the ratio between the molecular mean free path and the characteristic flow dimension such as hydraulic diameter. Based on the Knudsen number, the flow can be divided into various regimes as shown in Table 2.1 [28]. In the continuum regime ($Kn < 0.001$), Navier-Stokes equation based on the continuum assumption is adequate to model the fluid behavior. In the slip-flow regime ($0.001 < Kn < 0.1$), the continuum model can be used with the application of the slip/jump boundary conditions. The slip/jump boundary conditions refer to circumstances in which the tangential velocity of the fluid at the wall is not the same as the wall velocity and the temperature of the fluid next to the wall is not the same as the wall temperature. If the flow is in the transition regime ($0.1 < Kn < 10$), the Navier-Stokes equation is not valid, and molecular-based models such as Direct Simulation Monte Carlo (DSMC) or Boltzmann transport equations should be used. In the free molecular flow regime ($Kn > 10$), the collision between molecules can be neglected and collisionless Boltzmann transport equations can be used [29]. In the microcoolers described in this thesis, the minimum pressure of the gas inside is 0.10 MPa. The mean free path of nitrogen gas at 300 K and 0.10 MPa is about 100 nm, and it reduces with decreasing temperature and increasing pressure. The minimum characteristic flow dimension of the microcoolers is 2.2 μm. Therefore, the maximum Knudsen number is about 0.045, and the Navier-Stokes and energy equations can be used to estimate the performance of the microcoolers.

Table 2.1: Flow regimes based on the Knudsen number [30].

Regime	**Method of calculation***	**Kn range**
Continuum	Navier-Stokes and energy equations with no-slip/no-jump boundary conditions	$Kn < 0.001$
Slip flow	Navier-Stokes and energy equations with slip/jump boundary conditions, DSMC	$0.001 < Kn < 0.1$
Transition	DSMC, BTE	$0.1 < Kn < 10$
Free molecule	DSMC, BTE	$Kn > 10$

* DSMC=direct simulation Monte Carlo, BTE=Boltzmann transport equations.

2.1.2 Reynolds number

The Reynolds number is the ratio of inertial forces to viscous forces and is given by:

$$Re = \frac{\rho v D_h}{\mu} \tag{2.1}$$

where ρ, v and μ are the density, the mean velocity and the dynamic viscosity of the fluid, respectively. D_h is the hydraulic diameter of the channel, defined as:

$$D_h = \frac{4A_{cross}}{O} \tag{2.2}$$

where A_{cross} is the cross sectional area and O is the perimeter of the channel.

The Reynolds number is used to determine if the flow is laminar, transient or turbulent. In laminar flow, the fluid moves in smooth layers or lamina. Turbulent flow is characterized by unsteady mixing due to eddies. Transient flow is a mixture of laminar and turbulent flow, with turbulence in the center of the channel, and laminar flow near the boundaries. According to typical macro-scale fluid theory, a flow is laminar if the Reynolds number is less than 2300 and is turbulent if it is greater than 4000 [31]. Some studies indicate that the transition from laminar to turbulent flow in microchannel occurs when the Reynolds number is lower than 2300 [32–35]. Hetsroni et al. [36] compared numbers of experimental data and considered one main reason of the early transition from laminar to turbulent flow in microchannel is the relative surface roughness. In general, the flow regime can be determined based on the dependence of the friction factor on the Reynolds number as discussed below.

The pressure drops in microcoolers affect their cold-end temperatures and powers consumed by compressors in closed cycles. The pressure drop of internal incompressible fully developed flow in a channel with a length, l, can be calculated using the Darcy-Weisbach equation:

$$\Delta p = 0.5 f \rho v^2 \frac{l}{D_h} \tag{2.3}$$

where f is the Darcy-Weisbach friction factor.

For fully developed laminar, one-phase flow in a channel, the friction factor depends only on Re, given by:

$$f = \frac{C}{Re} \ (Re < 2300) \tag{2.4}$$

The constant C depends on the cross sectional shape of the channel [31]. For parallel plates C = 96, for a circular channel C = 64 and for a square channel C = 57.

In the transient and turbulent flow regimes, the friction factor is dependent on the Reynolds number and the channel surface roughness, which is given by the Moody chart [37].

For non-laminar, one-phase flow in a smooth channel, the friction factor can be evaluated by using the following two empirical relations [31]:

$$f = 0.316 Re^{-0.25} \ \left(2 \cdot 10^3 < Re < 2 \cdot 10^4\right) \tag{2.5}$$

$$f = 0.184 Re^{-0.20} \ \left(2 \cdot 10^4 < Re < 1 \cdot 10^6\right) \tag{2.6}$$

2.1.3 Nusselt number

The Nusselt number is the ratio of convective to conductive heat flow across (normal to) the boundary and is defined as:

$$Nu = \frac{hD_h}{\lambda} \tag{2.7}$$

where h is the convective heat transfer coefficient and λ is the thermal conductivity of the fluid.

For fully developed laminar, one-phase flow in a channel, the Nusselt number is determined by the cross sectional shape of the channel and the thermal boundary conditions [38].

For fully developed turbulent, one-phase flow in a smooth surface macrochannel ($Re > 10^4$), the Dittus-Boelter equation [39] may be used as a first approximation:

$$Nu = 0.023 Re^{0.8} Pr^n \tag{2.8}$$

where n=0.4 for heating and n=0.3 for cooling.

The Prandtl Number (Pr) is the ratio of the momentum diffusivity (kinematic viscosity, ν) and thermal diffusivity (α) and can be expressed as:

$$Pr = \frac{\nu}{\alpha} = \frac{\mu c_p}{\lambda} \tag{2.9}$$

where μ, c_p and λ are the dynamic viscosity, the specific heat at constant pressure and the thermal conductivity of the fluid, respectively. The Prandtl number describes the thickness of the hydrodynamic boundary layer compared with the thermal boundary layer. When the Prandtl number is less than unity, it means that the thermal diffusion is faster than the momentum diffusion.

For transient flow and fully developed turbulent, one-phase flow in a rough surface channel, the Gnielinski correlation [40] is recommended:

$$Nu = \frac{(f/8)(Re - 1000)Pr}{1 + 12.7(f/8)^{1/2}\left(Pr^{2/3} - 1\right)} \tag{2.10}$$

2.1.4 Deviations of microflow from classical macroscale theory

There are no concrete conclusions regarding the validity of classical macroscale theory for the prediction of fluid dynamics and heat transfer in microchannels. Wu and Little [32] measured friction factors for the flow of gases in microchannels with hydraulic diameter ranging from 45 to 83 μm. It was found that the measured friction factors had similar Reynolds number dependence as expected from the Moody Chart but the measured values were higher than the expected. Combining Eqs. 2.1, 2.3 and 2.4, Eq. 2.11 shows that, at fixed mass-flow rate, the pressure drop is inversely proportional to the fourth power of the hydraulic diameter of the channel. Therefore, a very precise value of the hydraulic

diameter of the channel is necessary for determining the friction factor. The change in the dimensions of the microchannel during the bonding was not considered in Wu and Little's measurement [32], which could be one reason of the deviations.

$$\Delta p = 0.5 f \rho v^2 \frac{l}{D_h} = 0.5 \frac{C\mu}{\rho D_h v} \rho v^2 \frac{l}{D_h} = 0.5 \frac{C\mu}{D_h} \left(\frac{\dot{m}}{\rho \pi D_h^2 / 4} \right) \frac{l}{D_h} \Rightarrow \Delta p \propto \frac{1}{D_h^4} \quad (2.11)$$

Similarly, the accuracy of the Nusselt number is strongly influenced by the accuracy of the measurement of the temperatures including the wall temperature of the microchannel and the fluid temperature in the microchannel, which is difficult to measure [41].

Another main cause of deviations is the relative surface roughness [42]. The roughness increases the momentum transfer in the boundary layer near the surface. Mala and Li [34] explained the surface roughness effects by using a so-called roughness-viscosity model, in which the additional momentum transfer was taken into account by introducing a roughness viscosity near the surface.

Even though some of the deviations could be explained by the causes mentioned above, there are also new phenomena which become increasingly important due to the small scale in microchannels such as viscous dissipation and electric double layers. For a given Reynolds number, the fluid velocities in microchannels are higher than in macrochannels. Therefore, frictional heating due to viscous dissipation has more influence for microchannels than it has for macrochannels. Koo and Kleinstreuer [43] investigated the viscous dissipation effect in microchannels. They found viscous dissipation became significant for water flow in microchannel with a hydraulic diameter less than 50 μm. Besides, the viscous dissipation effect increased as the aspect ratio of the microchannel deviated from unity. Microchannels made from material like silica, glass, acrylic, and polyester carry electrostatic charges. If the liquid contains a very small number of impurities with charge, the electrostatic charges on the microchannel surface will attract the counter ions in the liquid. The rearrangement of the charges on the surface and the balancing charges in the liquid is called an electric double layer. Yang et al. [44] found the effects of the electric double layer could have significant effects on the friction factor and the Nusselt number in microchannels with hydraulic diameters smaller than 40 μm.

The flow channels of the microcoolers described here are wet chemically etched. Therefore the surface roughness is considerably smaller than the channel depth and will have no significant influence on the friction factor and the Nusselt number. The hydraulic diameter of the flow channel in the CFHX of the microcooler is about 80 μm. Besides, the effects of viscous dissipation and electric double layer on gas flow in microchannels are much smaller than that of liquid flow in microchannels. We expect that the classical macroscale theory is applicable to the flow channels of the microcoolers. The fluid dynamics and heat transfer in the microchannel with pillar matrix are different from those in the microchannel without pillar matrix due to the vortices around the pillars. The influence of the pillar structure in the microchannel is addressed in chapter 8.

2.1.5 Conductive heat flow

Conduction is the heat transfer by means of molecular agitation within a substance without any motion of the substance as a whole. In a JT microcooler, conduction occurs through the CFHX's body along a direction parallel to the flow direction. Besides, conduction takes place vertically across the wafer through the pillars in the fluid channels. The rate of conduction in a specified direction is expressed by Fourier's law as:

$$\dot{Q} = -\lambda A \frac{dT}{dx} \tag{2.12}$$

where λ, A, and $\frac{dT}{dx}$ are the thermal conductivity of the material, the cross-sectional area and the temperature gradient, respectively.

The conduction along the direction parallel to the flow direction is unfavorable to JT microcoolers, which can be reduced by decreasing the thermal conductivity of the material. The main reason to select borosilicate glass (D263T) as the material of the microcoolers described in this thesis is its low thermal conductivity. However, the conduction along the direction perpendicular to the flow direction is favorable to the heat exchange between the warm high-pressure fluid and the cold low-pressure fluid in the microcoolers. The conduction can be improved by increasing the temperature gradient through decreasing the thickness of the middle wafer between the fluid channels.

2.1.6 Convective heat flow

Convection represents the heat transfer due to the movement of fluids. In a JT microcooler, convection occurs between the fluid and the surface of the channel and the pillars inside the channel. The rate of convection between the fluid and the surface can be expressed as:

$$\dot{Q} = hA\Delta T \tag{2.13}$$

where h, A and ΔT are the convective heat transfer coefficient, the heat exchange area and the temperature difference between the surface and the fluid, respectively. The convective heat transfer coefficient (h) is determined by the Nusselt number in the channel according to the Eq. 2.7.

2.1.7 Radiative heat flow

The heat transfer through radiation takes place through electromagnetic waves mainly in the infrared region. Two entities at different temperatures can exchange heat through radiation.

For two-surface enclosure as depicted in Figure 2.1, the radiative heat transfer rate ($\dot{Q}_{1-2}$) is represented by:

$$\dot{Q}_{1-2} = \frac{\sigma_B \left(T_1^4 - T_2^4\right)}{\frac{1}{\varepsilon_1 A_1} + \frac{1-\varepsilon_2}{\varepsilon_2 A_2}} \tag{2.14}$$

where σ_B is Stefan-Boltzmann constant, A_1 and A_2 inner and outer surface, ε_1 and ε_2 inner and outer emissivity.

In the measurement setup of a JT microcooler, the emissivity of the surroundings (the vacuum chamber) will be very high and close to 1. Besides, the surface of the vacuum chamber will be much larger than the surface of the microcooler ($A_1 << A_2$). Knowing this, Eq. 2.14 can be simplified to:

$$\dot{Q}_{1-2} = \varepsilon_1 \sigma_B A_1 \left(T_1^4 - T_2^4\right) \tag{2.15}$$

The material of the microcooler is borosilicate glass (D263T) that has a high emissivity value (0.8-0.95). To reduce the radiation loss, the microcooler's surface is covered with a thin gold layer. The emissivity of a smooth gold surface is about 0.02. In contrast, the emissivity of the sidewall of the microcooler and the temperature sensor and heaters on the microcooler surface is relatively high. For decreasing the radiation loss induced by these parts, a third surface can be inserted in the space between the microcooler and the vacuum chamber.

If there is a third surface inserted in the space between the two surfaces shown in Figure 2.2, the intermediate surface A_s shields A_2 from the radiosity emanating from A_1; at the same time, A_s shields from A_1 the fraction of A_2 radiosity that would be intercepted by A_1. The radiative heat transfer rate from A_1 to A_2 in this case is described by:

$$\dot{Q}_{1-2} = \frac{\sigma_B \left(T_1^4 - T_2^4\right)}{\frac{1}{\varepsilon_1 A_1} + \frac{1-\varepsilon_{s,1}}{\varepsilon_{s,1} A_s} + \frac{1}{\varepsilon_{s,2} A_s} + \frac{1-\varepsilon_2}{\varepsilon_2 A_2}} \tag{2.16}$$

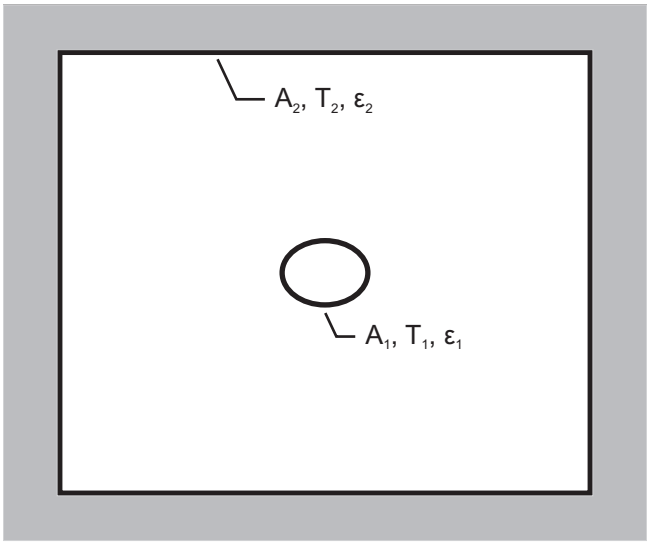

Figure 2.1: Enclosure with two surfaces.

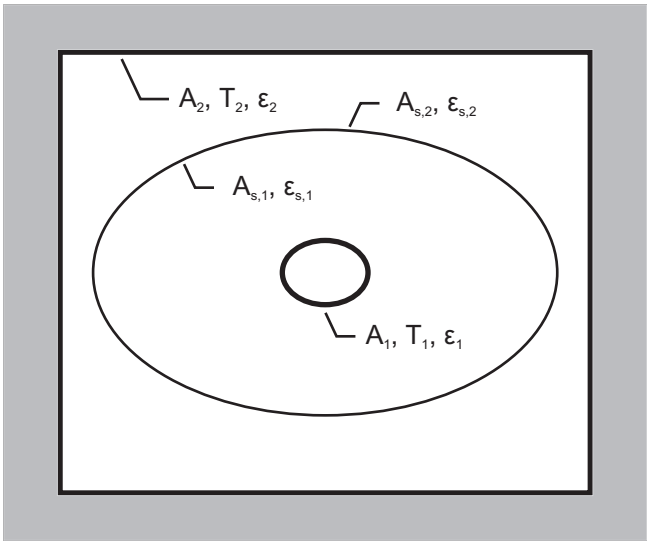

Figure 2.2: Enclosure with three surfaces.

If there is more than one surface inserted in the space between the two surfaces, the radiative heat transfer rate from A_1 to A_2 could be represented similarly. For multilayer insulation, the heat flux between A_1 and A_2 also include the conductive heat path due to the contact area between the layers besides the radiative heat path. When the number of layers increases, the radiative heat transfer will be reduced; however, the heat conduction through the layers will increase because the contact area increases. Consequently, there is an optimal number of layers in the design of the thermal insulation.

Taking into account that the emissivity of the surrounding is close to 1 and the surface of the vacuum chamber is much larger than the surface of the cooler, Eq. 2.16 becomes:

$$\dot{Q}_{1-2} = \varepsilon_{ave}\sigma_B A_1 \left(T_1^4 - T_2^4\right) \tag{2.17}$$

$$\varepsilon_{ave} = \frac{1}{\frac{1}{\varepsilon_1} + \frac{A_1}{\varepsilon_{s,1}A_s} + \frac{A_1}{\varepsilon_{s,2}A_s} - \frac{A_1}{A_s}} \tag{2.18}$$

From Eq. 2.18, we know that ε_{ave} reaches minimum value when A_s equals A_1.

The intermediate material could be any superinsulation film with low emissivity. Beside, crinkled superinsulation film is often used because it provides built-in stand-offs to minimize heat transfer by conduction in multilayer applications.

2.1.8 Molecular flow conduction

To minimize the heat transfer between a microcooler and the surrounding gas, the microcooler is operated in a vacuum chamber where a vacuum pressure of less than 0.01

Pa is maintained. In this case, the gas around the microcooler lies in the free molecular flow regime. In this flow regime, the conduction through the gas is proportional to the gas pressure (p) and the temperature difference between the mcirocooler and the surrounding gas (ΔT) [45]:

$$\dot{Q} = \alpha \lambda_m p A \Delta T \tag{2.19}$$

where

$$\alpha = \frac{\alpha_1 \alpha_2}{(\alpha_1 + \alpha_2 - \alpha_1 \alpha_2)} \tag{2.20}$$

$$\lambda_m = \frac{\gamma + 1}{\gamma - 1} \sqrt{\frac{R}{8\pi M T}} \tag{2.21}$$

Here, α is the average thermal accommodation coefficient, λ_m is the molecular flow heat conduction coefficient, γ is the ratio of the isobaric and isochoric specific heats of the gas, M is the molecular mass of the gas, R is the ideal gas constant, T is the gas temperature, α_1, α_2 are the coefficients of thermal accommodations, respectively.

2.2 Design of a two-stage microcooler

2.2.1 Introduction

To reach a temperature of about 30 K using the JT effect, hydrogen or neon gas can be used as the working fluid. However, in order to generate cooling by JT expansion, these gases should be precooled below their inversion temperatures, i.e. 205 and 250 K, for hydrogen and neon gas, respectively. Thus a two-stage JT cooler is required, in which the first stage precools the second stage. A schematic of the Linde-Hampson cycles of a two-stage JT cooler is shown in Figure 2.3. In the first stage, the fluid with inversion temperature above ambient temperature is pressurized isothermally using a compressor ($5 \rightarrow 1$). After compression, the high-pressure fluid flows through the CFHX I exchanging heat with the low-pressure return fluid ($1 \rightarrow 2$). The high-pressure fluid then expands over the restriction I, cools down and changes partially its phase to a liquid ($2 \rightarrow 3$). By absorbing heat from the pre-cooler, the liquid evaporates ($3 \rightarrow 4$), and the vapor flows back to the compressor via the CFHX I ($4 \rightarrow 5$). In the second stage, after compression ($13 \rightarrow 6$), the high-pressure fluid flows through the CFHX II ($6 \rightarrow 7$). Then, the high-pressure fluid is precooled to below its inversion temperature by the evaporator of the first stage ($7 \rightarrow 8$). It flows to the restriction II via the CFHX III ($8 \rightarrow 9$) and undergoes an isenthalpic expansion, cools down and changes partially its phase to a liquid ($9 \rightarrow 10$). By absorbing heat from its surroundings the liquid evaporates ($10 \rightarrow 11$) and the vapor flows back through the CFHX III and CFHX II ($11 \rightarrow 13$).

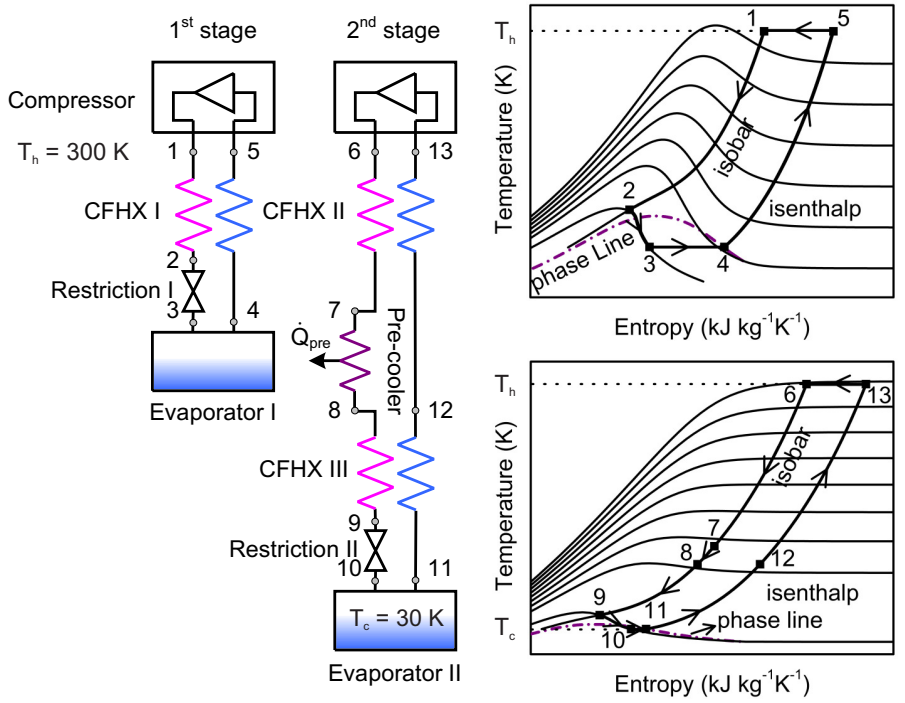

Figure 2.3: Schematic of the Linde-Hampson cycle of a two-stage cooler and the thermodynamic cycles drawn in temperature-entropy diagrams.

2.2.2 Optimization of working fluids

To select the optimum working fluids, the COP of the two-stage cooler at the steady state is investigated, based on the assumptions that the CFHXs and the pre-cooler are ideal heat exchangers and all net cooling power of the first stage is used for precooling the second stage. The COP of the two-stage cooler (shown in Figure 2.3) is defined as the ratio of the gross cooling power at the second stage and the change in Gibbs free energy of the fluids of both stages during compression.

$$COP = \frac{-\Delta h_{11,10}\dot{m}_{II}}{(\Delta h_{5,1} - T_h \Delta s_{5,1})\,\dot{m}_I + (\Delta h_{13,6} - T_h \Delta s_{13,6})\,\dot{m}_{II}} \tag{2.22}$$

Here, $\dot{m}_I$ and $\dot{m}_{II}$ are the mass-flow rates in the respective cold stages; $\Delta h_{x,y}$ is the enthalpy difference between points x and y; analogously $\Delta s_{x,y}$ is the entropy difference between these two points.

The stationary energy balance of the first evaporator gives:

$$\dot{m}_I / \dot{m}_{II} = \Delta h_{7,8} / \Delta h_{4,3} \tag{2.23}$$

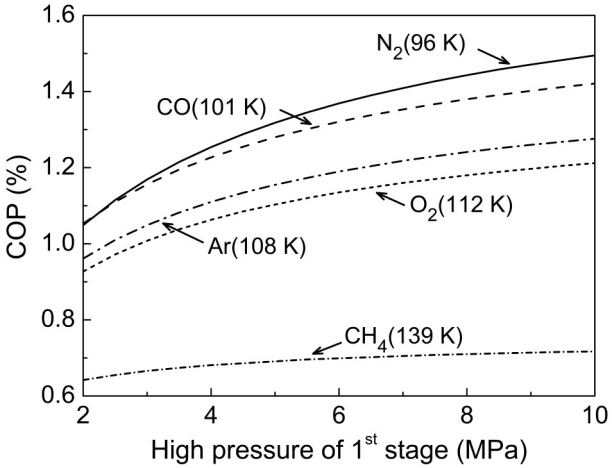

Figure 2.4: Ideal-case COP as a function of the 1st stage high pressure for various working fluids. Low pressure of the 1st stage is 0.60 MPa and high pressure of the 2nd stage is 4.0 MPa hydrogen gas. The saturation temperatures of the corresponding working fluids at 0.60 MPa are shown in parenthesis.

To achieve a temperature that is below the inversion temperature of neon or hydrogen, candidate first-stage fluids are nitrogen, argon, carbon monoxide, oxygen and methane. The working fluids of both stages are optimized based on a target temperature of 28 K with an allowance of 2 K. The corresponding equilibrium vapor pressures of neon and hydrogen at 28 K are 0.13 and 0.57 MPa, respectively.

Figure 2.4 shows the influence of the first-stage working fluid at different values of the high pressure with hydrogen as the second-stage working fluid. The low pressure of the first stage is fixed at 0.60 MPa and the high pressure of the second stage at 4.0 MPa. The saturation temperatures of the candidate first-stage fluids at 0.60 MPa are shown in Figure 2.4. The COP increases with increasing high pressure of the first stage. This is because the specific enthalpy difference of the fluid between high and low-pressure side of the first stage increases. Nitrogen gas as the first-stage working fluid yields the best COP, mainly because the saturation temperature of nitrogen at 0.60 MPa is the lowest among the candidate first-stage fluids. The influence of the first-stage low pressure and relevant pre-cooler temperature ranges of the candidate first-stage fluids from 0.10 to 1.00 MPa are shown in the Figure 2.5 with the high pressure of the first stage and the high pressure of the second stage being fixed at 8.0 and 4.0 MPa, respectively. The COP decreases with increasing low pressure of the first stage. This is because the pre-cooler temperature increases and thus the specific enthalpy difference of the fluid between high and low-pressure side of the second stage after precooling decreases. The difference in COP of the candidate first-stage fluids is small when the pre-cooler temperature is the same as shown

in Figure 2.5b.

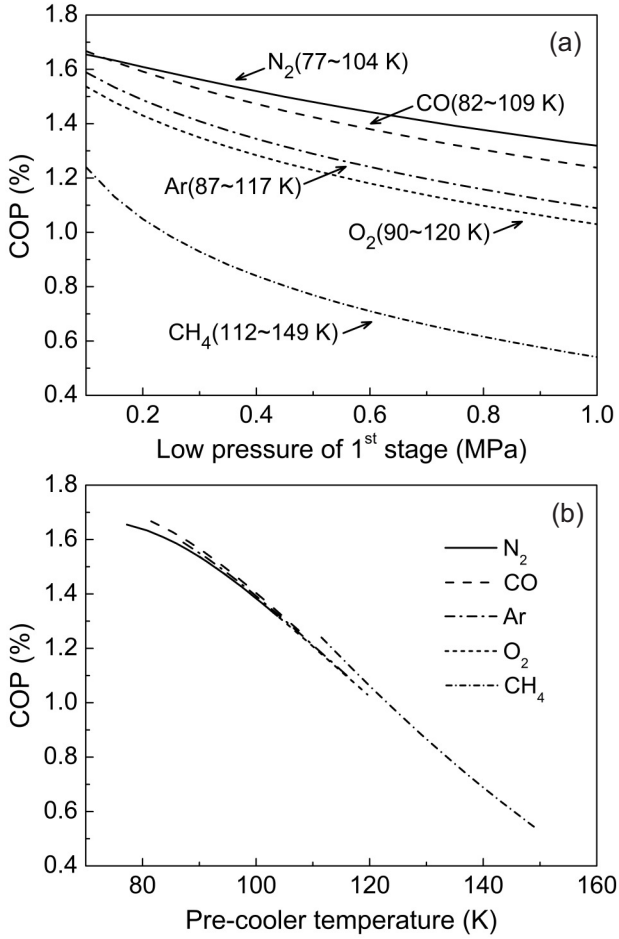

Figure 2.5: Ideal-case COP as a function of the 1st stage low pressure (a) and the corresponding pre-cooler temperature (b) for various working fluids. High pressure of the 1st stage is 8.0 MPa and high pressure of the 2nd stage is 4.0 MPa hydrogen gas. The temperature ranges shown in parenthesis of (a) are the saturation temperature ranges of the corresponding working fluids from 0.10 to 1.00 MPa, which are also the relevant pre-cooler temperature ranges shown in (b).

The influence of the second-stage high pressure is shown in Figure 2.6 under the condition that the first stage is operated with nitrogen gas, expanding from 8.0 to 0.60 MPa. The COP increases with increasing high pressure of the second stage. Hydrogen gas as the second-stage working fluid has a better performance than neon gas when the high pressure is below 9.2 MPa. Since, in future, we intend to operate the two-stage cooler with a sorption compressor, a modest high pressure is attractive and,

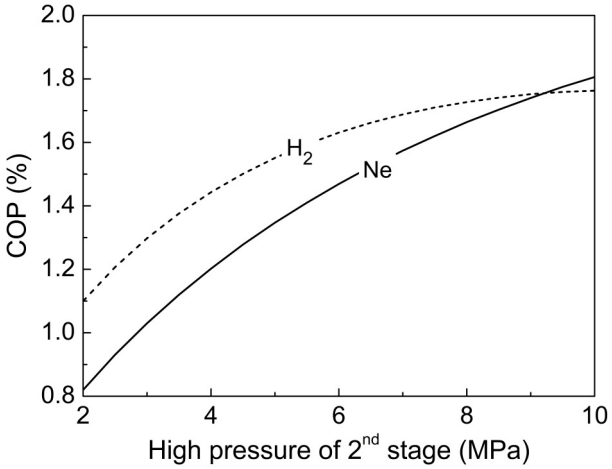

Figure 2.6: Ideal-case COP as a function of the 2nd stage high pressure for hydrogen and neon gas. The 1st stage is operated with nitrogen gas between 8.0 and 0.60 MPa.

therefore, hydrogen gas is chosen as the second-stage working fluid.

The nominal operating high and low pressures of the first stage are selected as 8.0 and 0.60 MPa to be consistent with earlier studies [22], and those of the second stage as 4.0 and 0.57 MPa as shown in Table 2.2.

Table 2.2: Operating pressures selected for optimum fluids of the two-stage cooler.

Stage	Working fluid	High pressure (MPa)	Low pressure (MPa)
First	N_2	8.0	0.60
Second	H_2	4.0	0.57

2.2.3 Optimization of cooler dimensions

The geometry of the two-stage microcooler as shown in Figure 2.7 is based on the single-stage microcooler design that was realized by Lerou et al. [21]. The cooler consists of a stack of three glass wafers. A thin gold layer is deposited on the cooler's surface to reduce the radiation losses. For each stage, the high and low-pressure lines are isotropically etched in the middle and bottom wafers. The channels contain pillars to limit the maximum mechanical stress due to the high pressure. In each stage, the high-pressure line ends in a flow restriction, which is extended to the evaporator volume and connected to the low-pressure line. Thus, a CFHX is formed by the high and low-pressure channels and the thin intermediate glass wafer. In order to increase the heat transfer between pre-cooler

and the first evaporator, they are integrated into a compact design with a relatively large heat-transfer area. Here, the low-pressure fluid of the first stage, after expansion, needs to take up heat from the high-pressure fluid of the second stage. The thermal resistance between the pre-cooler and the first evaporator includes the convective resistance from low-pressure fluid of the first stage to middle wall, the conductive resistance through that wall and the convective resistance from middle wall to the high-pressure fluid of the second stage.

Based on the earlier work, borosilicate glass D263T is chosen as the fabrication material [21]. Considering pressure requirements, the mechanical properties of borosilicate glass D263T, and manufacturability, the thicknesses of the top wafer, middle wafer and bottom wafer are chosen as 400, 145 and 175 μm respectively.

In terms of dimensions, the CFHX length should be large to maximize the heat exchange between high-pressure fluid and low-pressure fluid and to reduce the longitudinal conductive losses. The disadvantage of a longer CFHX is a larger pressure drop and a higher heat flux from the 300 K environment through radiation and conduction via residual gas in the vacuum space. The channel height should be small to maximize the heat exchange between the high-pressure and low-pressure flows. However, a smaller channel height results in a higher pressure drop. Considering the influence of the pillars in the channels on the pressure drop and fabrication constraints, the height of the channels is fixed at 40 μm. In addition, to simplify the structure of the two-stage microcooler, several parts of the microcooler have equal dimensions. For instance, the CFHX I and CFHX II have the same length; the CFHX II and CFHX III have the same width.

In order to optimize the microcooler dimensions, a dynamic finite-element model of the cooler has been developed in which the parasitic heat losses and the mass-flow

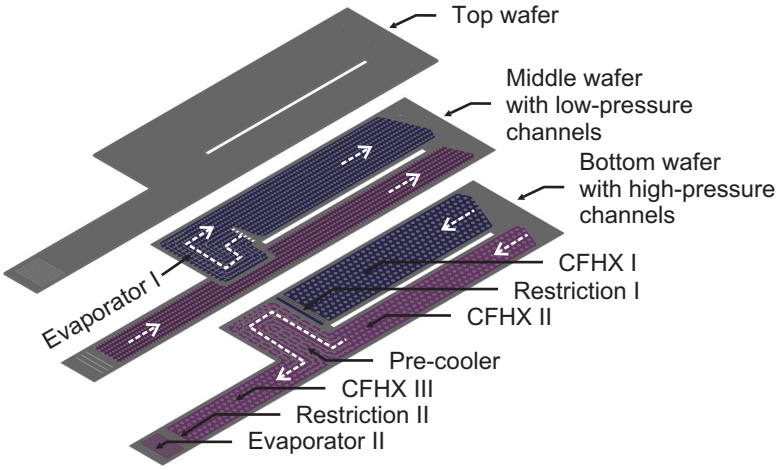

Figure 2.7: Exploded view of the two-stage microcooler.

rates change with the cold-end temperatures during the cool-down process. The model is based on the simplified dynamic lumped-element model of a two-stage microcooler presented elsewhere [46]. In the model, the two-stage microcooler is divided into six parts (three CFHXs, two evaporators and a pre-cooler) as shown in Figure 2.8. The CFHX is split into elements of constant length and each element contains three sub-elements: a high-pressure fluid element, a material element and a low-pressure fluid element. The temperature nodes for the fluid streams are placed at the border of the fluid elements and temperature nodes for material are placed in the centre of the material elements. The constant wall temperature boundary condition for laminar flow is used to determine the Nusselt number (Nu) within each element. Besides the boundary condition, the Nusselt number also depends on the cross-sectional shape of the channel for fully developed laminar flow [38]. The nodes of the fluid elements are connected by enthalpy flow ($\dot{H}$), whereas the nodes in the material elements are connected by longitudinal conductive heat flow ($\dot{Q}_c$). The nodes of fluid elements and material elements are connected by the convective heat flow ($\dot{Q}_{wg}$ and $\dot{Q}_{gw}$). The pre-cooler and the two evaporators are treated as single elements. These separate elements are connected to the different CFHXs by enthalpy flow and longitudinal conductive heat flow. Moreover, the radiative heat flow ($\dot{Q}_{rad}$) on the microcooler outer surface and conductive heat flow via the surrounding gas ($\dot{Q}_{csg}$) are taken into account. To minimize the radiative heat load on the microcooler, the outer surface of the microcooler is coated with a thin layer of gold. The emissivity of a smooth gold surface (ε) is around 0.02 [31]. In our design, a conservative emissivity value of 0.04 is used to allow for design margin. The conductive heat flow via the surrounding gas is determined by the average thermal accommodation coefficient (α), the molecular flow heat conduction coefficient (λ_m around 1.23 for air) and the ambient pressure as shown in Table 2.3. The thermal accommodation coefficient is a value between 0 and 1. If molecules thermally equilibrate with the wall by making many collisions on a rough surface, the value nears to 1. If the surface is smooth and molecules rebound without energy transfer, the value approaches 0. The conductive heat flow transfer from the surrounding gas is lower than the radiative heat flow when the ambient pressure is less than 0.01 Pa. The microcooler is intended to operate in a vacuum pressure of about 0.005 Pa, so the contribution of heat loss due to the surrounding residual gas is negligible. At the warm ends of CFHXs I and II, the nodes are assumed to be at an ambient temperature of 300 K, whereas the warm end of CFHX III is assumed to be at the pre-cooler temperature. The cold ends of CFHXs I and III are assumed to be at the temperatures of the fluids in the evaporators because CFHXs I and III terminate in the evaporators. The temperature of the cold end of CFHX II at the low-pressure side is assumed to be the outlet temperature of the low-pressure fluid of CFHX III.

The energy balances for the pre-cooler and the two evaporator elements are given by:

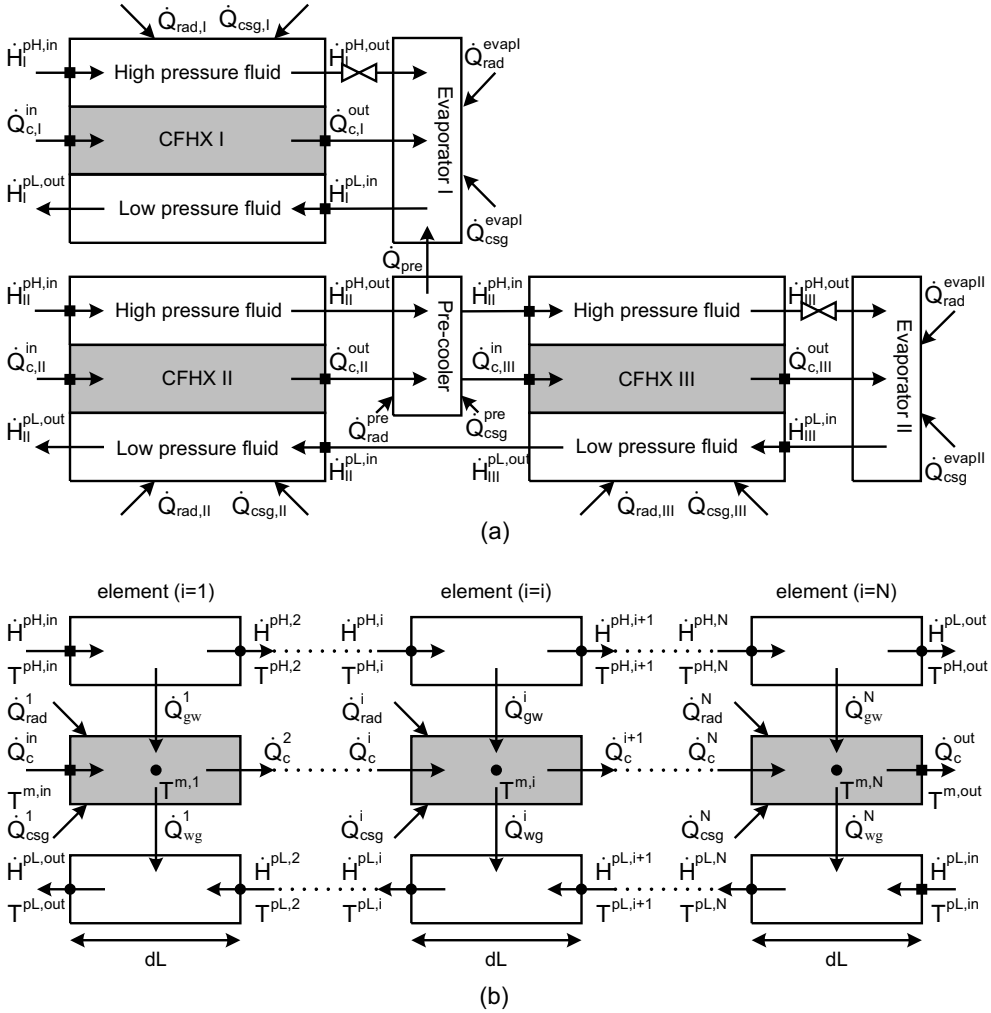

Figure 2.8: Block diagram of the two-stage microcooler dynamic model (a) and CFHX model (b). Temperature nodes indicated by rectangular symbol serve as boundary conditions of CFHXs.

Evaporator I:

$$\dot{H}_I^{pH,out} + \dot{Q}_{c,I}^{out} - \dot{H}_I^{pL,in} + \dot{Q}_{pre} + \dot{Q}_{rad}^{evapI} + \dot{Q}_{csg}^{evapI} = C^{evapI} dT^{evapI}/dt \tag{2.24}$$

Pre-cooler:

$$\dot{H}_{II}^{pH,out} + \dot{Q}_{c,II}^{out} - \dot{Q}_{pre} - \dot{H}_{III}^{pH,in} - \dot{Q}_{c,III}^{in} + \dot{Q}_{rad}^{pre} + \dot{Q}_{csg}^{pre} = C^{pre} dT^{pre}/dt \tag{2.25}$$

Evaporator II:

$$\dot{H}_{III}^{pH,out} + \dot{Q}_{c,III}^{out} - \dot{H}_{III}^{pL,in} + \dot{Q}_{rad}^{evapII} + \dot{Q}_{csg}^{evapII} = C^{evapII} dT^{evapII}/dt \tag{2.26}$$

For the CFHX elements, the following energy balances can be derived:

High-pressure fluid:

$$\dot{H}^{pH,i} - \dot{H}^{pH,i+1} - \dot{Q}_{gw}^{i} = C^{pH,i} dT^{pH,i+1}/dt \tag{2.27}$$

Material:

$$\dot{Q}_{c}^{i} + \dot{Q}_{rad}^{i} + \dot{Q}_{csg}^{i} + \dot{Q}_{gw}^{i} - \dot{Q}_{wg}^{i} - \dot{Q}_{c}^{i+1} = C^{m,i} dT^{m,i}/dt \tag{2.28}$$

Low-pressure fluid:

$$\dot{H}^{pL,i+1} + \dot{Q}_{wg}^{i} - \dot{H}^{pL,i} = C^{pL,i} dT^{pL,i}/dt \tag{2.29}$$

The relation between different energy flows and temperature nodes are shown in Table 2.3.

The model is built in the software program Simulink [47] using block diagrams expressing the equations. Each element is created as a sub-system that is connected through input and output ports.

The mass-flow rate of each stage is determined by temperature-dependent working-fluid properties (i.e. density and viscosity) and the dimensions of the JT restriction. The flow through the restriction is assumed to be laminar due to the small dimensions of the restriction and the relatively low mass-flow rate. Furthermore, we assume the restriction to be isothermal at a temperature equal to that of the evaporator because the evaporator is in direct thermal contact with the restriction. In that case, the mass-flow rates ($\dot{m}$) of both

Table 2.3: Relation between different energy flows and temperature nodes.

Energy flows	**Expressions**
Precooling power	$\dot{Q}_{pre} = \left(T^{pre} - T^{evapI}\right)/R$
Enthalpy flow rate	$\dot{H} = \dot{m}h\left(p,T\right)$
Convective heat transfer rate	$\dot{Q}_{gw}^{i} = U_{gw}^{i} A_{\|\|} \left(\left(T^{pH,i} + T^{pH,i+1}\right)/2 - T^{m,i}\right)$
between fluid and material	$\dot{Q}_{wg}^{i} = U_{wg}^{i} A_{\|\|} \left(T^{m,i} - \left(T^{pL,i} + T^{pL,i+1}\right)/2\right)$
Conduction heat transfer rate	$\dot{Q}_{c}^{i} = \lambda^{i} A_{\perp} \left(T^{m,i-1} - T^{m,i}\right)/dL$
along material	$\dot{Q}_{c}^{in} = 2\lambda^{in} A_{\perp} \left(T^{m,in} - T^{m,1}\right)/dL$
	$\dot{Q}_{c}^{out} = 2\lambda^{out} A_{\perp} \left(T^{m,N} - T^{m,out}\right)/dL$
Radiative heat flow	$\dot{Q}_{rad}^{i} = \varepsilon\sigma_{B} A^{i} \left(\left(T^{a}\right)^{4} - \left(T^{m,i}\right)^{4}\right)$
Heat flux via the surrounding gas	$\dot{Q}_{csg}^{i} = \alpha\lambda_{m} p A^{i} \left(T^{a} - T^{m,i}\right)$

stages can be determined by the following equation [31]:

$$\dot{m}(p, T_{evap}) = \frac{wh^3}{12l} \int_{pL}^{pH} \frac{\rho(p, T_{evap})}{\mu(p, T_{evap})} dp \tag{2.30}$$

where w, h and l are the width, height and length of the restriction, respectively, and pH and pL are the high and low pressures, respectively. ρ is the density and μ the viscosity which both are pressure (p) and evaporator temperature (T_{evap}) dependent.

To search for the cooler with the smallest cooler dimensions that satisfies the cooling requirements, the Matlab Optimization Toolbox [47] is employed. The parameter to be minimized is the cooler volume, and the variable parameters are the length and width of CFHXs I and III and the two restrictions. The height of the restrictions is fixed at 1.1 μm to be consistent with the production process of earlier studies. The constrained conditions are that the net cooling power of the first stage is at least 50 mW and that of the second stage at least 20 mW, the heat exchanger efficiency (the ratio of the heat absorbed by the low-pressure fluid to the heat demanded for the low-pressure fluid when its outlet temperature reaches the inlet temperature of the high-pressure fluid) of CFHX I and III is at least 0.995 and the maximum design area of the wafer used during manufacturing is fixed at 90.0 x 90.0 mm^2.

The optimized CFHX dimensions are shown in Table 2.4. The height of the gas channels in the CFHX is 40 μm. The restriction of the first and second stages consist of 21 and 10 parallel rectangular slits, respectively. The length and the total width of the restrictions are also shown in Table 2.4. The height of the slits in the restriction of both the stages is 1.1 μm. The overall dimensions of the cooler are 85.8 x 20.4 x 0.72 mm^3. Here, 5 mm extra length for the inlet and outlet gas connections is included as well as a 1 mm gap separating the two stages.

Table 2.4: Dimensions of the two-stage micro-cooler (components indicated in Figure 2.7).

Component	Length (mm)	Width (mm)
CFHX I	35.9	11.9
CFHX II	35.9	7.5
CFHX III	25.5	7.5
Restriction I	1.00	2.14
Restriction II	1.75	0.62

2.2.4 Cooler performance with nitrogen and hydrogen as working fluids with optimum dimensions

At steady state, the gross cooling power of the first stage (the product of the mass flow rate of the first stage and the enthalpy difference of the warm end of CFHX I under the actual

conditions) is 192 mW of which 109 mW is used for precooling the second stage, 19 and 14 mW are lost in conduction and radiation, respectively. As required, the resulting net cooling power of the first stage is 50 mW. The gross cooling power of the second stage (the product of the mass flow rate of the second stage and the enthalpy difference of the warm end of CFHX III under the actual conditions) is 35 mW of which 4 and 11 mW are lost in conduction and radiation, respectively, resulting in a net cooling power of 20 mW at the second stage.

The temperature profiles of the three CFHXs at steady state are shown in Figure 2.9. In CFHX I and III, the temperature gradients increase towards the cold ends as well as the temperature differences between high-pressure fluid and low-pressure fluid. This is due to the difference in specific heat capacities of the high and low-pressure fluid streams. At relatively high temperature this difference is quite small and hence the temperature difference is also much smaller. The dynamic behavior of the microcooler with optimum geometry is analyzed in detail using the finite-element model described above. The cool-down curves of the evaporators of both stages are shown in Figure 2.10a. The first stage cools to 97 K in 0.3 hour. The second-stage evaporator temperature decreases rapidly after $t \approx 1.5$ hour, and then achieves 28 K at 1.7 hour. The cool-down times of both stages depend on the corresponding net cooling powers. The small increase in pre-cooler temperature at around 1.7 hour is mainly because of the increase in mass-flow rate of the hydrogen, which is due to a decrease in temperature of evaporator II.

The gross and net cooling powers of both stages and the precooling power as a function of time are shown in Figure 2.10b. It is important to note that the power recordings match the temperature evolution as depicted in Figure 2.10a. The net cooling power of the first stage decreases at the start although the gross cooling power increases at the same time. This is because the parasitic heat loads and precooling power increase more than the gross cooling power. The net cooling power increases rapidly after evaporator I has achieved its steady temperature. At about 1.6 hour it decreases steeply, and then it increases a little and remains constant at 50 mW. This is mainly because the power taken by the pre-cooler varies in time. At the start, for about 0.5 hour, the net cooling power of the second stage is larger than its gross cooling power. This is because the pre-cooler is significantly colder than the second evaporator (see Figure 2.10a), and thus heat flows through CFHX III from evaporator II to the pre-cooler. After 0.5 hour, the net cooling power gets smaller than the gross cooling power because the heat conduction from evaporator II to the pre-cooler decreases and parasitic heat loads increase. At steady state, the net cooling power of the second stage stabilizes at 20 mW. Thus, the net cooling power of the second stage, in the beginning, is dominated by the longitudinal conduction, whereas it is dominated by enthalpy flow after about 1.5 hour. This can also be derived from the temperatures of both evaporators and the pre-cooler versus time and the mass-flow rates as shown in Figure 2.10. The mass-flow rates change in time because viscosity and density of the working fluids change with temperature. The mass-flow rates of the first and the second stages eventually stabilize at 14.0 and 0.94 mg s^{-1}, respectively.

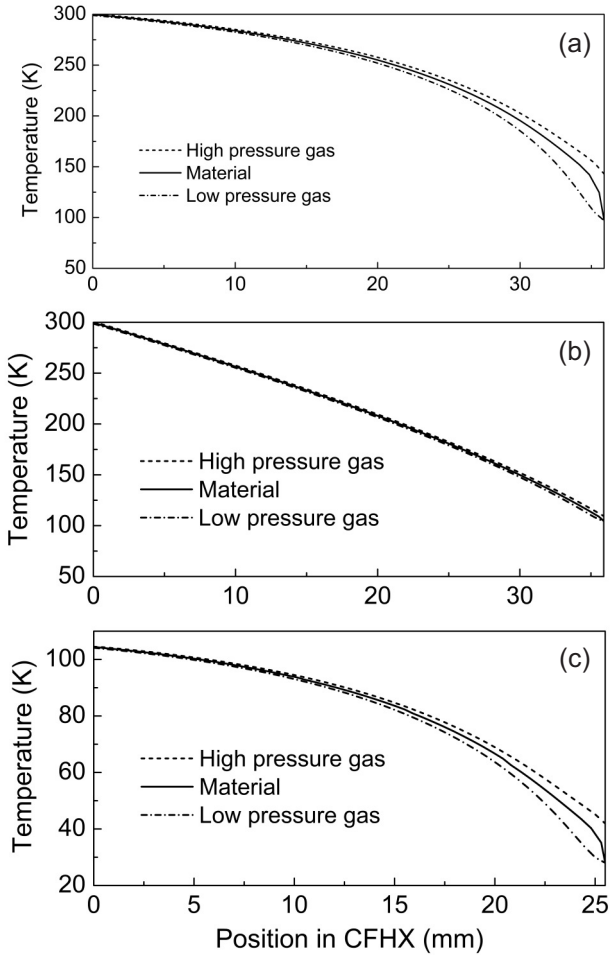

Figure 2.9: Steady-state temperature profiles of the three CFHXs. (a) CFHX I. (b) CFHX II. (c) CFHX III.

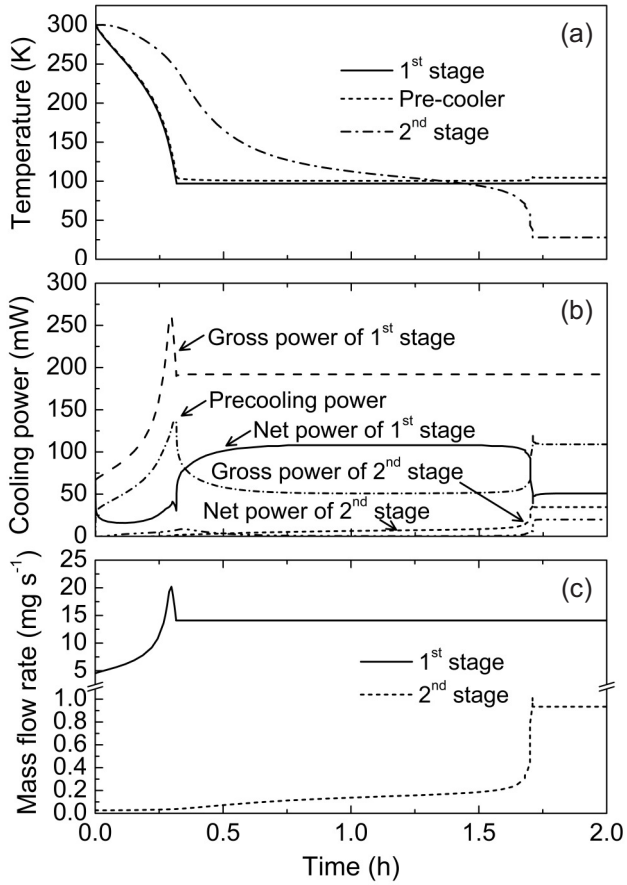

Figure 2.10: Dynamic behavior of the cooler. (a) Temperatures of both evaporators and pre-cooler. (b) Gross and net cooling powers of both stages and precooling power. (c) Mass-flow rates of both stages.

2.2.5 Parameter sensitivity analysis

Small deviations may occur compared to the designed geometry in the fabrication process. It is, therefore, important to know the influence of the different parameters on the performance of the microcooler.

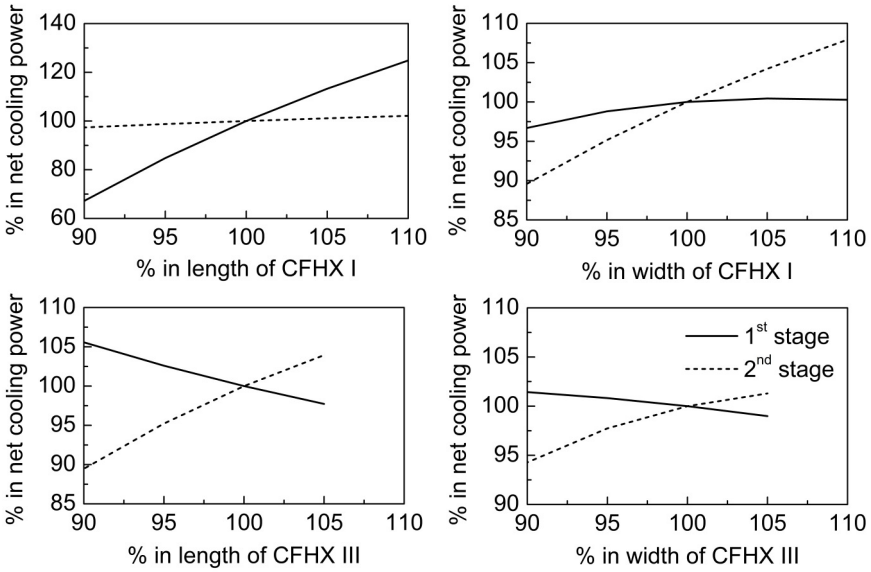

Figure 2.11: Influences of relative variations of the optimal parameters on the both stage net cooling powers.

The effects of variations in optimized parameters on the net cooling powers are shown in Figure 2.11. It should be noted that the length of CFHX II and width of CFHX II are coupled to the length of CFHX I and the width of CFHX III, respectively, and are changed in parallel. The net cooling power of the first stage increases with the increasing length of CFHX I because of the increasing heat exchanger efficiency. The influence of the length of CFHX I hardly affects the net cooling power of the second stage. The net cooling power of the first stage increases with increasing width of CFHX I at the start (larger contact area and therefore better heat-exchange efficiency), then the increase reduces gradually due to the increasing conduction loss. The heat transfer area between pre-cooler and the first evaporator increases with increasing width of CFHX I. That is why the increasing width of CFHX I is beneficial to the second stage net cooling power. Increasing the length of CFHX III improves the net cooling of the second stage but the net cooling power of the first stage decreases because of the higher precooling power is required. The influence of the width of CFHX III on the second stage net cooling power is similar to that of CFHX I on the first stage net cooling power. The conduction loss from CFHX II to CFHX III increases with increasing CFHX width, which results in a decrease in the first stage net

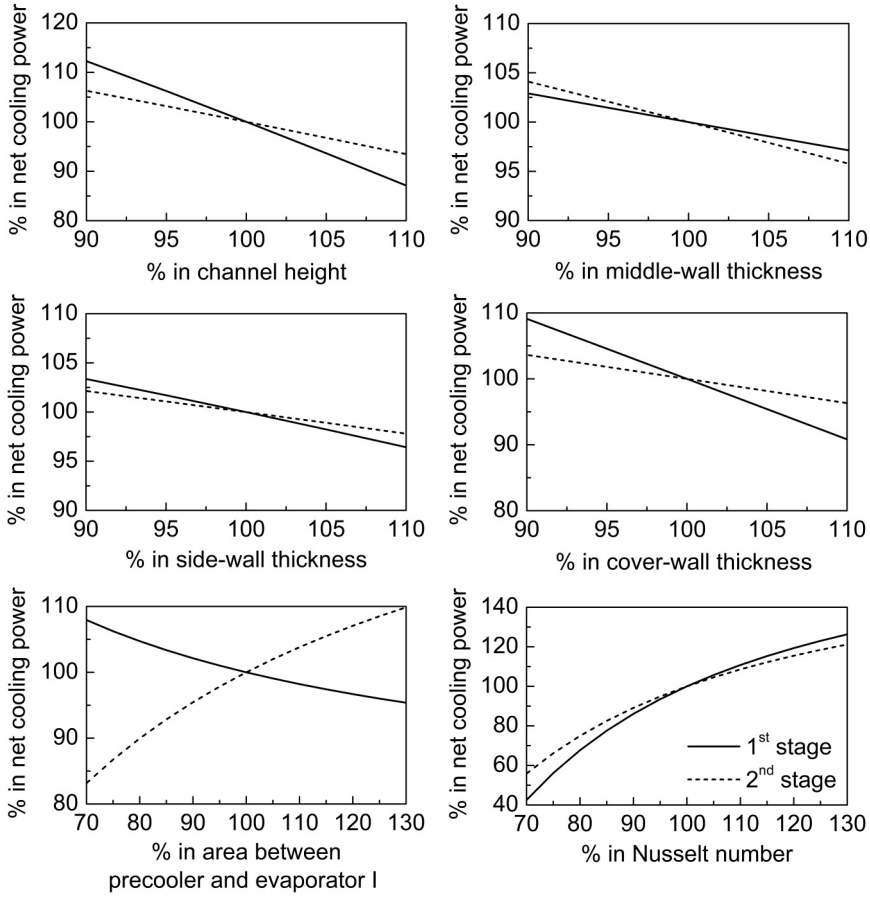

Figure 2.12: Influences of relative variations of the non-optimal parameters on the both stage net cooling powers.

cooling power. Besides, the increase of length or width is limited by conduction and radiation losses of CFHX III. Excessive increase ($> 5\%$) will obstruct the cooler from cooling down to 28 K.

The effects of variations in non-optimized parameters are shown in Figure 2.12. Increasing the channel height or the wall thicknesses are not beneficial to the cooler performance, which is opposite to the effect of the Nusselt number. A larger channel height results in a larger hydraulic diameter and thus in a lower heat transfer coefficient. The conduction loss increases due to the increasing wall thicknesses, and a larger middle-wall causes a higher thermal resistance between the fluids in the CFHX. The area between pre-cooler and the first evaporator determines the thermal resistance between them. Therefore, increasing that area results in an increase in the net cooling power of the second

stage but in a decrease in the net cooling power of the first stage.

2.3 Conclusions

Classical macroscale theory of fluid dynamics and heat transfer of one-phase flow has been reviewed. Possible explanations for deviations of microflow from classical theory have been discussed. It can be concluded that the classical theory is applicable to flow channel in the CFHX of the two-stage microcooler. The working fluids in the two-stage microcooler operating at 28 K are optimized on the basis of the COP, and nitrogen and hydrogen gas are chosen as the first stage and the second stage working fluid, respectively. A finite-element model with lumped evaporators and pre-cooler is developed for the two-stage microcooler. The minimum-volume cooler geometry with a cooling power of 50 mW at 97 K and 20 mW at 28 K is obtained with the model developed employing the Matlab Optimization Toolbox. The cooler with optimum overall dimensions of 85.8 x 20.4 x 0.72 mm^3 cools down to 28 K within 1.7 hour with mass-flow rates of 14.0 mg s^{-1} nitrogen gas and 0.94 mg s^{-1} hydrogen gas at steady state. After that, the sensitivities of the optimal and non-optimal parameters on the microcooler performance are analyzed.

CHAPTER 3

Fabrication and application demonstration

In this chapter, the fabrication of the two-stage microcooler is briefly introduced. The application potential of the microcooler coupled with electronic devices is demonstrated by cooling an YBCO film through its superconducting phase transition.

3.1 Fabrication

The two-stage microcooler is fabricated using standard micromachining technology (see Figure 3.1). Compared to the design cooler presented in chapter 2, there is no slit between CFHX I and CFHX II because creating this slit appeared to be a risky step in the production of the cooler. The slits in the restrictions are buffered hydrofluoric acid (HF) etched, and gas channels in the CFHX are HF etched. The evaporator slits and feedthroughs are powder blasted. Next, the three wafers are fusion bonded to one stack. Separate microcoolers are obtained by a combination of dicing and powder blasting through the stack with a suitable mask. After separation, A 0.2 μm layer of gold is deposited on the microcooler to increase the reflectivity of the surface thereby lowering the thermal radiation heat load on the microcooler. This approach allows the fabrication of many such microcoolers at low cost. The bonding and powder blasting process are the critical steps that currently mainly determine the production yield. The fabrication process is similar to our single-stage microcooler, the details of which were discussed in an early study [21]. Figure 3.1 shows the two-stage microcooler without a gold layer.

3.2 Application demonstration of cooling superconducting devices

3.2.1 Measurement set-up

The schematic of the experimental setup for characterizing the microcooler is shown in Figure 3.2. Nitrogen and hydrogen gas (both purity level 5.0) are supplied from pressurized gas bottles. The gas flows through pressure controllers (HPC) that regulate

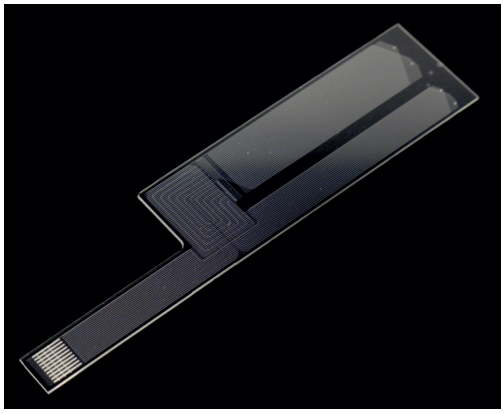

Figure 3.1: Photograph of the two-stage microcooler.

the high pressures. The nitrogen gas is purified with a getter filter. Impurities from the nitrogen gas (especially water) are removed to about 1.0 parts per billion (ppb) level to prevent clogging due to water deposition [48]. The clogging issue will be discussed in details in chapter 5. Impurities from the hydrogen gas are trapped in the pre-cooler and a getter filter is considered not necessary. The microcooler is mounted in a glass vacuum chamber where a vacuum pressure of less than 0.01 Pa is maintained. At the low-pressure side, the pressure of the gas is measured with a pressure meter (LPM), and the outflow is measured with a mass-flow meter (MFM). Pressure relief valves are used at the outlets of both stages to maintain constant outlet pressures and also to prevent air from flowing into the system. The dashed lines in Figure 3.2 indicate tubes that are used to pump and flush the system. The microcooler is mounted into a flange and surrounded by a printed circuit board (PCB) as shown in Figure 3.3. The temperature is measured at the evaporator of the nitrogen and hydrogen stages indicated by T1 (Pt 1000 sensor) and T2 (Dt 471 diode sensor), respectively. The temperature sensor locations are shown in Figure 3.3. A surface mounted device resistor used as a heater, which is glued on the pre-cooler, is used to apply heat and to control the temperature of the nitrogen stage. The temperature sensors, heater and YBCO film are glued on the microcooler with conducting silver paint and connected to the PCB using bond wire made of 99% aluminum and 1% silicon with a diameter of 25 μm. A silicon piece as shown in Figure 3.3 is glued to the evaporator of

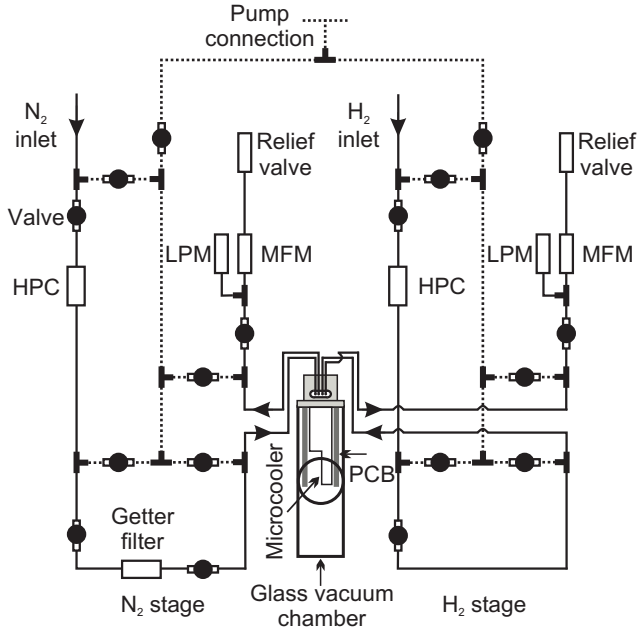

Figure 3.2: Schematic of the two-stage microcooler characterization set-up. (HPC: high pressure control; LPM: low pressure meter; MFM: mass-flow meter; PCB: printed circuit board).

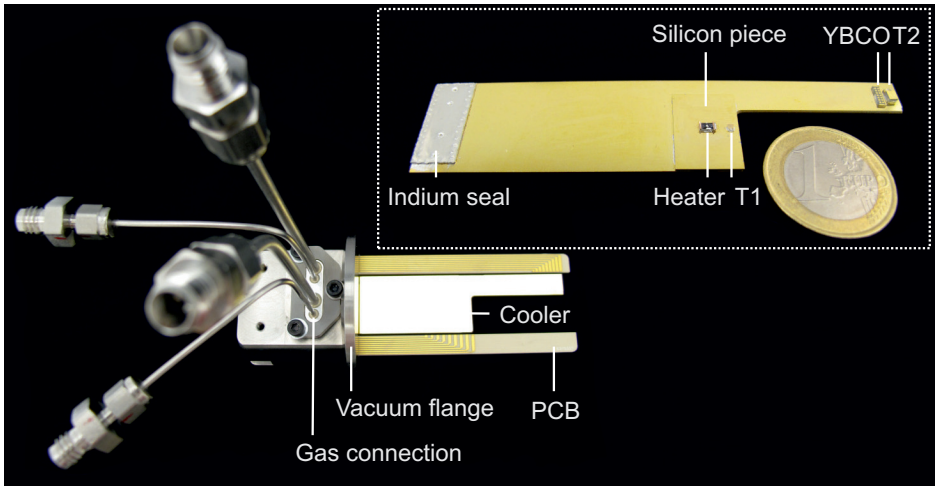

Figure 3.3: Photograph of the two-stage microcooler mounted into a vacuum flange and surrounded by a PCB. The inset shows the microcooler with two temperature sensors, a heater, a silicon piece and an YBCO film. A euro coin (diameter about 23 mm) is shown for size comparison.

the nitrogen stage and the pre-cooler to create a uniform temperature along the pre-cooler. The indium seal is used to make leak-tight connections between the gas inlets and outlets of the microcooler and the gas tubes connected to pressurized gas bottles.

3.2.2 Cool-down and performance of the microcooler

Figure 3.4a shows cool down curves for the nitrogen and hydrogen stages. In this experiment, the high and low pressures of the gas in the nitrogen stage are 8.5 and 0.10 MPa and in the hydrogen stage 8.0 and 0.10 MPa. The corresponding mass-flow rates measured on the low-pressure side of each stage are shown in Figure 3.4b. The temperature of the nitrogen stage (T1) decreases from 295 to 94 K in about 20 minutes. With decreasing temperature, the mass-flow rate of the nitrogen stage increases from 6.0 to 20.4 mg s^{-1} due to the density and viscosity being temperature dependent. After 20 minutes, the mass-flow rate fluctuates at around 17.5 mg s^{-1} indicating that liquid is formed in the JT expansion. The temperature of the hydrogen stage (T2) increases a little at the beginning, which is consistent with our simulations [49] and due to the inversion temperature of hydrogen gas being below ambient. After about 5 minutes, T2 drops gradually due to the longitudinal conduction from the cold end of the hydrogen stage to the pre-cooler. When T2 is lower than the inversion temperature of hydrogen (205 K), the cold end cools down by the JT expansion of the hydrogen gas. At this point, the middle section of CFHX III is at a slightly higher temperature than its both ends. The heat capacity of this middle section limits the rate at which T2 decreases. After about

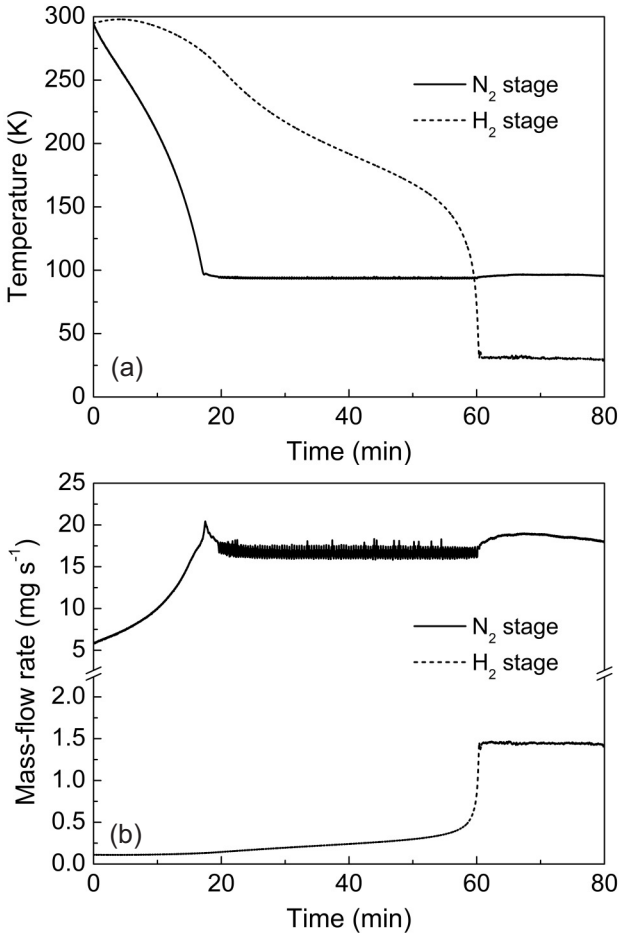

Figure 3.4: Measurements of the two-stage microcooler. (a) Cold-end temperatures of both stages versus time. (b) Mass-flow rates of both stages versus time.

50 minutes, T2 drops steeply and reaches 30 K in about 10 more minutes. The mass-flow rate of the hydrogen stage in this process increases from 0.1 to 1.4 mg s^{-1} again caused by the temperature dependence of the density and the viscosity of the gas. In the steady state of this experimental setting, the two-stage microcooler maintains a constant temperature of 96 K at the nitrogen stage and 30 K at the hydrogen stage. The mass-flow rates in the two stages are 17.9 and 1.4 mg s^{-1}, corresponding to gross cooling power of 311 and 136 mW, respectively. The parasitic heat load on the nitrogen stage is estimated to be 85 mW [49], and the remaining cooling power of this stage (226 mW) is used to precool the hydrogen gas. No net cooling power remains at the nitrogen stage in this setting. The estimated parasitic heat load on the hydrogen stage is 64 mW, resulting in a net cooling

power at 30 K of 72 mW.

3.2.3 YBCO film resistance

For demonstration purposes, a superconducting YBCO film is attached to the hydrogen stage evaporator (evaporator II in Figure 2.7). The device adds additional parasitic losses to the microcooler that primarily consist of thermal radiation on the surface of the film and heat conduction through the bond wires connecting the film to the outside electronics. The resistance of the YBCO film is measured using the standard 4-point method. The heat conduction through the four bond wires made of 1% silicon and 99% aluminum with a diameter of 25 μm and a length of 5 mm is about 20 mW when T2 is 30 K. The radiation loss induced by the YBCO film is reduced by coating most of the surface of the YBCO film with a gold layer. The resistance of the YBCO film versus time and temperature are shown in Figure 3.5a and b, respectively. The resistance decreases gradually with decreasing temperature of the hydrogen stage. At about 90 K the superconducting phase transition occurs [50]. The small residual resistance in the superconducting state is caused by an offset error in the voltage amplifier. With this experiment, we demonstrate the integration of an electronic device to the microcooler and also cooling the device down to cryogenic temperature of 30 K.

3.3 Conclusions

In this chapter, the fabrication and the application potential of the microcooler are discussed. The microcooler is realized by using only micromachining technology. The microcooler consists of a stack of only three glass wafers in which microstructures are etched. Compared to earlier work in which stacks of seven wafers were applied, this substantially improves the fabrication yield of two-stage microcoolers. The working fluids of the first and second stages are nitrogen and hydrogen gas, respectively. The nitrogen stage cools down from 295 to 94 K in about 20 minutes and the hydrogen stage cools down from 295 to 30 K in 60 minutes. The high and low pressures of the nitrogen gas are 8.5 and 0.10 MPa, and those of the hydrogen gas are 8.0 and 0.10 MPa, respectively. At the steady state, the hydrogen stage has a net cooling power of about 72 mW at 30 K with a mass-flow rate of 1.4 mg s^{-1}. A superconducting YBCO film is attached to the evaporator of the hydrogen stage. The microcooler cools down to 30 K and during the cool-down the YBCO film turns to its superconducting state. This demonstrates the application potential of the microcooler for integration with electronic devices such as, infrared detectors, low-noise amplifiers and superconducting sensors.

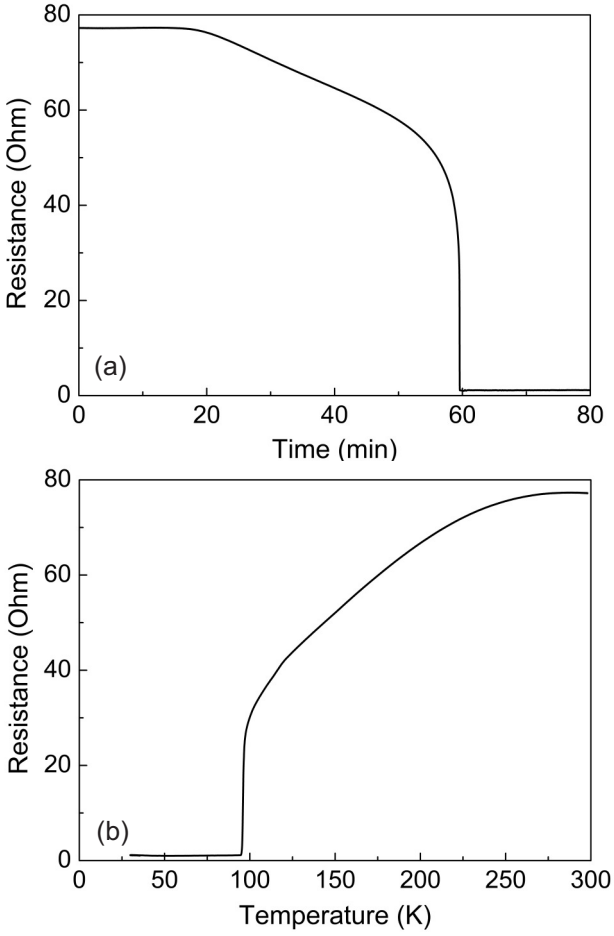

Figure 3.5: YBCO film resistance measurement versus time (a) and versus cold-end temperature of the hydrogen stage (b).

CHAPTER 4

Characterization

In this chapter, the characterization of the two-stage microcooler is discussed in details. Experimental results on cool down and cooling power are compared to dynamic modeling predictions.

4.1 Measurement set-up

The performance of the two-stage microcooler is measured with the setup shown in Figure 3.2 in chapter 3. The microcooler used in these measurements is shown in Figure 4.1. Temperatures are measured with Pt1000 sensors (T1 and T2) and a Dt471 diode sensor (T3) as shown in Figure 4.1. Surface mounted device resistors are used as heaters for supplying heat to the microcooler in order to measure the cooling power at the two stages. The temperature sensors and heaters are glued on the microcooler with conducting silver paint and connected to the PCB using bond wires made of 99% aluminum and 1% silicon with a diameter of 25 μm. The gas in- and outlet ports of the microcooler are connected to the tubes leading to pressurized gas bottles with indium seals for leak tightness. The microcooler as shown Figure 4.1 is used in the cooling-power experiments discussed in section 4.3. In the cool-down measurement described in section 4.2, the sensor T2 and the small silicon piece near T3 are not included.

4.2 Cool-down measurement and simulation

The microcooler was cooled down with the nitrogen stage operating between 8.5 and 0.11 MPa, and the hydrogen stage between 7.0 and 0.10 MPa. The high-pressure settings are larger than the selected operating pressures mentioned in chapter 2 (8.0 and 4.0 MPa). The high pressures are increased to compensate for the higher parasitic losses due to the sensors glued on the microcooler and corresponding bond wires. For the same purpose, the low pressure of the nitrogen stage is reduced from the initial design value 0.60 to 0.11 MPa, to reach a lower precooling temperature and thus to obtain a higher gross cooling power at the hydrogen stage. The low pressure of the hydrogen stage is reduced from the initial design value 0.57 to 0.10 MPa to reach the lowest possible temperature. The available cooling power of the hydrogen stage is measured when the low pressure of

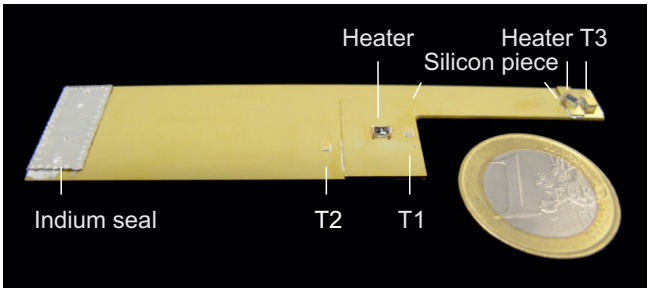

Figure 4.1: Photograph of the two-stage microcooler with a gold layer, two heaters, two silicon pieces and three temperature sensors. A euro coin (diameter about 23 mm) is shown for size comparison.

the hydrogen stage is set at 0.57 MPa.

The temperature readings of T1 and T3 were recorded under cool down indicating the temperatures at the nitrogen and hydrogen evaporator positions. Figure 4.2 shows the cold-end temperatures and the measured mass-flow rates versus the time. The measured cold end of the nitrogen stage cools down from 295 to 94 K in about 20 minutes while its mass-flow rate increases from 6.1 to 21.7 mg s^{-1} and fluctuates at around 17.5 mg s^{-1} after 20 minutes. The cool-down time of the hydrogen stage from 295 to 30 K is about 60 minutes. With decreasing cold-end temperature, the measured mass-flow rate of the hydrogen stage increases from 0.1 to 1.6 mg s^{-1} and then fluctuates at 1.3 mg s^{-1} eventually. Figure 4.2a also shows the simulated cool-down curves based on a dynamic model that we presented in chapter 2. The simulation is compared to the experimental results further on in this section.

Figure 4.3 shows the measured and calculated mass flow rates of the nitrogen (a) and the hydrogen (b) stages versus the corresponding cold-end temperatures. The mass-flow rate for fully developed, laminar flow through a rectangular channel can be calculated as:

$$\dot{m}(p,T) = \frac{wh^3}{12l}\int_{pL}^{pH}\frac{\rho(p,T)}{\mu(p,T)}dp \tag{4.1}$$

where w, h and l are the width, height and length of the restriction, respectively, and pH and pL are the high and low pressures, respectively. $\rho(p,T)$ is the density and $\mu(p,T)$ the viscosity which both are pressure- and temperature-dependent. With fixed restriction dimensions, the mass-flow rate is determined by the pressure and temperature profile along the restriction. The pressure profile is assumed to be linear, while the temperature profile can be evaluated using two types of assumptions. One assumption is that the restriction has a constant temperature equal to that of the evaporator, which was adopted in chapter 2. The other assumption is that the JT expansion is adiabatic and thus isenthalpic [51]. Figure 4.3 shows the measured and predicted mass-flow rates versus cold-end temperature for nitrogen and hydrogen stages. Compared to the mass-flow rate predicted based on the isothermal expansion, the calculated mass-flow rate trend by using the isenthalpic expansion assumption fits better with the measured trend during the cool-down process. The measured mass-flow rate of each stage increases with decreasing cold-end temperature because the density and viscosity of the gas are temperature dependent. As the cold end of each stage approaches its lowest temperature, the mass-flow rate starts to deviate from the theoretical trend; it first increases and then decreases. This can be explained by the fact that two-phase flow is formed in the evaporator. When two-phase flow returns into the CFHX connected with the evaporator, the high-pressure fluid is cooled down further in an unpredictable manner. The calculated isenthalpic mass-flow rate fits well with the measured trend during the cool-down process. As indicated by the Eq. 4.1, the mass-flow rate is proportional to the cube of the restriction height. A good fit to the measurements is obtained for a restriction height of 1160 nm whereas the design value was 1100 nm. When two-phase fluid starts to form, the calculated isenthalpic mass-

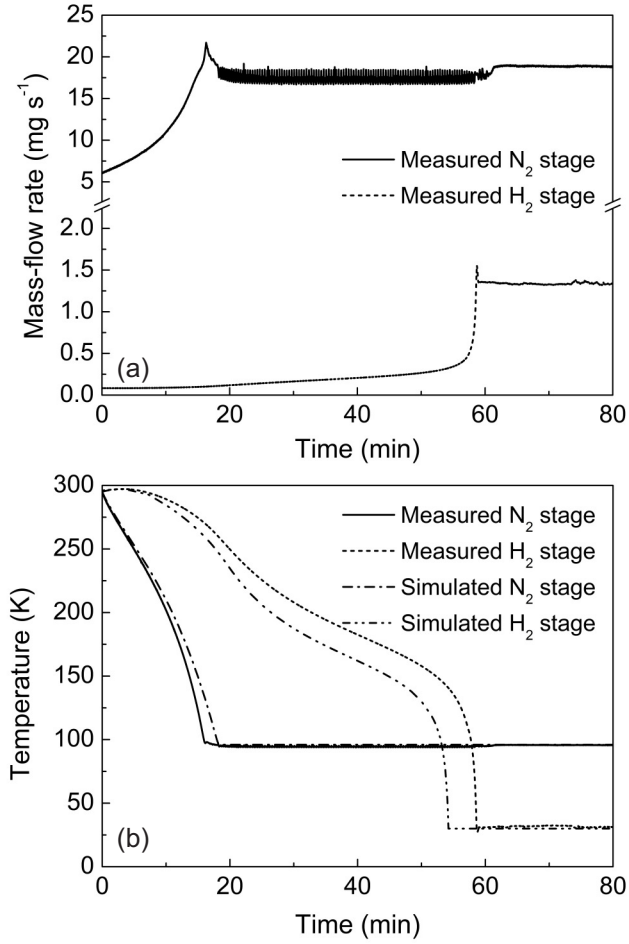

Figure 4.2: Measurement and simulation of the cool down of the two-stage microcooler. (a) Cold-end temperatures of both stages. (b) Mass-flow rates of both stages.

flow rate deviates from the measured value and can be used for first-order estimates only.

The simulated cool-down curves of both stages in Figure 4.2 which are calculated based on our dynamic model were discussed in chapter 2. The only distinction compared to the earlier model is that in the present model the heat exchange between CFHX I of the nitrogen stage and CFHX II of the hydrogen stage is included, corresponding to the actual cooler layout (see Figure 2.7 and Figure 3.1). As discussed in section 3.1, there is no slit between CFHX I and CFHX II because this appeared to be a risky step in the production of the cooler.

The calculated cooling power of the hydrogen stage against its cold-end temperature

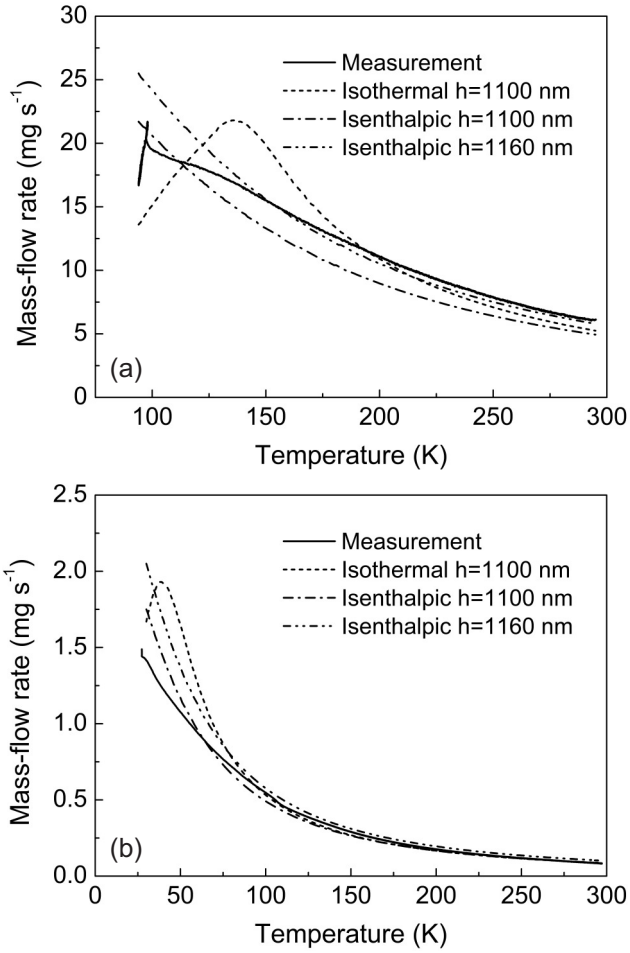

Figure 4.3: Mass-flow rate as a function of the cold-end temperature of each stage. (a) Nitrogen stage. (b) Hydrogen stage.

and the calculated parasitic loss that is caused by the heat conduction and thermal radiation to the sensors on the evaporator of the hydrogen stage are plotted in Figure 4.4. In this figure, the cooling power is composed of the power resulting from the JT expansion and the thermal conductance to the pre-cooler stage through the glass material.

Figure 4.4 can be used to explain the shape of the hydrogen-stage cool-down curve that is shown in Figure 4.2. In Figure 4.2, the cold-end temperature of the hydrogen stage increases a little in the beginning. This is because, at the start, the temperature of the hydrogen gas is above its inversion temperature (heating is obtained instead of cooling). After 5 minutes, the cold-end temperature of the hydrogen stage decreases because it

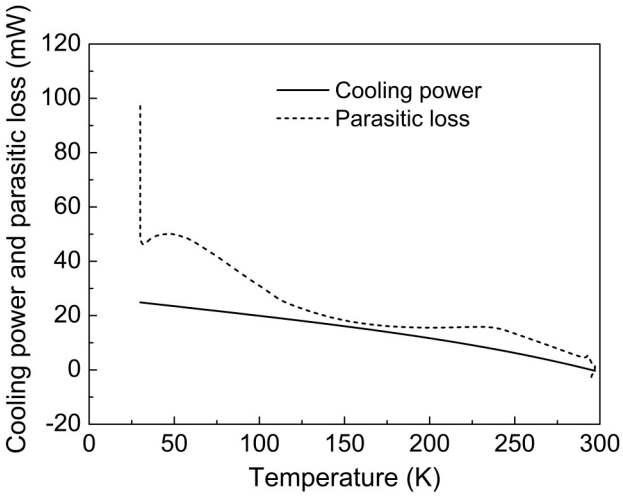

Figure 4.4: Cooling power and parasitic loss of the sensors on the hydrogen stage as a function of its cold-end temperature (In this figure the cooling power should be seen as the effective cooling power including the conductive heat flow through the hydrogen stage).

is cooled by the nitrogen stage through thermal conduction via the glass wafers. This thermal conduction increases in time because the cold-end temperature of the nitrogen stage decreases faster than that of the hydrogen stage. As a result, in Figure 4.2, the cool-down speed of the hydrogen stage increases until the cold end reaches a temperature of about 230 K. At that point, the nitrogen stage reaches its lowest temperature of 94 K and the temperature difference between pre-cooler and hydrogen-stage cold end starts to decrease. This causes a decrease in the thermal conduction and thus in the cool-down speed. When the cold-end temperature of the hydrogen stage gets below the inversion temperature of 205 K, cooling is obtained through the expansion of the hydrogen gas. As shown in Figure 4.4, the difference between the cooling power and the parasitic loss reaches a minimum when the cold-end temperature of the hydrogen stage is about 170 K. At that point, the mass-flow rate in the hydrogen stage starts to increase significantly (see Figure 4.3b). As a result, the cool-down speed of the hydrogen stage increases gradually (see Figure 4.2a). The final cool-down phase from about 125 K down to 30 K goes very fast because of the increasing mass-flow rate (Figure 4.3b). The evaporator cools down from 50 to 30 K in only a few seconds and because the surrounding cools more slowly, the conductive load form the surrounding glass to the evaporator increases. Therefore, the effective cooling power plotted in Figure 4.4 shows an initial dip at around 30 K. As in time the surrounding glass cools down, the effective cooling power increases to its static high value.

The measured cold-end temperatures of both stages do not reach the corresponding saturation points of 78.6 K at 0.11 MPa for the nitrogen stage and 20.3 K at 0.10 MPa for

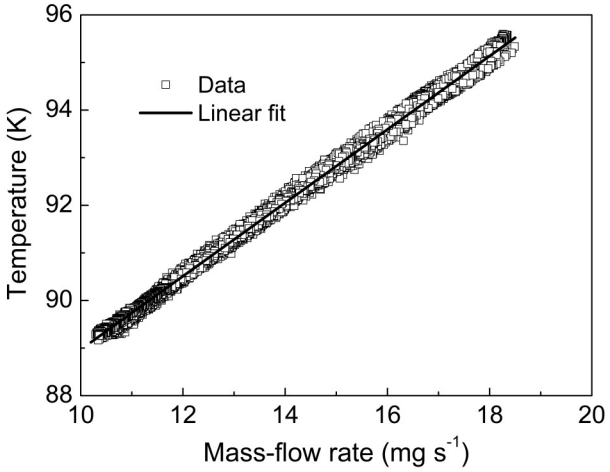

Figure 4.5: Measured cold-end temperature of the nitrogen stage (T1) versus mass-flow rate.

the hydrogen stage. One reason is the thermal resistance caused by the poor conductance of the glass wafer and the convective heat exchange between the working fluids and the glass. The thermal resistances of the silver paint and the silicon piece are negligible in this respect. The other reason of the discrepancy are the pressure drops along the low-pressure channels and the gas exits. As shown in Figure 4.5, the measured cold-end temperature of the nitrogen stage (T1) increases with increasing mass-flow rate. More mass flow leads to a higher pressure drop and thus to a higher boiling point of the nitrogen inside the evaporator. A linear fit to the experimental data has been made as:

$$T = 0.77\dot{m} + 81.3 \tag{4.2}$$

where the mass-flow rate ($\dot{m}$) is expressed in mg s^{-1} and the temperature T in K. When the mass-flow rate was zero, the pressure drop along the low-pressure channel and exit effect should be zero and the boiling point of nitrogen should be 78.6 K. The difference of 2.7 K compared to the value of 81.3 K in Eq. 4.2 is due to the thermal resistance between the temperature sensor and the nitrogen inside the evaporator.

4.3 Cooling power measurement and simulation

The available cooling power at the hydrogen stage was measured using the heater at that stage, at a constant low pressure of 0.57 MPa. In the measurement, the nitrogen stage was operated between a high pressure of 8.5 MPa and a low pressure of 0.11 MPa. After the hydrogen stage had reached about 30 K, the cooling power was determined by increasing the power dissipated in the heater to the point where the evaporator run

dry and the hydrogen stage started to warm up (T3 in Figure 4.1). Figure 4.6 shows the cooling powers of the hydrogen stage at different values of the high pressure. When the high pressure of the second stage is 6.0 MPa and the power of the heater is set at 32.5 mW, the cold-end temperature of the hydrogen stage stabilizes at about 32 K and the mass-flow rate at about 0.93 mg s^{-1}. The fluctuation in the mass-flow rate indicates two-phase flow in the evaporator. After 12 minutes, the heater power is increased to 35.0 mW and the temperature and mass-flow rate of the hydrogen stage stay constant for about 6 minutes. At t = 18 minutes, the cold-end temperature increases rapidly and the mass-flow rate decreases with increasing temperature. During this period, the mass-flow rate of the nitrogen stage decreases from 16.8 to 16.0 mg s^{-1} due to water molecule deposition inside the restriction [48]. Accordingly, the temperature of the nitrogen stage decreases a little according to Eq. 4.2. Using this method, the available cooling power of the hydrogen stage is estimated at about 32.5 mW with a high pressure of 6.0 MPa. When the high pressure of the hydrogen stage is lowered to 5.5 MPa, the required cooling power at the precooling stage decreases and as a result the mass flow and the temperature of the nitrogen stage decrease a little according to Eq. 4.2. Also, the nitrogen mass-flow rate starts to fluctuate which is caused by liquid nitrogen entering the return line of the CFHX. The available cooling power of the hydrogen stage at different high-pressure settings are summarized in Table 4.1 . With the high pressure of the hydrogen stage decreasing from 6.0 to 4.5 MPa, the available cooling power decreases from 32.5 to 6.1 mW and the corresponding hydrogen mass-flow rate decreases from 0.93 to 0.76 mg s^{-1}.

The cooling power available at the nitrogen stage was measured by incorporating the heater at the cold end of the nitrogen stage in a PID control loop in which the temperature of sensor T1 was stabilized at 95 K. In this experiment, the high pressure of the hydrogen stage was fixed at 6.0 MPa, and that of the nitrogen stage at 8.5 MPa. In this setting, the cooling power at the hydrogen stage was measured to be 30 mW (slightly lower than the value in Table 4.1, column a, because of the slightly higher nitrogen-stage temperature). As shown in Figure 4.7, the fluctuation in the mass-flow rate of the nitrogen stage disappears gradually with increasing heater power, which indicates that

Table 4.1: Cooling power of the hydrogen stage at different high-pressure set points, low pressure 0.57 MPa. The nitrogen stage was operated between 8.5 and 0.11 MPa.

Case	**a**	**b**	**c**	**d**
High pressure of H_2 stage (MPa)	6.0	5.5	5.0	4.5
Mass-flow rate of H_2 stage (mg s^{-1})	0.93	0.88	0.82	0.76
Cooling power of H_2 stage (mW)	32.5	25.2	15.6	6.1
Temperature of H_2 stage, T3 (K)	32	32	31	31
Temperature of N_2 stage, T1 (K)	94	93	93	93

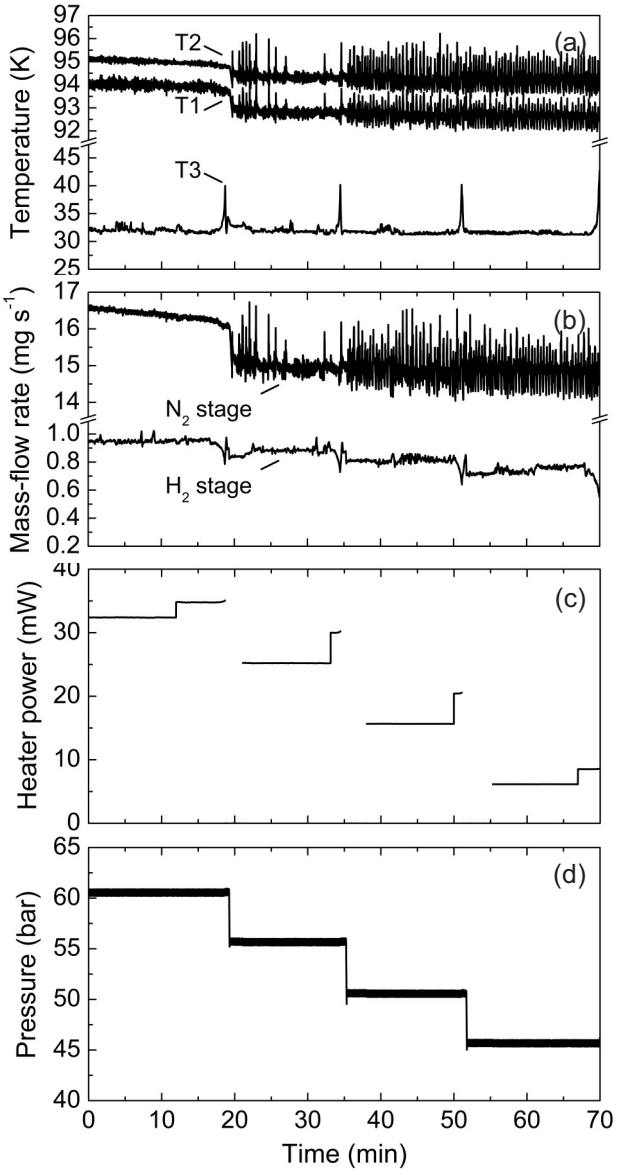

Figure 4.6: Cold-end temperatures, mass-flow rates and cooling power of the hydrogen stage with different high pressures and constant low pressure of 0.57 MPa.

liquid nitrogen evaporates during the process. During the period from 3 to 5 minutes, the mass-flow rate of the nitrogen stage increases from 16.3 to 17.5 mg s^{-1} with the cold-end temperature increasing from 94 to 95 K due to the temperature dependence of the density and the viscosity of nitrogen. After 5 minutes, the mass-flow rate of the nitrogen stage reduces slightly from 17.4 to 16.7 mg s^{-1} due to water molecule deposition inside the restriction [48]. The decreasing mass-flow rate results in a decrease in pressure drop along the low-pressure channel and thus in a lower temperature of the nitrogen stage according to Eq. 4.2. As a result, the heater power required for stabilizing T1 at 95 K increases, as can be seen in Figure 4.7. The net cooling power of the nitrogen stage is about 20.7 mW at a mass-flow rate of 16.7 mg s^{-1}. In the experiment, the cold-end temperature and mass-flow rate of the hydrogen stage stay constant at about 32 K and 0.93 mg s^{-1}, corresponding to Table 4.1 .

The method described above was applied to measure the available cooling powers of the nitrogen stage at different high pressures of the hydrogen stage as shown in Table 4.2. This table corresponds to Table 4.1 but now the nitrogen cold end is controlled at 95 K. Due to the water molecule deposition inside the restriction of the nitrogen stage [48], the mass-flow rate of the nitrogen stage varies over the separate experiments reported in Table 4.2. With measured mass-flow rates and temperatures, the net cooling powers of both stages are calculated using the above-mentioned dynamic model and the results are included in Table 4.2. The difference between the measured and the predicted net cooling power is only 2 to 4.0 mW in the considered measuring range.

Table 4.2: Cooling power of the nitrogen stage at different hydrogen-stage high pressures and nitrogen stage controlled at 95 K.

Case	**a**	**b**	**c**	**d**
High pressure of H_2 stage (MPa)	6.0	5.5	5.0	4.5
Set heat power of H_2 stage (mW)	30.0	22.8	11.8	4.7
Mass-flow rate of N_2 stage (mg s^{-1})	16.7	17.0	15.7	15.4
Cooling power of N_2 stage (mW)	20.7	37.0	61.0	83.9
Calc. cooling power of N_2 stage (mW)	24.7	35.0	63.6	80.6
Calc. cooling power of H_2 stage (mW)	27.0	18.8	10.3	2.0

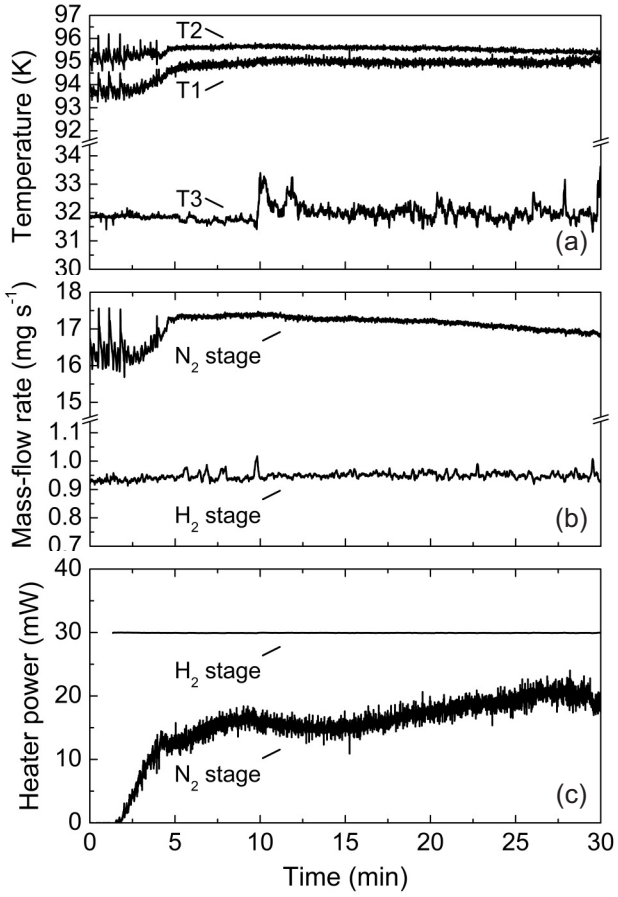

Figure 4.7: Cold-end temperatures, mass-flow rates and cooling power of nitrogen stage with hydrogen pressure between 6.0 and 0.57 MPa.

4.4 Conclusions

A two-stage Joule-Thomson (JT) micocooler with outer dimensions of 90.0 x 20.4 x 0.72 mm^3 has been developed and tested. It is operated with nitrogen gas in the first stage and hydrogen gas in the second. These stages cool down to about 94 and 30 K, respectively, using JT expansion in a restriction with a height of 1.1 μm. The nitrogen stage is typically operated between 0.11 MPa at the low-pressure side and 8.5 MPa at the high-pressure side. The hydrogen stage has a low pressure of 0.57 MPa, whereas the high pressure is varied between 4.5 and 6.0 MPa. In changing the pressure settings, the cooling power can more or less be exchanged between the two stages. These typically range from 21 to 84 mW at 95 K at the nitrogen stage, corresponding to 30 to 5 mW at 31-32 K at

the hydrogen stage. A dynamic model presented in chapter 2 was validated through the comparison of simulations and measurements of typical cool-down curves and cooling powers under different operating conditions.

CHAPTER 5

Clogging phenomenon and mechanism analysis

A critical issue for the long-term operation of micromachined cryogenic coolers is clogging of the microchannels caused by the deposition of water that is present as impurity in the working fluid. In this chapter, a model is developed to describe the deposition process considering the diffusion and kinetics of water molecules. In addition, this process was imaged under cryogenic operation with a microscope and a high resolution camera. These imaging results correspond well with the modeling predictions. Measures for preventing microcooler channels from clogging based on the model are discussed and verified through experiments.

5.1 Introduction

The long-term performance of microcoolers is limited by clogging of the microchannels caused by the deposition of impurities in the working fluid [11,22,52,53]. Lerou et al. [54] imaged the deposition of water molecules inside the CFHX of a microcooler during operation. They postulated that the deposited ice detached from the CFHX surface due to the gas flow, and then migrated to the restriction thus blocking the flow. The field of view of the camera used in their measurement setup did not provide adequate information of the clogging process in the restriction. This chapter focuses on the microscopic observation of the deposition of water molecules and subsequent sublimation inside the restriction and provides furthers insight in the mechanism of clogging in microchannels. Based on the findings we have suggested preventive measures of clogging in microcoolers and also have demonstrated through experiments the notable effect of the proposed measures.

5.2 Observation of clogging phenomenon

The microcooler studied in this chapter is similar to that used by Derking et al. [55] with outer dimensions of 60.0 x 9.5 x 0.72 mm^3. It is made of three glass wafers (see Figure 5.1a). The thicknesses of the top, middle and bottom wafers are 400, 145 and 175 μm, respectively. The high and low-pressure channels with a height of 40 μm are etched in the middle and bottom wafers. The channels contain pillars to limit the maximum mechanical stress caused by the high pressure. The high-pressure channel (HPC) ends in a flow restriction, which is extended to the evaporator volume and connected to the low-pressure channel (LPC). Thus, a CFHX is formed by the high and low-pressure channels. To reduce the radiative heat loss from the warm environment, a reflective gold layer is deposited on the entire outer surface of the microcooler except on one side of the evaporator to facilitate visual inspection of the microcooler channels. The JT flow restriction of the microcooler consists of 14 parallel slits 1.15 mm long, 0.14 mm wide and 1.1 μm high.

The working fluid is nitrogen gas of 5.0 purity, which is supplied from a pressurized gas bottle. The nitrogen gas flows through a pressure controller that regulates the high pressure. The nitrogen gas is purified with a getter filter to remove most impurities (especially water). The microcooler is placed in a small glass vacuum chamber as shown in Figure 5.1a, in which a vacuum pressure of less than 0.01 Pa is maintained. The distance between the microcooler and the outside of the vacuum chamber is about 10 mm, which is less than the working distance of the objective lens used to image the microcooler. At the outlet of the microcooler, the pressure and mass-flow rate of the nitrogen gas are measured.

The temperatures are measured with Pt1000 sensors (T1 and T2) as shown in Figure 5.1c. A surface-mount device resistor acts as a heater for controlling the cold-end temperature (T1). The temperature sensors and the heater are glued on the microcooler

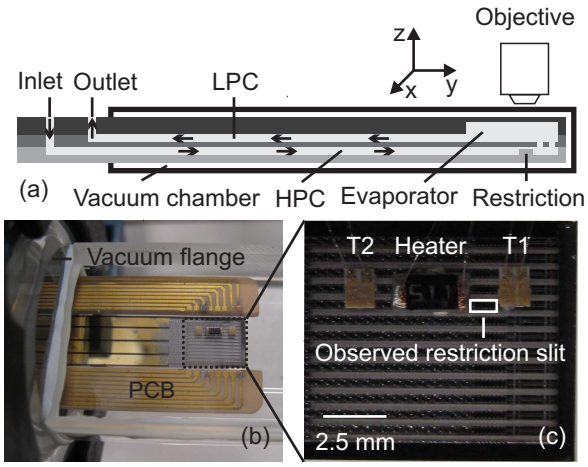

Figure 5.1: (a) Schematic cross-section of the measurement setup. (b) Photograph of the microcooler mounted into a vacuum flange and surrounded by a PCB. (c) The zoomed area without a gold layer with the observed restriction slit. (HPC: high pressure channel; LPC: low pressure channel; PCB: printed circuit board).

with thermally conducting silver paint and electrically connected to the printed circuit board (PCB) using bond wires made of 99% aluminum and 1% silicon with a diameter of 25 μm. The field of view of the camera is about 0.33 x 0.25 mm^2. The camera and the objective are mounted on an x-y stage for navigation along the length of the restriction slit and thus the whole restriction slit can be covered in 4 steps.

The microcooler is operated with high and low pressures of 8.0 and 0.63 MPa respectively. The lowest cold-end temperature attained by the microcooler is 102 K. Figure 5.2a presents the section of the restriction slit where ice formation is observed in the experiments. Figure 5.2 is obtained by combining three images taken along the length of the slit. Figures 5.2b-d show the locations of the deposition of water molecules in the observed restriction slit as the cold-end temperature is controlled at increasing temperature levels (140, 150, 160, 170 K, respectively). This location shifts towards the outlet of the slit as the cold-end temperature increases. In each case, the deposited ice quantity gradually increases in time which is ascertained by the darkening of the spot in the microscopic image at the location of the deposition. The cleavage and subsequent migration of the ice crystals as suggested by Lerou et al. [54] is not observed.

5.3 Ice crystal deposition: theory and modeling

The deposition rate of water molecules on the inner surface of the microcooler is determined by the diffusion of water molecules in nitrogen gas and the kinetic process

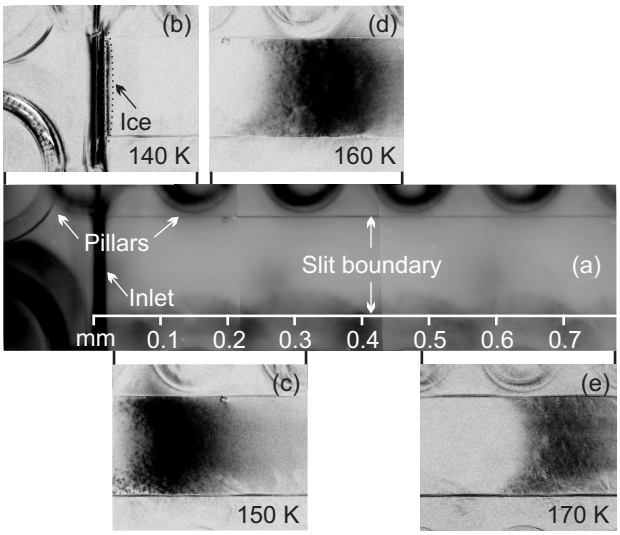

Figure 5.2: (a) Image of a part of the observed restriction slit made by combining three images taken along the restriction slit. The positions of the figures (b), (c), (d) and (e) show their relative locations in the restriction. The four figures indicate the locations of ice (dark spot in the restriction slit) at several cold-end temperatures, which are obtained by taking the difference of the image with ice and that of the corresponding field shown in (a) without ice. This difference is black-white inverted to obtain clearer pictures.

of water molecules on the surface. The deposition rate, $\dot{n}_{dep}$ (in mol m^{-2} s^{-1}), which is equal to the diffusion flux of water molecules in nitrogen gas can be expressed by Fick's law [31]:

$$\dot{n}_{dep} = D_{12}\frac{p_c - p_b}{0.5hRT} \tag{5.1}$$

where p_c and p_b (in Pa) are the partial pressures of water in the center and near the boundary of the channel,respectively; h is the channel height; R (in J K^{-1} mol^{-1}) is the universal gas constant and T (in K) is the temperature of the nitrogen gas in the channel. The diffusion coefficient of water molecules in nitrogen gas (D_{12}, m^2 s^{-1}) is estimated using the Chapman-Enskog theory [56] and a modified equation for high pressures proposed by Riazi and Whitson [57].

The proportionality constant D_{12} (m^2 s^{-1}) is the mass diffusivity of species 1 into 2 (i.e. water into nitrogen discussed in this chapter). The mass diffusivity of a binary gas mixture at low to moderate pressures pressures (less than 1.5 MPa), D^*_{12}, can be estimated using kinetic theory , resulting in the following relation [56]:

$$D^*_{12} = C\frac{T^{3/2}}{pl^2_{1,2}\Omega_D}\sqrt{\frac{M_1+M_2}{M_1M_2}} \tag{5.2}$$

where $C = 1.955 \cdot 10^{-24}$ (in $J^{3/2}K^{-3/2}mol^{-1/2}$) is constant, T is the absolute temperature (K), M_1 and M_2 are the molar masses of species 1 and 2 (kg mol^{-1}), p is the pressure (Pa), $l_{1,2}$ is a characteristic length of the mixture (m), and Ω_D is the dimensionless collision integral for diffusion. The characteristic length ($l_{1,2}$) is estimated according to the average of the Lennard-Jones 12-6 potential characteristic lengths for species 1 and 2 are provided by Poling et al. [56]. The collision integral for diffusion (Ω_D) is a function of the dimensionless temperature. One analytical approximation for Ω_D given by Neufield et al. [58] is:

$$\Omega_D = \frac{1.06036}{\tilde{T}^{0.1561}} + \frac{0.1930}{\exp\left(0.47635\tilde{T}\right)} + \frac{1.03587}{\exp\left(1.52996\tilde{T}\right)} + \frac{1.76474}{\exp\left(3.89411\tilde{T}\right)} \tag{5.3}$$

where

$$\tilde{T} = k_B T / \varepsilon_{12} \tag{5.4}$$

where k_B is Boltzmann constant, T is the absolute temperature and ε_{12} is a characteristic mixture energy parameter, which can be estimated in terms of Lennard-Jones 12-6 potential characteristic energies for species 1 and 2 (ε_1 and ε_2) according to:

$$\varepsilon_{12} = \sqrt{\varepsilon_1 \varepsilon_2} \tag{5.5}$$

The value of the Lennard-Jones 12-6 potential characteristic energy for many species are available in [56].

At high pressures, the mass diffusivity of a binary gas mixture no longer varies inversely with pressure as suggested by Eq. 5.2 due to the deviation from an ideal gas. An estimation method suggested by Riazi and Whitson [57] is:

$$\frac{\rho D_{12}}{\rho^* D_{12}^*} = 1.07 \left(\frac{\mu}{\mu^*}\right)^{b+cp_r} \tag{5.6}$$

where ρ, μ are the density and viscosity at the actual pressure and temperture, respectively. The superscript $*$ refers to the low-pressure case in which D_{12}^* is given by Eq. 5.2 with temperature and pressure chosen at a specific reference case. Here, the reference case is set at 300 K and 101.325 kPa, with ρ^* and μ^* the density and viscosity under these conditions. In the exponent, p_r is the reduced pressure, defined as the ratio of the actual pressure to the critical pressure.

$$b = -0.27 - 0.38\varpi \tag{5.7}$$

$$c = -0.05 + 0.10\varpi \tag{5.8}$$

where ϖ is the acentric factor, a pure component constant defined by Pitzer et al. [59]:

$$\varpi = -\log_{10}\left(p_r^{sat}\right) - 1 \tag{5.9}$$

where $p_r^{sat} = p^{sat}/p_{crit}$ is the reduced saturated vapor pressure at the reduced temperature $T_r = T/T_{crit} = 0.7$.

The kinetic process of water molecules on the surface is described using the Hertz-Knudsen-Langmuir theory [60–62]:

$$\dot{n}_{dep} = \alpha \frac{p_b - p_{sat}}{\sqrt{2\pi MRT}} \tag{5.10}$$

where p_{sat} (in Pa) is the equilibrium pressure of water molecules on the surface of the channel; M (in (kg mol^{-1}) is the molar mass of water. In the relevant temperature range of the microcooler, the values of the accommodation coefficient can be represented as [63–67]:

$$\alpha = 9.72 \times 10^{-2} \exp(232/T) \tag{5.11}$$

Combining Eq. 5.1 and Eq. 5.10, we obtain:

$$\dot{n}_{dep} = (p_c - p_{sat}) / \left(\frac{0.5hRT}{D_{12}} + \frac{\sqrt{2\pi MRT}}{\alpha} \right) \tag{5.12}$$

Equation 5.12 is used to simulate the deposition of water molecules along the length of the restriction at several cold-end temperatures. In this simulation, the restriction slit is divided into several small elements (typically 100) of constant length. Within each element, the gas temperature and pressure are assumed constant as well as the gas properties. Besides, the assumptions in the model are: 1. The temperature profile along the restriction slit is linear; 2. The expansion along the restriction follows an isenthalpic process; 3. The surface of the restriction slit has the same temperature as the high-pressure gas inside it. The latter assumption is acceptable because the small hydraulic diameter of the slit (about 2.2 m) results in an extremely high heat-transfer coefficient. The above assumptions determine the pressure profile along the slit. Further inputs to the model are the inlet partial pressure of water, the pressures before and after expansion through the slit and the temperature after expansion.

5.4 Water partial pressure in gas supply

The initial partial pressure of water in the nitrogen gas supply was determined by placing a small piece of silicon on the microcooler covering the whole restriction area to provide a uniform temperature along the slit (see Figure 5.3). In that isothermal case, the deposition of ice will occur at the highest pressure in the slit, which is at the inlet.

In this experiment the high pressure was 8.7 MPa (pressure drop along CFHX negligible). It is observed that the mass-flow rate through the restriction did not decrease as long as the cooler tip was controlled at temperatures above 182.5 K as shown in Figure 5.4. At lower temperatures, clogging occurred. Since at 182.5 K the phase transition of water vapor into ice is at 8.6 mPa, we can estimate the inlet molar fraction

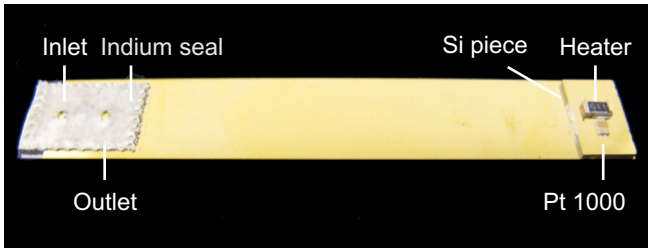

Figure 5.3: Single-stage microcooler with a silicon piece, a heater and a temperature sensor.

of water to be about 1.0 ppb. For the nitrogen gas with a pressure of 8.0 MPa as in the case of our clogging experiments, the partial pressure of water can thus be estimated at 8.0 mPa.

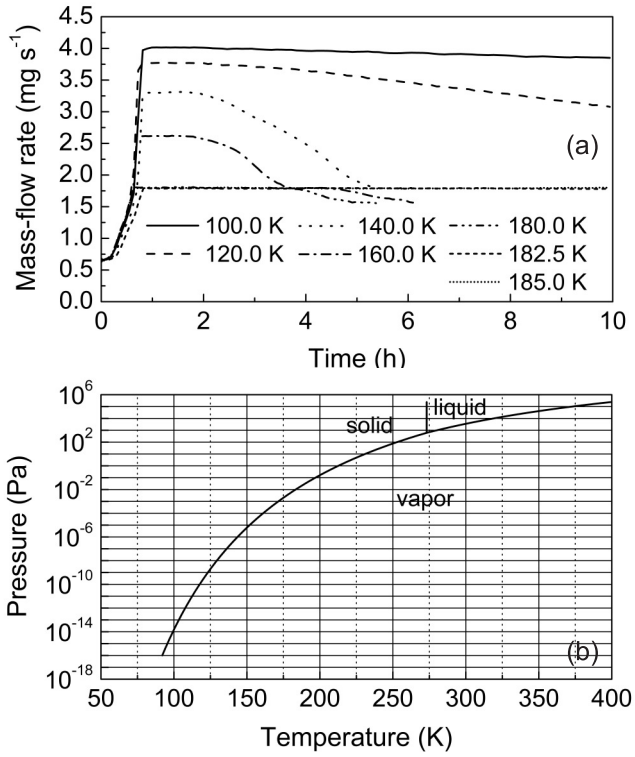

Figure 5.4: (a) Mass-flow rates versus time at different cold-end temperatures. (b) Phase diagram of water [13].

5.5 Clogging simulations and experiments

The ice growth rate along the restriction is simulated at several cold-end temperatures. Following the experimental settings, the pressures before and after expansion in the model are 8.0 and 0.86 MPa, respectively (pressure drop in the low-pressure CFHX channel estimated at 0.23 MPa with a constant mass-flow rate of 10 mg s^{-1}). Figure 5.5 shows the simulated ice growth rate along the restriction slit at several cold-end temperatures. Due to the clogging, the mass-flow rate will decrease in reality, which will cause a decrease in the ice growth rate. The decreasing mass-flow rate has an influence on the pressure drop in the low-pressure CFHX channel, which will affect the location of the clogging in the restriction. To keep the cold-end temperature of the microcooler at a certain value, the minimum mass-flow rate is about 75% of its initial maximum value. In this case, the effect of the decreasing mass-flow rate on the location of clogging in the 1.15 mm long restriction is less than 0.01 mm. As shown in Figure 5.5a-d, at 140 K the ice mainly forms at the inlet of the restriction and the ice peak shifts towards the outlet of the restriction at increasing cold-end temperature. This corresponds well with the experimental observation depicted in Figure 5.2.

Figure 5.6 compares the locations of the ice peaks in simulations and experiments. The trends are clearly the same and the difference is caused by the fact that the simulation is based on isenthalpic expansion implying an adiabatic process. In reality, however, the process is not adiabatic since the high-pressure gas is precooled by the returning low-pressure gas. Therefore, the gas temperature at the entrance of the restriction in reality

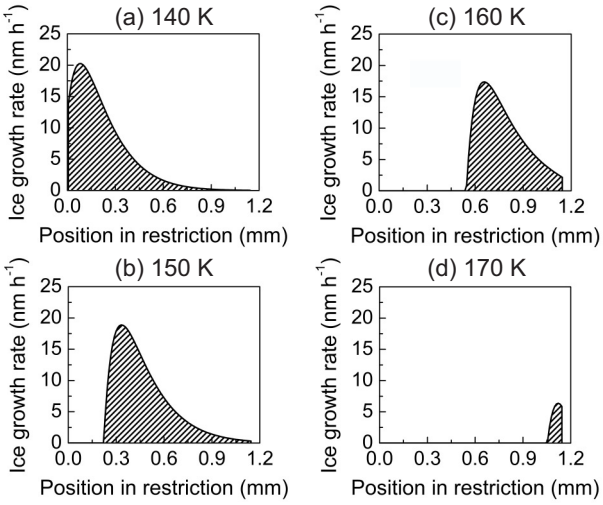

Figure 5.5: Simulated ice growth rate along the restriction slit with a length of 1.15 mm at several cold-end temperatures.

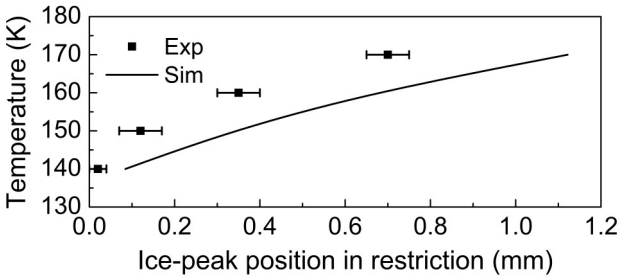

Figure 5.6: Relation between ice-peak position and cold-end temperature in simulation (Figure 5.2) and experiment (Figure 5.5). The error bar indicates the length of the dark spot shown in Figure 5.2b-e.

will be lower than in the simulations and thus in reality the ice peaks will be closer to the inlet of the slit.

As also measured by Lerou et al. [54] clogging causes the mass-flow rate to decrease and as a result the cooling power decreases. When the cooling power can no longer compensate for parasitic heat losses (conduction and radiation), the microcooler warms up and the ice sublimates. Figure 5.7 shows a sequence of images showing the deposition of water molecules and the subsequent sublimation in the observed restriction slit. From point 1 to 2, the mass-flow rate decreases from 2.3 to 1.4 mg s^{-1} due to the clogging of the slit. At point 3, the mass-flow rate reaches a minimum of 0.6 mg s^{-1} at cold-end temperature 218 K. At that point sublimation occurs and the mass-flow rate starts to increase. From point 4 to 5 and 6, the deposited ice gradually sublimates to vapor and the mass-flow rate increases to 4.9 mg s^{-1}. With the restriction warming up, the ice does not migrate, but rather sublimates leaving no traces in the restriction.

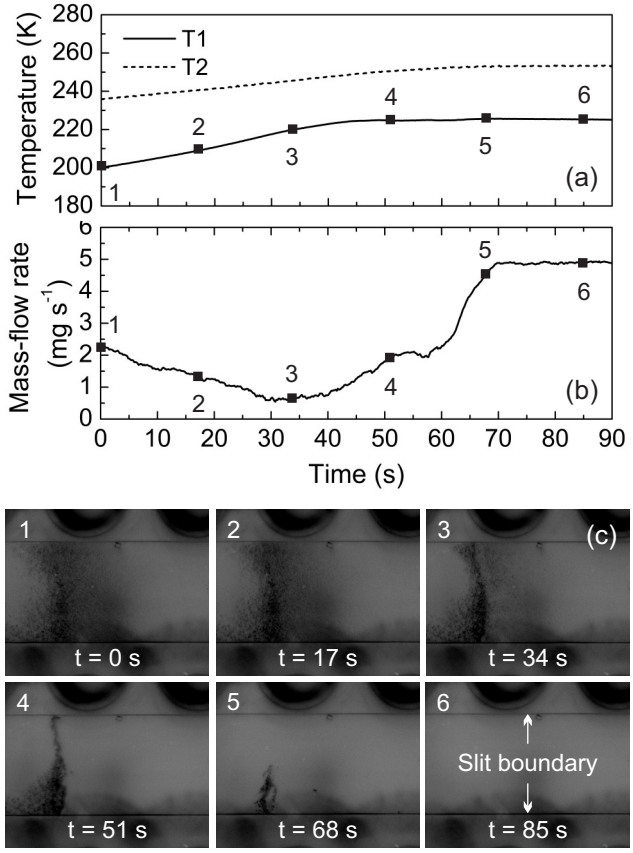

Figure 5.7: Temperature (a) and mass-flow rate (b) recorded during clogging (points 1-3) and subsequent declogging (points 3-6). In (c) six frames are shown of the camera recording taken at moments that correspond to the points 1-6.

5.6 Measures against clogging

The deposition of water molecules in the microcooler mainly depends on the inlet partial pressure of water and the temperature profile along the microcooler. To reduce the clogging rate, the first measure is to decrease the water fraction in the supply gas using a getter filter. The second measure is to shift the location of the major deposition of water molecules from the restriction to the CFHX by changing the temperature profile along the microcooler. For that purpose a sufficiently large part of the CFHX in front of the restriction needs to be cooled to below the ice-deposition temperature (in our case about 180 K). That is why the evaporator is extended to cover part of the high-pressure channel as is shown in Figure 5.1a [68]. Because of the poor thermal conductance of glass, this approach is more successful when using a piece of well-conducting material (such as

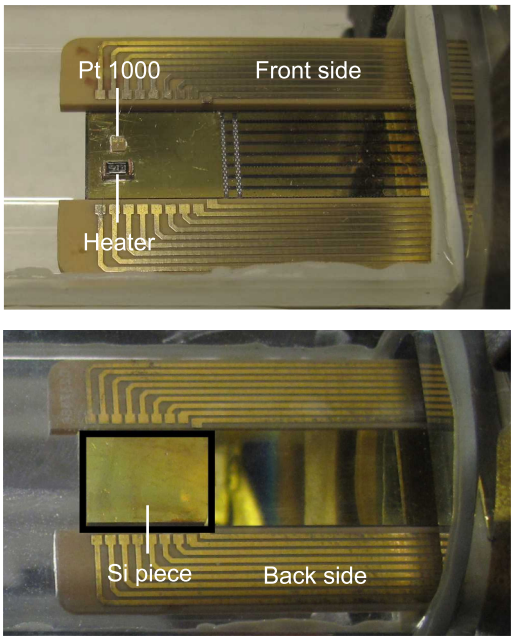

Figure 5.8: Photograph of the microcooler mounted into a vacuum flange and surrounded by a PCB.

silicon) to make a thermal link between evaporator and the relevant part of the CFHX. The latter concept is verified by experiments. The microcooler in verification experiments (see Figure 5.8) has the same dimensions as the microcooler shown in Figure 5.1(b). The microcooler is operated with nitrogen gas between 8.0 and 0.63 MPa. With the cold-end temperature decreases from 295 to 105 K, the mass-flow rate increases from 3.5 to 15.4 mg s^{-1} as shown in Figure 5.9. By controlling the cold-end temperature at 105 K, a decrease in mass-flow rate is observed due to clogging, which causes the cooling power to decrease. After 11.0 hours, the cooling power can no longer compensate for parasitic heat losses, the microcooler warms up. To make a thermal link between the evaporator and the relevant part of the CFHX, a silicon piece of 13.0 x 9.5 x 0.5 mm^3 is glued on the back side of the microcooler. With the same pressure settings, the microcooler with the silicon piece has an initial mass-flow rate of 17.2 mg s^{-1} at 105 K. The difference in the mass-flow rate is caused by the different temperature profile along the restriction. The microcooler with the silicon piece can keep the cold-end temperature at 105 K for 51.8 hours. This verifies that the clogging rate can be reduced by changing the temperature profile along the microcooler.

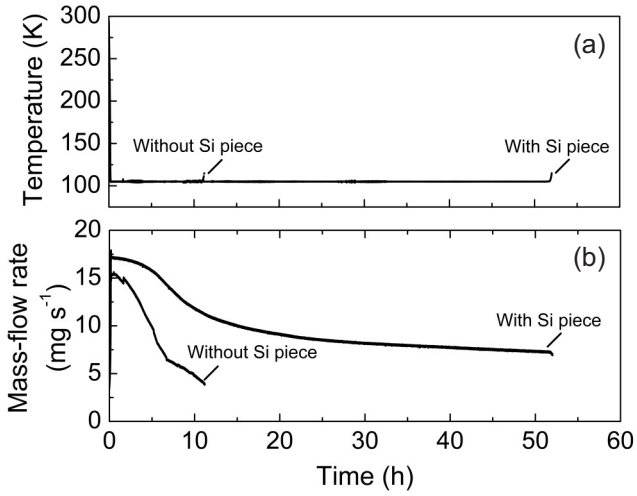

Figure 5.9: Measurements of the microcooler without and with a silicon piece. (a) Cold-end temperatures versus time. (b) Mass-flow rates versus time.

5.7 Conclusions

A major hurdle in long-term operation of JT microoolers is the clogging caused by the deposition of water that is present as impurity in the working fluid. In this chapter, the mechanism of the clogging phenomena is investigated through experimental observation and theoretical explanation. It is found that the position and the rate of the deposition of water molecules in the microcooler mainly depend on the inlet partial pressure of water and the temperature profile along the microcooler. By using a getter filter, most impurities (especially water) from nitrogen gas are removed to a minimum value of about 1.0 parts per billion (ppb). By changing the temperature profile along the microcooler using a silicon piece, the operating time of the microcooler under test at 105 K extends from 11 to 52 hours.

CHAPTER 6

Utilization for cooling low-noise amplifiers

The sensitivity of antenna systems increases with increasing active area, but decreases at higher noise figure of the low-noise amplifier (LNA). Cooling the LNA locally results in significant improvement in the gain and in lowering the noise figure of the LNA. Micromachined JT coolers can provide a cryogenic environment to the LNA. They are attractive because they have no cold moving parts and can be scaled down to match the size and the power consumption of LNAs. In this chapter, the utilization of microcoolers for cooling low-noise amplifiers is discussed based on the Square Kilometre Array case as an example. This study was performed together with Roel Witvers of ASTRON.

6.1 Introduction

The Square Kilometre Array (SKA) [69] is designed to detect very weak signals at frequencies from 70 MHz to 10 GHz in three bands (low: 70-450 MHz, middle: 0.45-1.4 GHz, high: 1.2-10 GHz). In the low and middle parts, two different types of aperture arrays will be adopted. Dish antennas will be used to observe signals in the high part of the frequency band. The purpose of this chapter is to explore the improved performance of the telescope in the middle frequency band by cooling the low-noise amplifier (LNA).

The telescope sensitivity is determined by the ratio of the active area to the noise temperature of the entire receiver. In the receiver system, the noise temperature is primarily determined by the first stage LNA [70], which is a key component placed at the front-end of a radio receiver circuit. The reduction in noise temperature of a LNA by cryogenic cooling provides an effective way to improve the receiver sensitivity [71]. From the noise model developed by Pospieszalski [72], the minimum noise temperature of a field effect transistor chip can be expressed by:

$$T_{min} = 2\frac{f}{f_T}\sqrt{r_t T_g g_{ds} T_d} \tag{6.1}$$

where T_{min} is minimum noise temperature, f is the frequency of radio waves, f_T is the intrinsic cut-off frequency, r_t is the total resistance including parasitic resistances of gate and source and the intrinsic gate resistance, g_{ds} is the drain-to-source conductance, T_g and T_d are equivalent gate and drain temperature, respectively. T_g is approximately equal to the physical temperature of a device.

The performance improvement of cryogenically-cooled LNAs has been demonstrated in many studies [73–75]. For the SKA telescope, cryogenic cooling reduces the active area required for a given telescope sensitivity or allows higher sensitivity with the same active area. It is not necessary to cool the whole radio receiver for this application, but only the localized LNA chip. A miniature cryogenic cooler is attractive for the local cooling of the LNA chip. Localized LNA thermoelectric cooling has been investigated by Schreuder and Bij De Vaate. The noise figure of the LNA at 2.6 GHz reduced from 1.40 dB at 293 K to 1.15 dB when the LNA was cooled down to a temperature of 250 K [76]. Compared to thermoelectric coolers, JT coolers can offer lower cold-end temperature. Besides, JT coolers are also suitable for miniaturization because they have no cold moving parts and therefore can be scaled down to match the size and the power dissipation of LNA chips [11, 52]. In this chapter, the utilization of JT microcoolers for cooling LNAs is investigated. As a demonstration, we have integrated a commercial gallium arsenide monolithic microwave integrated circuit LNA with a single-stage 110 K microcooler. It shows a 0.33 dB noise figure improvement in the frequency range between is 0.65 to 1.05 GHz. As indicated by Eq. 6.1, an even better performance of LNAs could be obtained by using 30 K microcoolers [78].

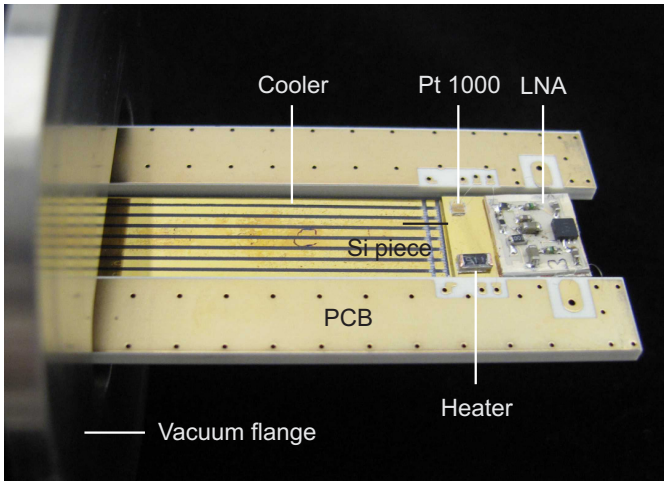

Figure 6.1: Photograph of the microcooler with a temperature sensor, a heater, a LNA and a silicon piece mounted into a vacuum flange and surrounded by a PCB.

6.2 Micro Joule-Thomson cold stage and LNA

The micromachined JT cooler is made from a stack of three glass wafers with dimensions of 60.0 x 9.5 x 0.72 mm^3. The microcooler is mounted into a vacuum flange and surrounded by a printed circuit board (PCB) as shown in Figure 6.1. The cold-end temperature of the microcooler is measured with a platinum resistor (Pt1000). A surface mounted device resistor is used as a heater to apply heat and thus to control the cold-end temperature of the microcooler. The LNA together with the temperature sensor and the heater is glued to a silicon piece that is thermally connected to the cold end of the microcooler with conducting silver paint similar to the procedure described by Derking et al. [51]. The function of the silicon piece is to uniformly distribute the heat and to reduce temperature gradients along the LNA. The temperature sensor, the heater and the LNA are electrically connected to the PCB with bond wires made of 99% aluminum and 1% silicon having a diameter of 25 μm. Both the temperature sensor and the heater are connected to the PCB with 2 bond wires. The LNA requires 7 bond wires consisting of 2 radio frequency (RF) signal wires, 4 ground wires, and 1 direct current (DC) wire.

The PCB transports the RF signals to the LNA attached on the cold end of the microcooler. The RF power losses associated with PCB transmission lines have a significant effect on a propagating signal in the radio frequency range. Some of the power losses are caused by its resistance, that is, ohmic or resistive loss. At high frequencies, the insulating material around the transmission line can also absorb energy from the alternating electric field and converts it to heat, which is called dielectric loss. The resistive and dielectric losses vary in proportion to the length of the transmission

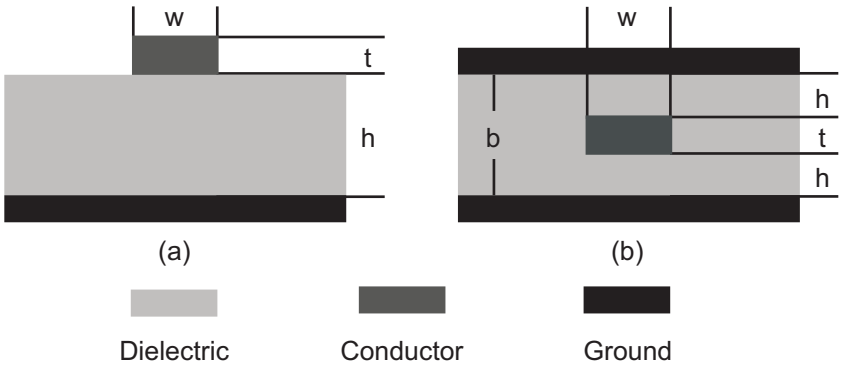

Figure 6.2: Typical two configurations of PCB. (a) Microstrip. (b) Stripline.

line. Therefore, a shorter transmission line means lower RF loss. When a signal is transmitted along a transmission line, some of the signal power may be reflected back to the transmitting device rather than being carried all the way along the transmission line to the receiver. The power losses will increase due to the signal reflection. To decrease the power losses caused by reflection, the characteristic impedance (Z_0) of the transmission line should be equal to the load impedance. For a uniform transmission line, the characteristic impedance is determined by the geometry and materials of the transmission line, where it does not depend on its length. The two most commonly used layout configurations on PCBs are microstrip and stripline as shown in Figure 6.2.

Microstrip is a layout configuration where a flat conductor is separated from a ground plane by a layer of dielectric material. This configuration has a dielectric surrounding the conductor on one side while air surrounding it on the other. The characteristic impedance of a microstrip is dependent on the width (w) of the conductor, the thickness (t) of the conductor, the dielectric constant (ε_r) of the material used, and the height (h) between the conductor and ground plane, given by [79]:

$$Z_{0,ms} = \begin{cases} Z_{0,ms1} & \text{for } w/h < 2 \\ Z_{0,ms2} & \text{for } w/h \geq 2 \end{cases} \tag{6.2}$$

where

$$Z_{0,ms1} = \frac{60}{\sqrt{\varepsilon_{re1}}} \ln\left(\frac{5.98h}{0.8w+t}\right) \tag{6.3}$$

$$Z_{0,ms2} = \frac{120\pi}{\sqrt{\varepsilon_{re2}}\,(w/h + 1.393 + 0.667\ln(w/h + 1.444))} \tag{6.4}$$

$$\varepsilon_{re} = \begin{cases} \varepsilon_{re1} & \text{for } w/h < 2 \\ \varepsilon_{re2} & \text{for } w/h \geq 2 \end{cases} \tag{6.5}$$

$$\varepsilon_{re1} = 0.475\varepsilon_r + 0.67 \tag{6.6}$$

$$\varepsilon_{re2} = \frac{\varepsilon_r + 1}{2} + \frac{\varepsilon_r - 1}{2\sqrt{1 + 10h/w}} \tag{6.7}$$

Stripline is constructed with a flat conductor suspended between two ground planes. The conductor and ground planes are separated by a dielectric. The approximate formula for the characteristic impedance of a stripline provided by [79]:

$$Z_{0,sl} = \begin{cases} Z_{0,sl1} & \text{for } w/(b-t) \geq 0.35 \\ Z_{0,sl2} & \text{for } w/(b-t) < 0.35 \end{cases} \tag{6.8}$$

where

$$Z_{0,sl1} = \frac{94.15}{\sqrt{\varepsilon_r}\left(\frac{w}{b}k + \frac{C_f}{8.854\varepsilon_r}\right)} \tag{6.9}$$

$$Z_{0,sl2} = \frac{60}{\sqrt{\varepsilon_r}} \ln\left(\frac{4b}{\pi d}\right) \tag{6.10}$$

$$k = 1/(1 - t/b) \tag{6.11}$$

$$C_f = \frac{8.854\varepsilon_r}{\pi}\left(2k\ln(k+1) - (k-1)\ln\left(k^2-1\right)\right) \tag{6.12}$$

$$d = \frac{w}{2}\left(1 + \frac{t\left(1 + \ln(4\pi w/t) + 0.51\pi(t/w)^2\right)}{\pi w}\right) \tag{6.13}$$

In the layout of stripline, the magnetic and electric field lines are confined to the dielectric in the space between the ground planes. Compared to microstrip, where some of the field lines propagate in air, stripline affords more isolation between adjacent circuit traces, supporting more densely integrated circuits. The propagation time of microstrip is shorter than that of stripline since the dielectric material has a higher dielectric constant than that of air.

The PCB shown in Figure 6.1 is a multilayer board with the RF and DC lines inside. The RF lines are laid out in the form of strip-line configuration to shield the RF signals from the environment and the flange. The loss of the RF lines will increase the overall noise figure of the LNA and thus needs to be as low as possible. The measured RF loss of the PCB is given in Figure 6.3.

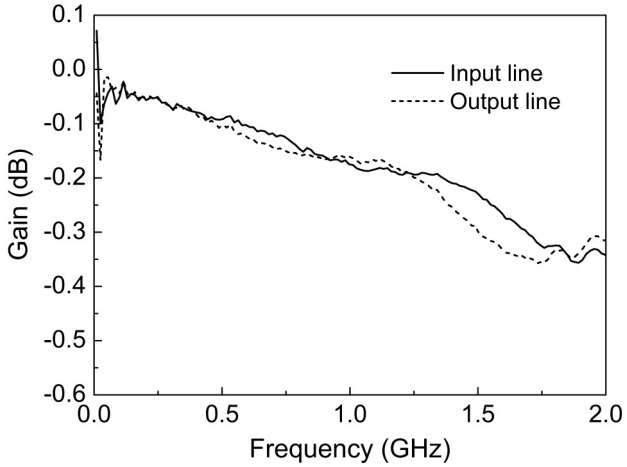

Figure 6.3: RF loss of the PCB in the setup of Figure 6.1.

6.3 Measurement

6.3.1 Measurement set-up

The working fluid, nitrogen gas, is supplied to the microcooler from a pressurized gas bottle. The inlet high pressure to the microcooler is controlled with a pressure control. The nitrogen gas is purified with a getter filter to remove most impurities (especially water) to about 1.0 ppb level to prevent clogging due to water deposition, see chapter 5. The outlet low pressure and mass-flow rate of the nitrogen gas are measured at the outlet of the microcooler. A pressure relief valve maintains a constant outlet pressure of 0.11 MPa and also prevents air from flowing into the system. A vacuum pressure of less than 0.01 Pa is maintained around the microcooler during the experiment.

6.3.2 Cool-down measurement

The operating low and high pressures of the microcooler are 0.11 and 8.5 MPa respectively. Figure 6.4 shows the measured cold-end temperature and mass-flow rate. From a room temperature of 295 K, the cold end cools to about 110 K in 18 minutes. As the cold-end temperature decreases to 125 K, the mass-flow rate increases from 4.2 to 15.3 mg s^{-1} due to the temperature dependence of density and viscosity of the nitrogen gas. When the cold-end temperature is lower than 125 K, the mass-flow rate decreases to 13.0 mg s^{-1} because liquid forms in the restriction. In the steady state, the mass-flow rate is constant at 13.8 mg s^{-1}.

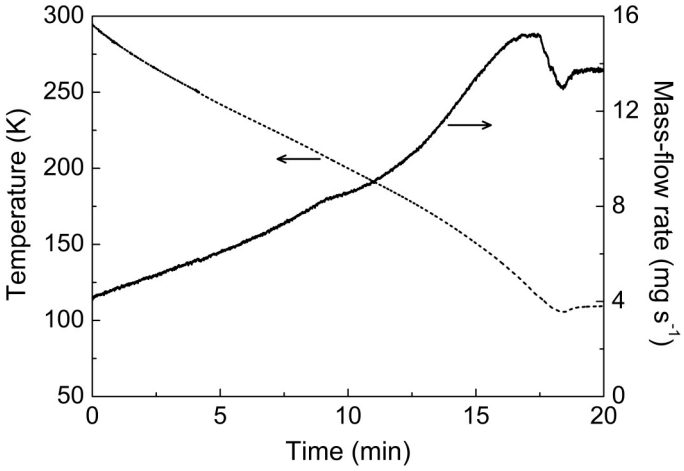

Figure 6.4: Measurement of the cool down of the microcooler.

6.3.3 Performance of LNA mounted on the microcooler

The net cooling power that can be used to balance the heat generated in the LNA is measured using a PID control loop that consists of a temperature sensor and a heater (indicated in Figure 6.1). At a controlled temperature of 115 K and a mass-flow rate of 15 mg s^{-1}, the measured net cooling power of the microcooler is about 43 mW as shown in Figure 6.5. At the cold-end temperature of 115 K, the estimated conductive heat flow through a total of 11 bond wires each with a length of 5 mm is about 38 mW, and the radiative heat flow to the LNA with dimensions of 10 x 10 x 0.5 mm^3 is about 47 mW. Therefore, the cooling capacity of the microcooler at 115 K is about 128 mW.

As shown in Figure 6.5, the LNA is switched on after about 2 minutes, and the supply voltage of the LNA at that point is set to 1.0 V with a power dissipation of 4 mW. The net cooling power of the microcooler reduces 4 to 39 mW accordingly. With the supply voltage increasing to 1.5 and 2.0 V, the net cooling power decreases to 28 and 14 mW. This means that the power dissipations of LNA are 15 and 29 mW with supply voltages of 1.5 and 2.0 V, respectively, which also match with the the product of applied voltage and the electric current read from the power supply. During the measurement, the temperature fluctuations are less than 0.5 K.

Figure 6.6 shows the measurement of the noise figure and gain of the LNA with a supply voltage of 2 V at 295 and 115 K in the frequency range between 0.65 and 1.05 GHz. The average noise figure of the LNA decreases from 0.83 to 0.50 dB when the cold-end temperature reduces from room temperature of 295 to 115 K. At room temperature, the gain decreases from 17.9 to 13.1 dB with the increasing frequency from 0.65 to 1.05 GHz. Upon cooling to 115 K, the corresponding increase in gain varies in

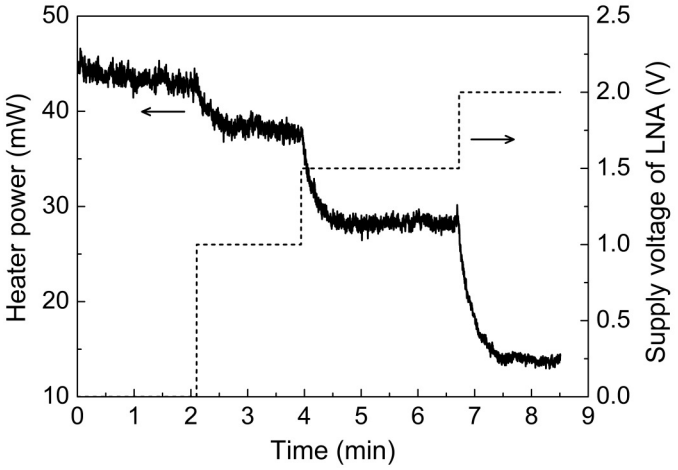

Figure 6.5: Measurement of the net cooling power of the microcooler with attached LNA operating at different supply voltages. The microcooler is controlled at 115 K with a mass-flow rate of 15 mg s^{-1}.

the range of 0.6 to 1.5 dB.

6.4 Discussion

By cooling the LNA from 295 to 115 K, the average noise figure decreases from 0.83 to 0.50 dB, corresponding to a reduction in the average noise temperature of the LNA from 61 to 35 K. The telescope sensitivity is proportional to the ratio of the active area to the noise temperature of the entire receiver. This implies that the active area of a telescope with a certain sensitivity can be reduced about 43% by using JT microcooling. The RF loss of the PCB is between 0.11 to 0.18 dB in the frequency range of 0.65 and 1.05 GHz as shown in Figure 6.3. Therefore, the effective improvement in noise figure due to the cooling system varies in the range of 0.15 to 0.22 dB. The RF loss of the PCB can be reduced by a better PCB material and/or a shorter RF line length. In the cooling system mentioned above, the RF line length is the distance between the cold end of the microcooler and the flange. To reduce the RF line length, the first measure is to separate the fluid and electrical feedthroughs by placing another flange with electrical feedthroughs on the side of the cold end of the microcooler. The second measure is to modify the microcooler geometry to a "U" shape with the cold end placed close to the warm-end flange. More improvements can be achieved by improving the impedance match between the PCB, bondwires and the LNA since the LNA is not performing optimally. Compared to the heat generated in the LNA, the conductive heat of the bond wires and the radiative heat of the LNA are relatively large. Therefore, the wires need further optimization based

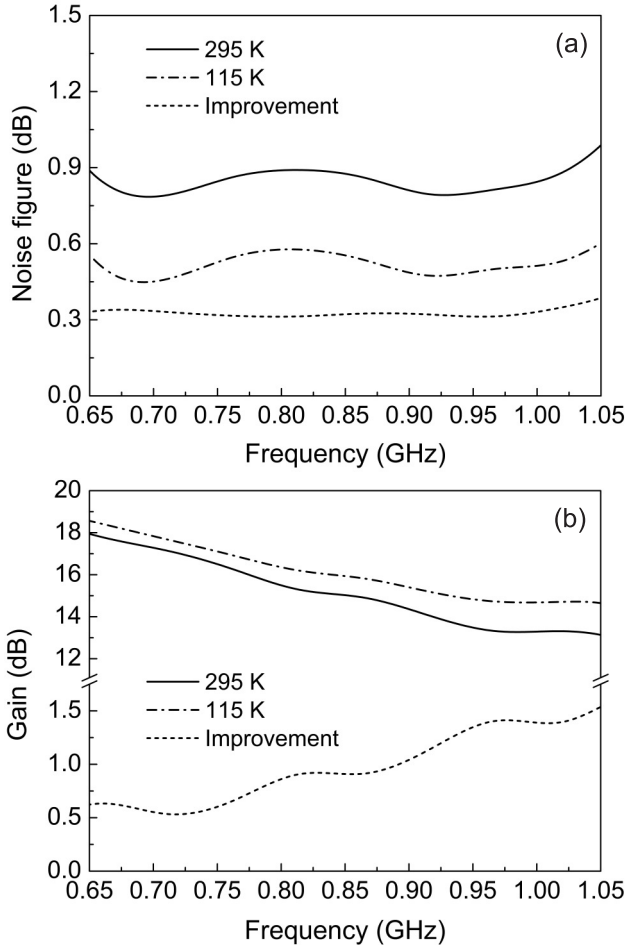

Figure 6.6: Noise figure (a) and gain (b) versus frequency at different temperatures.

on the acceptable impedance and the LNA chip should be made as small as possible to reduce the radiative loss.

6.5 Conclusions

In general, the performance of an antenna system can be improved by cooling the LNA stage in order to reduce the noise figure. Cooling the LNA locally can decrease the noise figure with low cooling power since not the whole system has to be cooled. In this chapter, localized LNA cooling using a JT microcooler has been demonstrated. The noise figure of the LNA under study drops by about 0.33 dB from 0.83 to 0.50 dB in the frequency

range between 0.65 and 1.05 GHz with its operating temperature decreasing from 295 to 115 K. Due to the decreasing operating temperature, the gain improvement varies in the range of 0.6 to 1.5 dB, dependent on the frequency. The length of RF lines along the PCB should be further reduced in order to decrease the loss before the LNA and therefore the noise figure.

CHAPTER 7

Long-life micro vacuum packaging

As illustrated in the previous chapters, microcoolers can be used to reach cryogenic temperatures. In order to do so, however, they require a very good thermal insulation from the warm environment. This is established by a vacuum space that has to be maintained at a pressure of 0.01 Pa or lower. A theoretical analysis of a 5-year lifetime micro vacuum chamber for a microcooler is presented in this chapter. The possible sources of gas, evolution mechanisms and their effects on the pressure in the vacuum chamber are discussed theoretically. This study can be used to guide the design of long-lifetime micro vacuum chambers that operate without continuous mechanical pumping. Part of the analysis results are verified by experiments.

7.1 Introduction

Micromachined cryocoolers need vacuum environments to minimize the parasitic loss that is due to the heat flow from the warm environment via the surrounding gas. To serve as an effective stand-alone micro cooling system, the microcooler and the device to be cryocooled need to be integrated in a micro vacuum chamber. As shown in Figure 7.1, the heat load on the microcooler placed in a vacuum chamber includes the conduction of the surrounding gas and the radiation between the microcooler and the vacuum chamber. In the free molecular flow regime, the conductive heat load increases with increasing chamber pressure, given by Eq. 2.19. In the continuum regime, the effect of the chamber pressure on the conductive heat load is negligible. The microcooler is designed to withstand the heat load at the level of radiative heat load. The critical pressure where the conductive heat load is equal to the radiative heat load, is typically about 0.01 Pa. Since both the radiation and conduction are proportional to the surface area of the microcooler, scaling the area has no effect on that critical pressure.

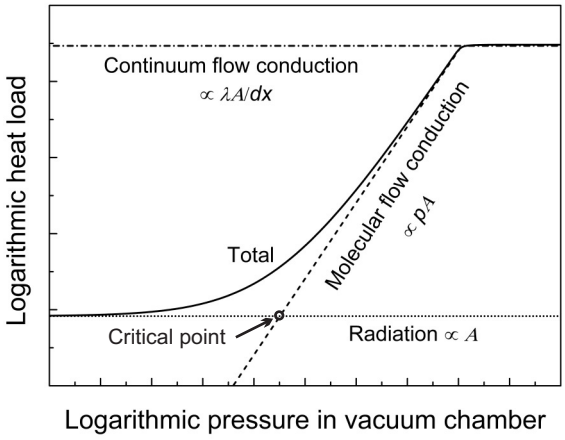

Figure 7.1: Heat load on a microcooler versus pressure in a vacuum chamber.

Why is it difficult to create a vacuum inside a chamber on earth? As Rabelais put it "Nature abhors a vacuum". This concept is as simple as opening a bottle of perfume and as complex as the second law of Thermodynamics [1]. Nature always prefers low energy and maximum entropy. Compared to a macro vacuum chamber, keeping a micro vacuum chamber at a constant vacuum level is more challenging, due to the larger ratio of surface area to volume. Two promising approaches to micro vacuum packaging have been presented, which are a component-level vacuum chamber and a wafer-level vacuum chamber [80]. A variety of fabrication techniques such as anodic bonding [81], solder

[1] http://cosmodemonic.com/index.htm

bonding [82], glass frit bonding [83] and getter techniques [83,84] have been investigated. However, few researchers have paid attention to the testing of the lifetime of the micro vacuum chamber until now. Cheng et al. [82] demonstrated stable, long term testing of vacuum-packaged μ-resonators for 56 weeks at a pressure of 2.5 Pa. Mitchell et al. [85] presented a vacuum packaging approach based on gold-silicon eutectic wafer bonding. The vacuum packages had a total volume of 2.3 x 2.3 x 0.9 mm^3, in which micromachined Pirani vacuum sensors were encapsulated in order to measure the packaged pressures. With the use of getters and a pre-bond outgassing step, pressures can remain stable from about 0.5 to 3.1 Pa with measured pressure fluctuations within $\pm$0.3 Pa for 4 years. This chapter addresses the issue of realizing a micro vacuum chamber to maintain pressure of 0.01 Pa or lower for 5 years.

7.2 Theory

The increase in pressure of a vacuum chamber is due to the gases and vapors released by means of various mechanisms. Such mechanisms involve internal and real leaks, vaporization, desorption, diffusion and permeation [86]. Internal leaks such as gas pockets and real leaks caused by pathways through physical damages should and can be prevented by proper design and careful manufacturing. Vaporization is the gas flux caused by the sublimation of the chamber wall, feedthroughs and other elements inside (microcooler and device to be cooled in our case). In dynamic equilibrium, the rate of molecules leaving the surface of the chamber equals the rate of molecules arriving at the surface. The pressure of the vapor over the surface in dynamic equilibrium is equal to the saturated vapor pressure of the chamber material. The saturated vapor pressures of most vacuum chamber materials (such as metal, glass and ceramic) at ambient temperature are orders of magnitude smaller than the required vacuum pressure of about 0.01 Pa. Therefore, the effect of vaporization is neglected in the design by using these types of materials. The other three causes of pressure increase including desorption, diffusion and permeation for a vacuum chamber placing in the earth's atmospheric environment are specifically considered here.

7.2.1 Desorption

Desorption is the release of adsorbed adsorbates from the surface of the adsorbent. These adsorbates can result from direct adsorption or from the final step in a permeation process. The rate of desorption is a function of the molecular binding energy between the adsorbent and the adsorbate, the surface temperature, and the surface coverage. When the internal surface of a vacuum chamber is exposed to air, the surface will be coated with layers of water molecules. A pump-down process of a vacuum chamber starting from atmospheric pressure goes through two stages. To begin with, the dry air will be mostly pumped away. And after that, the water molecules desorbing from the internal surfaces will follow. Once

the pressure inside is around 0.01 Pa, the desorbing water makes up over 99% of the total gas load [87]. The outer layers of water on the surface are adsorbed physically and the physisorbed water can be removed quickly when the pressure around the surface is lower than 2300 Pa, which is the saturated vapor pressure of water at ambient temperature of 293 K [13]. The innermost layer of water has a chemical binding and is difficult to remove at ambient temperature. Water adsorption and desorption on various material surfaces (including steel, aluminum, copper, glass, Teflon and PVC) were studied by R Dobrozemsky using the tritium-tracer technique [88, 89].

Consider a vacuum chamber of which the wall surface is covered with a monolayer of water molecules. Then, the conservation of mass results in [90]:

$$V\frac{dp}{dt} + Sp + A\frac{dN}{dt}k_BT = 0 \tag{7.1}$$

where V is the inner volume of the chamber (m^3), p the pressure in the chamber (Pa), S the pumping speed ($m^3\ s^{-1}$), A the inner area of the chamber (m^2), N the surface density of water molecules (molecules m^{-2}), and k_B the Boltzmann constant.

The desorption rate of water can be expressed as a first-order reaction:

$$-\frac{dN}{dt} = \frac{N}{\tau_0}\exp\left(-\frac{E}{RT}\right) \tag{7.2}$$

where τ_0 is the nominal period of vibration of the bond between the adsorbed molecule and the substrate which is usually taken to be about 10^{-13} s [91], and E is the activation energy of desorption (J mol^{-1}). Eq. 7.2 shows that pumping will be more effective at a higher temperature.

During a pumpdown, the desorption rate is initially high due to the fact that the outer layers of water on the surface have weaker water to water bonds ($4.2{\cdot}10^4$ J mol^{-1}) [91], and break easily. The innermost layer of water has much higher bond energies and desorbs much more slowly. The activation energy of desorption of the innermost layer of water on stainless steel is in the range of $1.00{\cdot}10^5$-$1.07{\cdot}10^5$ J mol^{-1}, which is dependent on the surface coverage [92]. According to R Dobrozemsky's experimental data [88, 89], the virtual energy of desorption of water on glass is also in this range.

When pumping is stopped then Eq. 7.1 shows that the increase in pressure is given by:

$$\frac{dp}{dt} = -\frac{dN}{dt}\frac{A}{V}k_BT \tag{7.3}$$

This equation shows that a smaller volume will cause a faster pressure increase for a given surface area. This means that it is more difficult for a chamber with a larger surface to volume ratio to maintain a constant pressure level.

If pumping is stopped at pressure p_0 and only the innermost layer of water is left on the surface with molecule density N_0 of 10^{19} molecules m^{-2}, then Eq. 7.3 can be used to derive the relation between pressure and molecule density after pumping has been stopped

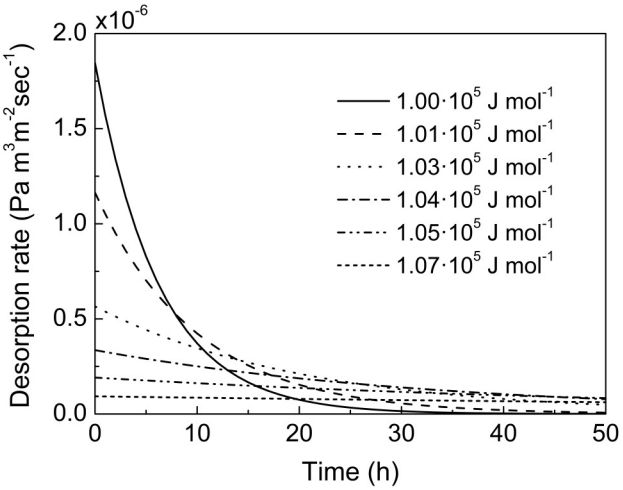

Figure 7.2: Desorption rate of water molecules as a function of time with different activation energies with initial molecular surface density of 10^{19} molecules m^{-2} at ambient temperature.

as:

$$(p - p_0) = \left(\frac{Ak_BT}{V}\right)(N_0 - N) \tag{7.4}$$

Based on Eq. 7.2, the surface density of water molecules with an initial value, N_0, after a certain time, t, becomes:

$$N = N_0 \exp\left(-\alpha\frac{t}{\tau_0}\right), \text{where } \alpha = \exp\left(-\frac{E}{RT}\right) \tag{7.5}$$

By combining Eqs. 7.2 and 7.5, the desorption rates of the innermost layer of water with molecular surface density, N_0, can be obtained. Figure 7.2 shows the desorption rates of water with various activation energies of desorption. As can be expected, the desorption rate of water with lower activation energy changes faster than that of water with higher activation energy.

As N decreases in time, p increases. Assume we stop pumping at a very low pressure (i.e. p_0 = 0) and furthermore that after pumping is stopped all remaining molecules at molecule density N_0 desorb and thus build up pressure. Then, the resulting pressure in the chamber is:

$$p = \frac{Ak_BT}{V}N_0 \tag{7.6}$$

Consider a microcooler vacuum chamber with inner volume V of $3.6{\cdot}10^{-5}$ m^3, inner area A of $8.1{\cdot}10^{-3}$ m^2 and resulting surface area-to-volume ratio of 225 m^{-1} . We find p = 9 Pa at ambient temperature, as indicated in Figure 7.3 that shows the pressure increase in the chamber after pumping is stopped as a function of time with different activation energies.

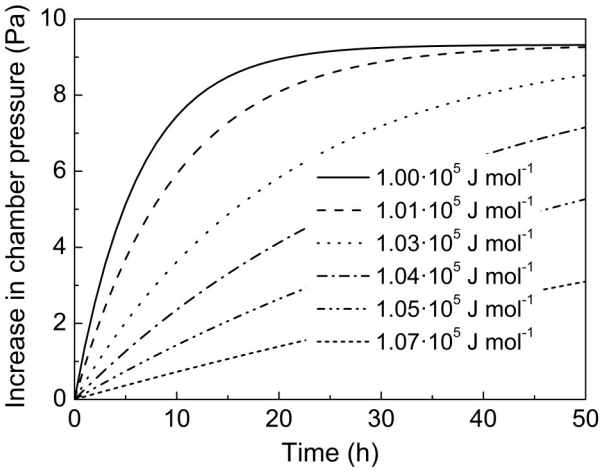

Figure 7.3: Increase in chamber pressure due to desorption after pumping is stopped as a function of time at various activation energies. Chamber volume $3.6{\cdot}10^{-5}$ m^3, inner area $8.1{\cdot}10^{-3}$ m^2 and initial molecular surface density 10^{19} molecules m^{-2} at ambient temperature.

If we want a vacuum space to remain at a pressure below a maximum p^*, then Eq. 7.6 shows that we need to reduce the molecule density to N^*:

$$N^* = \frac{p^* V}{A k_B T} \tag{7.7}$$

Eq. 7.5 shows that the pumping time required to arrive at this molecule density is given by:

$$t^* = \frac{\tau_0}{\alpha} \ln \frac{N_0}{N^*} \tag{7.8}$$

Since $\alpha = \exp\left(-\frac{E}{RT}\right)$ it again is clear that pumping at an elevated temperature is beneficial.

Figure 7.4 shows the relationship between the bake-out time and the baking temperature at various activation energies. As shown in the figure, it is hard to remove the chemisorbed water at ambient temperature, but water molecules are easily desorbed by baking at about 100 °C.

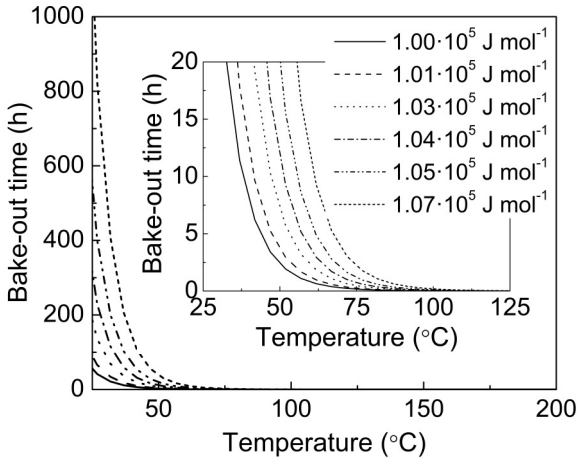

Figure 7.4: Bake-out time determined by desorption process as a function of baking temperature with different activation energies. Chamber volume $3.6{\cdot}10^{-5}$ m^3, inner area $8.1{\cdot}10^{-3}$ m^2 and initial molecular surface density 10^{19} molecules m^{-2}.

7.2.2 Permeation

Permeation is a three-stage process, consisting of the adsorption of gases at the exterior surface of the wall, the diffusion through the wall, and the desorption at the interior surface. In general, the diffusion through the wall determines the dynamics and the problem is described by the diffusion equation. For a stainless steel chamber, hydrogen gas is the most relevant diffusing gas, accounting for 90% or more of the permeation [93]. Helium gas permeation is dominant in case of a glass vacuum chamber [94]. The permeation of hydrogen gas in a stainless steel chamber and helium gas in a glass chamber are analyzed below.

It is assumed that the chamber wall has been completely degassed, which means that the gas concentration c inside the chamber wall is initially zero. This can only be realized if the micro vacuum chamber as a whole is placed in a larger vacuum oven. At time t =0, the micro vacuum chamber is closed, it is taken out of the vacuum oven, and the outer surface is exposed to air. Then, this exposure produces a concentration c_1 at this surface and the inner surface is maintained under vacuum.

According to Sieverts' law the concentration on the outer surface is given by [94]:

$$c_1 = \frac{K}{D} p_1^n \tag{7.9}$$

where D is the diffusivity, K is the permeability, and p_1 is the partial pressure of the gas under consideration. The partial pressures of hydrogen and helium gas in normal air are 0.055 and 0.52 Pa, respectively. In the case of permeation of hydrogen gas through metals,

n = 0.5, due to the dissociation of the hydrogen molecule. For the permeation of helium gas through dielectrics, n =1 [94].

It has been well established that the diffusivity and permeability of hydrogen gas in metals are given by Arrhenius-type equations:

$$D = D_0 \exp(-E_d/RT) \tag{7.10}$$

$$K = K_0 \exp(-E_k/RT) \tag{7.11}$$

For diffusivity, the values of the constant D_0 and the thermal activation energy of hydrogen gas in 304 type steel are $4.7{\cdot}10^{-7}$ m^2 s^{-1} and $5.4{\cdot}10^4$ J mol^{-1}, respectively; For permeability, the values of the constant K_0 and the thermal activation energy of hydrogen gas in 304 type steel are $1.9{\cdot}10^{-4}$ Pa$^{0.5}$ m^2 s^{-1} and $6.0{\cdot}10^4$ J mol^{-1}, respectively as reported by Louthan and Derrick [95].

Perkins [94] proposed formulae that fit the diffusivity and permeability data for helium gas in glass (vitreous silica) as:

$$D = D_T T \exp(-E_d/RT) \tag{7.12}$$

$$K = K_T T \exp(-E_k/RT) \tag{7.13}$$

where D_T is $3.0{\cdot}10^{-11}$ m^2 K^{-1} s^{-1}, E_d is $2.0{\cdot}10^4$ J mol^{-1}, K_T is $2.1{\cdot}10^{-13}$ m^2 K^{-1} s^{-1} and E_k is $1.8{\cdot}10^4$ J mol^{-1}.

The one-dimensional diffusion equation is:

$$D\frac{\partial^2 c}{\partial^2 x} = \frac{\partial c}{\partial t} \tag{7.14}$$

The initial and boundary conditions are:

$c = 0$	for	$0 \le x \le d$	at	$t = 0$
$c = 0$	for	$x = 0$	at	$t > 0$
$c = c_1$	for	$x = d$	at	$t > 0$

The solution to the diffusion equation is:

$$c(x,t) = \frac{xc_1}{d} + \frac{2c_1}{\pi}\sum_{n=1}^{\infty}\frac{(-1)^n}{n}\sin\left(\frac{n\pi x}{d}\right)\exp\left(-\left(\frac{n\pi}{d}\right)^2 Dt\right) \tag{7.15}$$

The instantaneous permeation rate (Pa m^3 m^{-2} s^{-1}) at the interior surface at time t is:

$$\dot{Q}(t) = D\left(\frac{\partial c}{\partial x}\right)_{x=0} = \frac{Dc_1}{d} + \frac{2Dc_1}{d}\sum_{n=1}^{\infty}(-1)^n\exp\left(-\left(\frac{n\pi}{d}\right)^2 Dt\right) \tag{7.16}$$

When t is equal to t_c, the equilibrium permeation rate is:

$$\dot{Q}(\infty) = \frac{Dc_1}{d} \tag{7.17}$$

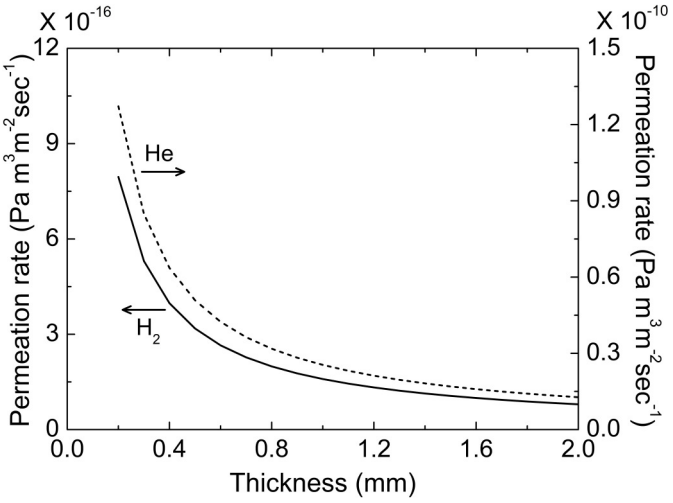

Figure 7.5: Permeation rate as a function of wall thickness of stainless steel and glass vacuum chamber for hydrogen and helium gas at ambient temperature, respectively, with corresponding partial pressures of 0.055 and 0.52 Pa.

The time to reach this steady state, can be approximated by t_c which is known as the critical time and is given by [96]:

$$t_c = \frac{d^2}{6D} \tag{7.18}$$

For the permeation of helium gas through a 2 mm thick glass chamber, the critical time is only about 2 days. Thus, in practice the permeation rate of helium gas through a glass chamber can be considered to be at equilibrium rate.

For the permeation of hydrogen gas through a 2 mm thick stainless steel chamber, the critical time is more than 100 years. At shorter time intervals, the permeation rate of hydrogen can be approximated. Reference [93] shows that in the case $Dtd^{-2} \leq 0.02$, the permeation rate obeys:

$$\dot{Q}(t) < 10^{-4}\dot{Q}(\infty) \tag{7.19}$$

The condition $Dtd^{-2} \leq 0.02$ for a 2 mm wall thickness corresponds to a maximum time of about 13 years. Therefore, within the time span of 5 years, the permeation rate of hydrogen gas through the stainless steel chamber wall can be considered as 0.01% of the equilibrium permeation rate.

Figure 7.5 shows the relationship between the permeation rate at the inner surface and the wall thickness of the vacuum chamber in 5 years. Here, the permeation rate of helium gas through a glass chamber is at its equilibrium rate, given by Eq. 7.17. The permeation rate of hydrogen gas through a stainless steel chamber is 10^{-4} of its equilibrium rate. As shown in Figure 7.5, the permeation rate of hydrogen gas through a stainless steel

chamber wall is about five orders of magnitude lower than that of helium gas through a glass chamber (for the same wall thickness).

As can be imagined, the pressure that is built up in time inside the vacuum chamber due to the permeation of gas, will show a similar dependence on the wall thickness as shown in Figure 7.5. The pressure built up after a period of five years in the stainless steel vacuum chamber introduced in section 7.2.1 (i.e. chamber volume $3.6{\cdot}10^{-5}$ m^3, inner area $8.1{\cdot}10^{-3}$ m^2) due to the permeation of hydrogen gas, is shown in Figure 7.6. In Figure 7.6, the permeation rate is based on Eqs. 7.17 and 7.19. The resulting pressure built up is much lower than the microcoolers' acceptable vacuum pressure. In contrast, the pressure built up in a glass vacuum chamber due to helium gas permeation quite quickly reaches this acceptable level. Figure 7.5 shows that at a thickness of about 2 mm, the helium gas permeation rate is around $1.5{\cdot}10^{-11}$ Pa m^3 m^{-2} s^{-1}. With the above mentioned values for area and volume a pressure of 0.01 Pa results in about one month! The permeation of helium gas through glass can be limited by coating it with titanium [97]. Besides functioning as a permeation barrier, titanium also absorbs other residual gases such as water and oxygen.

Glass and ceramics are widely used for optical and electrical feedthroughs. It is extremely important that these feedthroughs have a low helium-gas permeation rate in order to establish a long lifetime micro vacuum chamber. A commercial electrical feedthrough [98] with a leak rate lower than 10^{-11} Pa m^3 s^{-1}. The leak rate was measured in an environment with a helium gas pressure of 10^5 Pa. Therefore, the helium gas leak rate in normal air with a helium gas partial pressure of 0.52 Pa should be less than $5.2{\cdot}10^{-17}$ Pa m^3 s^{-1}. For the chamber discussed above with an internal volume of $3.6{\cdot}10^{-5}$ m^3, pressure level of 0.01 Pa and lifetime of 5 years, the pressure increase rate should be less than $2.3{\cdot}10^{-15}$ Pa m^3 s^{-1}. Thus, the helium leak rate of feedthroughs for the discussed chamber is acceptable. Perkins [94] pointed out that the permeability of CGW 1720 (Pyrex) glass is of the same order of magnitude as that of the 97% alumina ceramic (no data were reported as to the over-all composition) when the application temperature is less than 200 °C. Compared to Corning 9606 pyroceram (a glass ceramic) and mullite ceramic in the temperature range less than 200 °C, the permeability of CGW 1720 glass and the 97% alumina ceramic is much lower. Thus, the application of the latter two materials as insulators of feedthroughs is attractive in vacuum-chamber applications.

As can be seen in Figure 7.6, the pressure built up in this stainless steel chamber due to hydrogen permeation at a wall thickness of 2 mm is about $2.8{\cdot}10^{-6}$ Pa in a period of 5 years. Obviously, the pressure built up scales linearly with the area-to-volume ratio, as is also shown in Figure 7.7.

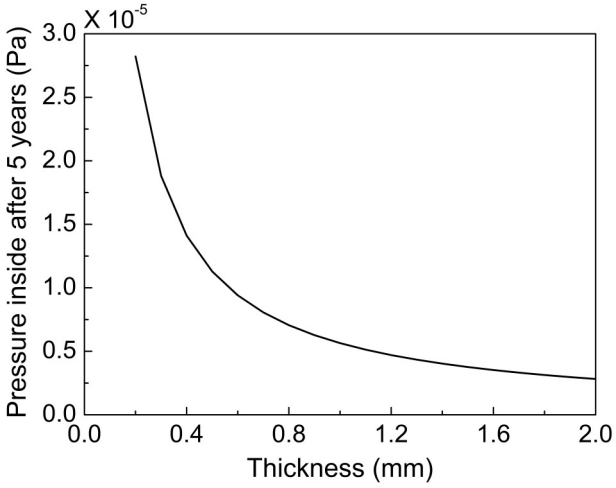

Figure 7.6: Maximum pressure built up in stainless steel vacuum chamber after 5 years (chamber volume $3.6{\cdot}10^{-5}$ m^3, inner area $8.1{\cdot}10^{-3}$ m^2) due to permeation of hydrogen gas at ambient temperature as a function of the wall thickness of the vacuum chamber (based on Eqs. 7.17 and 7.19).

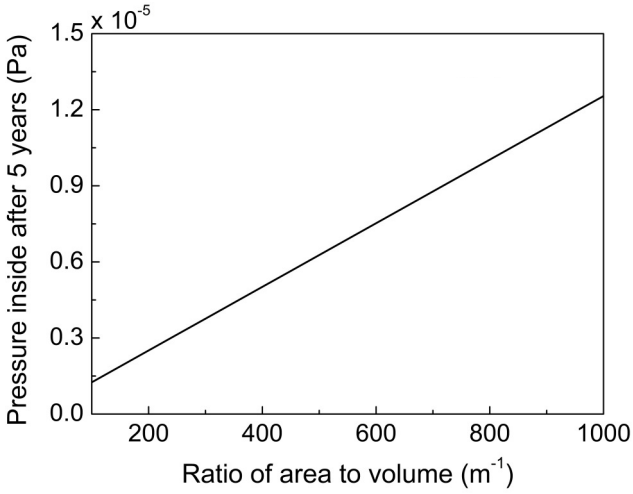

Figure 7.7: Pressure built up in a stainless steel vacuum chamber after 5 years due to hydrogen permeation at ambient temperature, as a function of the surface area-to-volume ratio of the vacuum chamber (wall thickness 2 mm and chamber volume $3.6{\cdot}10^{-5}$ m^3).

7.2.3 Diffusion

The outgassing in a vacuum chamber due to permeation is caused by the gases from the outside of the vacuum chamber. Except for the outside gases, the gases from the walls of the vacuum chamber also contribute to the system outgassing through diffusion. For a material of unit cross-sectional area and thickness d, the initial and boundary conditions in the diffusion process are:

$c = c_1$	for	$0 \leq x \leq d$	at	$t = 0$
$c = 0$	for	$x = 0$	at	$t > 0$
$c = 0$	for	$x = d$	at	$t > 0$

The solution is:

$$c(x,t) = \frac{4c_1}{\pi} \sum_{n=0}^{\infty} (2n+1)^{-1} \sin \frac{\pi(2n+1)x}{d} \exp\left(-\left(\frac{\pi(2n+1)}{d}\right)^2 Dt\right) \tag{7.20}$$

The instantaneous outgassing rate at one surface of the slab is:

$$\dot{Q}(t) = D\left(\frac{\partial c}{\partial x}\right)_{x=0} = \frac{4c_1 D}{d} \sum_{n=0}^{\infty} \exp\left(-\left(\frac{\pi(2n+1)}{d}\right)^2 Dt\right) \tag{7.21}$$

At relatively large values of the time t the contributions of the subsequent terms in the series of Eq. 7.21 very rapidly decrease. If $Dt/d^2 > 0.029$ then the second term is 10% of the first and the third is only 1% of the second. Therefore, if $Dt/d^2 > 0.029$ we can approximate the outgassing rate as:

$$\dot{Q}(t) = \frac{4c_1 D}{d} \exp\left(-\left(\frac{\pi}{d}\right)^2 Dt\right) \tag{7.22}$$

To reduce the outgassing rate through diffusion in a vacuum chamber, a baking process can be adopted before the vacuum chamber is sealed. The objective of the bake-out process is to degass the wall of the vacuum chamber and all materials inside the chamber. The bake-out time of hydrogen in a stainless steel chamber and helium in a glass vacuum chamber can be approximated using the Eq. 7.22. Assume that when the baking and pumping is stopped, the outgassing continues at a constant rate as expressed by Eq. 7.22, then the pressure built up in a certain time interval can be evaluated by multiplying the time elapsed with the outgassing rate and area/volume. In other words, the acceptable outgassing rate is determined by required pressure, lifetime and the surface area-to-volume ratio of the vacuum chamber. For the chamber discussed above with an internal volume of $3.6{\cdot}10^{-5}$ m^3, inner area $8.1{\cdot}10^{-3}$ m^2, pressure level of 0.01 Pa and lifetime of 5 years, the acceptable outgassing rate is $2.8{\cdot}10^{-13}$ Pa m^3 m^{-2} s^{-1}. The diffusivity is a function of the thermal activation energy of the diffusing gas in the solid as expressed in Eqs. 7.10 and 7.12. Because of the exponential dependence on temperature, an increase

in temperature will sharply increase the diffusivity and reduce the required bake-out time. With the given acceptable outgassing rate of $2.8{\cdot}10^{-13}$ Pa m^3 m^{-2} s^{-1}, the bake-out time of hydrogen in a stainless steel chamber and helium in a glass vacuum chamber for an interval of 5 years and a pressure built up of 0.01 Pa are depicted in Figure 7.8. The initial hydrogen concentration in stainless steel and helium concentration in glass are related to their partial pressures in air by means of Sieverts' law [94], $c_1(H_2) = 8.55$ Pa m^3 m^{-3} and $c_1(\mathrm{He}) = 8.1{\cdot}10^{-3}$ Pa m^3 m^{-3}. Due the stainless steel and glass production procedure, the amounts of hydrogen and helium dissolved in the two types of materials, respectively, can be higher than the value evaluated based on Sieverts' law. However, the initial concentration value does not influence the baking time a lot because the baking time is mainly determined by the diffusivities at different temperatures as indicated by Eq. 7.22.

As shown in Figure 7.8, the bake-out time decreases rapidly with increasing bake-out temperature. Furthermore, the bake-out time can be decreased significantly by reducing the wall thickness and at a reduction from 2.0 to 0.5 mm the resulting increase in permeation rate of hydrogen is acceptable as shown in Figures 7.5 and 7.6. Compared to the bake-out time required for stainless steel, the bake-out time required for glass is much shorter, which means that the diffusion resistance of helium through glass is smaller. The smaller diffusion resistance also implies that the outgassing due to permeation of helium through glass is an issue as discussed in section 7.2.2, and a permeation barrier, such as a titanium film is needed.

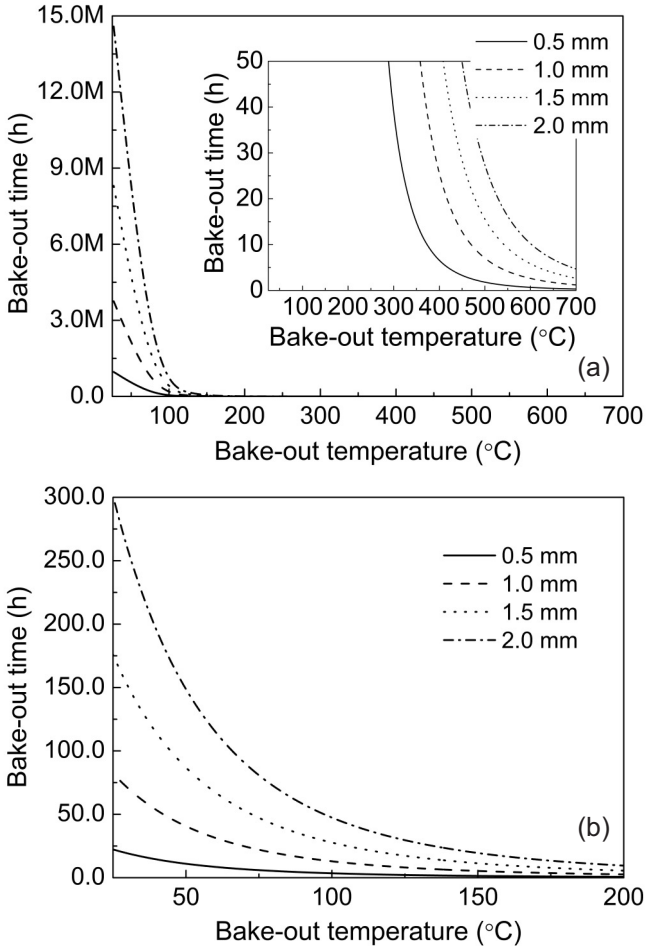

Figure 7.8: Bake-out time required for stainless steel (a) and glass vacuum (b) chamber (chamber volume $3.6{\cdot}10^{-5}$ m^3 and inner area $8.1{\cdot}10^{-3}$ m^2) as a function of bake-out temperature, based on acceptable pressure built up due to remaining hydrogen or helium outgassing of 0.01 Pa in 5 years. The initial hydrogen and helium concentration are 8.55 and $8.1{\cdot}10^{-3}$ Pa m^3 m^{-3}, respectively.

7.3 Getter pumps

As shown above, the bake-out time can be strongly reduced by increasing the bake-out temperature. However, electronic devices inside the vacuum chamber and other components may limit the maximum bake-out temperature which may result in insufficient baking. Getter pumps [99] are commonly used in these vacuum chambers to provide a continuous pumping mechanism after the chambers are sealed. Getter pumps include evaporable getters [100] and non-evaporable getters [101]. Evaporable getters employ

volatile and reactive materials such as barium and titanium [102], which are heated, evaporate and deposit on adjacent surfaces. These deposited materials capture gases on their surface in the form of stable chemical compounds. The pumping speed of an evaporable getter depends on the sticking coefficient of the gas on the surface. The sticking coefficient is higher at lower temperatures. In contrast, non-evaporable getters adsorb gases at the surface, followed by gases diffusion into the getter material. As indicated by name, the materials used in non-evaporable getters remain in the solid state instead of being evaporated and deposited on a surface. The pumping speed of a non-evaporable getter is limited by the diffusion process [103]. Since an increase in temperature represents an increase in the average molecular speed, the diffusion rate increases with increasing temperature. The getter pumps used in the experiment described in the next section are non-evaporable getters that employ porous, sintered, zirconium alloy [104, 105]. The getter can sorb hydrogen, carbon monoxide, carbon dioxide, oxygen, nitrogen, and water vapor at room temperature. Hydrocarbons are sorbed only at temperatures around 300 °C. Noble gases cannot be sorbed by this kind of getter. To capture noble gases or hydrocarbons at room temperature, the getter must be used in combination with a second pump, most commonly a sputter-ion pump [106].

7.4 Experimental results and discussion

The effect of baking and getter activation was investigated with a micro stainless steel vacuum chamber (shown in Figure 7.9). The cleaning procedures for the vacuum chambers included: remove all debris by blowing out with a high-pressure nitrogen line, wash in a hot water (approximate 80 °C) jet, dry using a clean high-pressure nitrogen flow, clean using acetone in an ultrasonic bath for at least 30 min, dry using clean high pressure nitrogen flow, clean using isopropanol in an ultrasonic bath for at least 30 min, finally, dry using clean high-pressure nitrogen flow. The inner volume and area are $3.6{\cdot}10^{-5}$ m^3 and $8.1{\cdot}10^{-3}$ m^2 respectively. An electrical feedthrough with 10 pins was used in the measurements [98]. The pin header feedthrough is an alumina ceramic feedthrough with a helium gas leak rate less than $5.2{\cdot}10^{-17}$ Pa m^3 s^{-1} in normal air. To minimize outgassing rates, a small manometer with little material and a low outgassing rate is necessary. A micropirani sensor kit calibrated for nitrogen at 25 °C was chosen [107]. In addition, a ST172 non-evaporable getter of SAES Getter was integrated in the chamber [108].

A total of four micro vacuum chambers was prepared. Table 7.1 presents an overview of the baking process of these chambers as well as the getter activation temperature.

After the cleaning and baking steps, the copper pinch-off tubes of the vacuum chambers are pinched off and from that moment the pressures inside the chambers were recorded. Because the fourth chamber was not baked at a higher temperature but only at a lower temperature, the measurement started 7 days earlier than for the other chambers, as shown in Figure 7.10. Compared to the other three chambers, only the

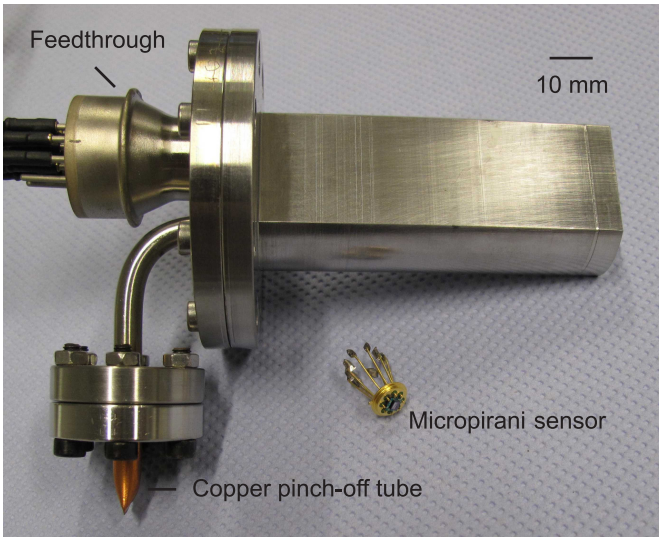

Figure 7.9: Photograph of the micro vacuum chamber.

third assembled chamber was not baked at 100 °C. Figure 7.10 shows the pressure in the third chamber gradually increases to about 0.15 Pa in the first 60 days because the desorption rate of water molecules of the third chamber is higher than the gettering rate. This indicates that baking the assembled chamber at 100 °C is necessary because the water layer forms again after a short time once the baked stainless steel chamber is exposed to atmospheric air [109, 110]. The pressure in the third chamber decreases after 60 days

Table 7.1: Overview of the set of measurements.

Chamber	Cleaning	Baking chamber 550 °C[a]	Baking total 100 °C[b]	Pump during activation	Getter activation temperature (°C)
1	X	X	X	X	900 (5 min)
2	X	X	X	X	450 (30 min)
3	X	X		X	450 (30 min)
4	X		X	X	450 (30 min)

[a] The baked chamber (without feedthrough, copper pinch-off tube, getter and pressure sensor) is in a vacuum oven at a pressure 1 Pa. The temperature inside ramps up to 550 °C from ambient temperature at 25 °C h^{-1} and remains stable at 550 °C for 56 h, then cools down to ambient temperature at 17.5 °C h^{-1}. After baking, the chamber is exposed to air for half an hour before assembling with flange cover.

[b] The assembled vacuum chamber is baked at 100 °C for 22 h connected with a turbo molecular pump at a pressure of less than 10^{-4} Pa.

because apparently the desorption rate of water drops below the gettering rate. The difference between the second and fourth chambers is that the fourth chamber was not baked at 550 °C but only at 100 °C, and the pressure inside the fourth chamber is a little higher as shown in Figure 7.10. According to the analysis above, a temperature of 100 °C is sufficient for removing the water layer but not the hydrogen gas inside the wall. Besides, the second chamber was baked in a vacuum oven at a pressure of 1 Pa, which is not low enough to reach an acceptable outgassing rate of $2.8{\cdot}10^{-13}$ Pa m^3 m^{-2} s^{-1} for the chamber under test without a getter. However, the gettering rate of hydrogen gas is much higher than the hydrogen outgassing rate. Thus, the pressure difference between the fourth chamber and the second chamber can be due to an inaccuracy of the pressure sensor mainly caused by zeroing procedure at different temperatures. No difference was observed between activation of the getter at 450 °C for 30 minutes and 900 °C for 5 minutes (chambers 1 and 2). The pressures in chambers 1 or 2, and 4 increase from the zero setpoint to about 0.05 and 0.07 Pa, respectively in few hours as indicated in Figure 7.10. We think that is because the zero procedures start at relatively high temperature, and the pressure of reading increases as the temperature reduces to ambient temperature. Therefore, we expect the real pressures in chambers 1, 2 and 4 are lower than the values of reading.

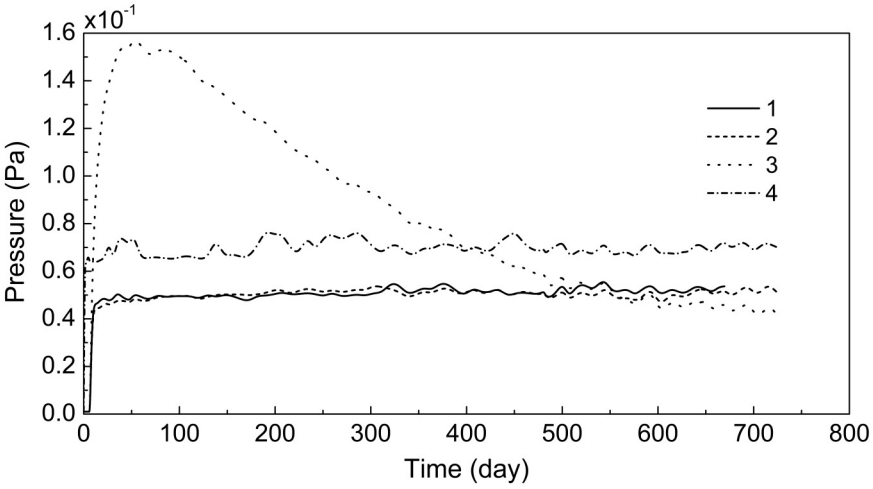

Figure 7.10: Pressures in stainless steel vacuum chambers versus time. The pressure of the first chamber was not recorded after 670 days because the pressure sensor broke.

7.5 Conclusions

In this chapter, the possible sources of gas, evolution mechanisms and their corresponding effects on the vacuum chamber have been discussed theoretically. It is difficult to remove the monolayer chemisorbed water on the stainless steel or glass chamber surface at ambient temperature, but it is easily desorbed by baking at temperature above 100 °C for an hour. For stainless steel chambers, hydrogen gas is the main gas accounting for 90% or more during the permeation process. However, the pressure increase due to the hydrogen gas permeation is much lower than the required pressure (0.01 Pa). Helium gas permeation presents a major problem for glass chambers. The pressure in glass vacuum chambers due to helium gas permeation is eventually equal to the partial helium gas pressure in the air (0.52 Pa), which is higher than the microcoolers' acceptable vacuum pressure. A helium gas permeation barrier such as a titanium coating is essential. Outgassing through diffusion can be reduced via a baking process. The use of glass or ceramic as an insulator of the feedthrough is very common in a vacuum chamber. Therefore, it is particularly important to select an insulator material that has low permeability, and to implement post-processing such as increasing the permeation barrier because a non-evaporable getter cannot sorb helium gas. Without considering the internal and real leaks, it is possible to maintain a vacuum chamber with chamber volume $3.6{\cdot}10^{-5}$ m^3 and inner area $8.1{\cdot}10^{-3}$ m^2 at a pressure of 0.01 Pa for 5 years without a getter. However, this conclusion needs to be supported by further experimental evidence. If the materials used in the chamber outgas easily (such as epoxy) or the chamber cannot be baked at sufficiently high temperature (e.g. for prevent damaging of internal sensors), a getter will be needed to compensate for the extra outgassing.

CHAPTER 8

Improvement in CFHX performance

Counter flow heat exchangers (CFHXs) are essential elements for Joule-Thomson (JT) microcoolers. The performance of CFHXs has a crucial influence on the overall behavior of microcoolers. In this chapter, the thermal and hydraulic performance of the high- and low-pressure channels of CFHXs with pillar matrices are investigated numerically for different flow patterns.

8.1 Introduction

In our design, the CFHX of the microcooler is composed of glass wafers with chemically etched channels [49, 78, 111]. A nitrogen-operated microcooler aiming at a temperature of around 100 K requires a high-pressure of about 8.0 MPa to achieve reasonable cooling. Because of the high pressure in the channels of the CFHX and the thin channel walls, high mechanical stresses inside the CFHX can be a problem. To keep the stress within limits, the high and the low-pressure channels contain pillar matrices. The pillars in the channels are conical frustums because of the isotropic chemical etching manufacturing process. The effect of the pillars on thermal and hydraulic characteristics of the CFHX is important for the microcooler design.

There has been extensive research on the heat transfer and pressure drop of flow across channels containing pillars with various pillar cross-sections, such as circular [112, 113], rectangular [114], elliptical [115], diamond [116] and square [117] shapes, etc. It is well known that the streamline-shaped cross section has less flow resistance. However, it is not clear which type of pillar has the best heat transfer performance. Also, a high heat transfer usually implies a high fluidic impedance and thus heat transfer and flow resistance should both be considered in the design. D. Poulikakos and A. Bejan [118] found a theoretical method to determine the optimal pillar geometry and dimensions in terms of the minimization of entropy generation in forced convection. The method of the minimization of entropy generation was adopted by W.A. Khan et al. [119] to analyze the thermodynamic losses caused by heat transfer and pressure drop in heat sinks with cylindrical pillars. By using this method, all relevant design parameters for heat sinks, including geometric parameters, material properties and flow conditions can be simultaneously optimized. W.A. Khan et al. [120] compared the overall performance of heat sinks with different pillar geometries comprising rectangular, square, circular and elliptical pillars. The results indicated that the preferred pillar profile was dependent on the parameters including axis ratio, aspect ratio and Reynolds number. K. Park et al. [121] numerically investigated the design optimization of heat sinks with square pillars. The thermal and hydraulic characteristics of heat sinks were analyzed using the finite volume method and a local optimization technique was used to obtain the optimum design.

In this chapter, the thermal and hydraulic characteristics of rectangular channels filled with staggered and aligned pillar matrices are simulated using Ansys Fluent [122], and the correlations of the Nusselt number and the Darcy-Weisbach friction factor in the channels are obtained through numerical data. These correlations can be used for predicting the performance of a microcooler. It is found that the microcooler performance can be improved by replacing the aligned pillar array in the high-pressure channel with staggered pillar array.

8.2 Analysis

The overall thermal performance of a CFHX is determined by the total thermal resistance from one fluid to the other, which includes two convective resistances at the wall-fluid interfaces and the conductive thermal resistance through the separating wall. The total thermal resistance per unit area can be expressed by:

$$1/U = 1/h_h + \delta_w/\lambda_w + 1/h_c \tag{8.1}$$

where $1/U$, $1/h_h$, δ_w/λ_w, $1/h_c$ are the total thermal resistance per unit area, convective resistance per unit area at the solid-hot fluid interface, the conductive thermal resistance in channel wall and convective resistance per unit area at the solid-cold fluid interface. The conductive term can be evaluated based on the thickness δ_w and the thermal conductance λ_w. The convective heat transfer is usually characterized by the Nusselt number. For fully developed laminar flow in rectangular channels, the Nusselt number depends on the cross sectional shape of the channel and the boundary conditions [38]. The heat transfer coefficients (h_h, h_c) can be obtained from the Nusselt number, the hydraulic diameter of the channel and the thermal conductivity of the fluid as given in Eq. 2.7. The CFHXs of our microcoolers have high and low-pressure channels with the same rectangular cross section. The Nusselt number of fully developed laminar flow in a rectangular channel with uniform wall temperature is determined by the aspect ratio of height-to-width (α), which can be approximated by the following empirical equation [38]:

$$Nu = 7.541\left(1 - 2.610\alpha + 4.970\alpha^2 - 5.119\alpha^3 + 2.702\alpha^4 - 0.548\alpha^5\right) \tag{8.2}$$

Without considering the effect of the pillars in the high- and low- pressure channels, the thermal resistance per unit area of a CFHX can be evaluated by using Eqs. 8.1 and 8.2. Figure 8.1 shows the thermal resistance per unit area of a CFHX. The channel width, the channel height and intermediate wall thickness of the CFHX are 10 mm, 40 μm and 105 μm, respectively. The working fluids of high and low-pressure channels are nitrogen gas at 8.0 and 0.60 MPa. The convective thermal resistance from low-pressure gas to middle wall is larger than that from middle wall to high-pressure gas because of the difference in the gas thermal conductivity. Compared with the total convective thermal resistance, the conductive thermal resistance of the middle wall is smaller, which means that the thermal performance of the CFHX can be improved by decreasing the total convective thermal resistance.

The microcooler requires a high pressure to establish enough cooling power for cooling down. To withstand the high pressure pillar matrices are made in the high-pressure channel as well as in the low-pressure channel for controlling the stresses inside within limits. The pillar configurations of the high and low-pressure channels with

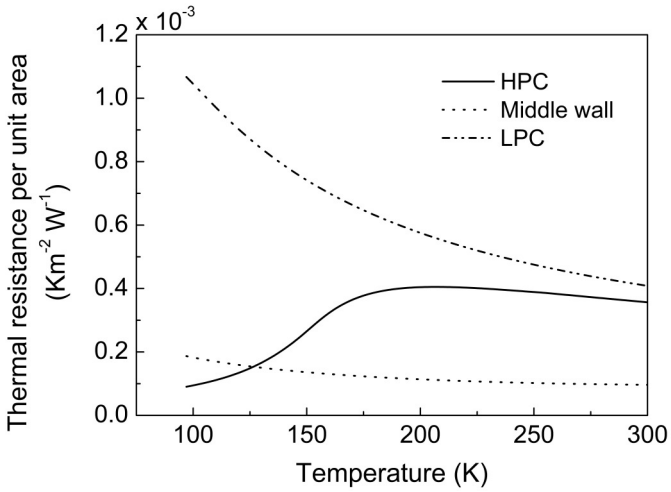

Figure 8.1: Thermal resistance per unit area of a CFHX with fully developed laminar flow in rectangular channels as a function of temperature. CFHX geometry: channel width 10 mm, channel height 40 μm and intermediate wall thickness 105 μm. Working fluid: nitrogen gas at 8.0 and 0.60 MPa. (HPC: high pressure channel; LPC: low pressure channel).

a height of 40 μm are depicted as shown in Figure 8.2. The thermal and hydraulic characteristics of the channels are not only determined by the pillar configurations, but also influenced by the flow direction. The high-pressure channel has an aligned pillar array for the horizontal direction and a staggered array arrangement in the vertical direction. The low-pressure channel has two different aligned array arrangements along horizontal and vertical directions.

To simulate the hydraulic and thermal characteristics of channels with pillars, the Knudsen number is indispensable for determining whether statistical mechanics or the continuum mechanics formulation of fluid dynamics should be used. For the microcooler, the Kundsen number is around 10^{-3} in channels of the CFHX, which indicates that the continuum mechanics can be used in the modeling of the thermal and hydraulic behaviors of channels with pillars. The governing equations used in this modeling are the continuity, the incompressible Navier-Stokes, and the energy equations. These equations together with boundary conditions are then implemented by a finite volume method through Ansys Fluent [122].

A three dimensional model of a rectangular channel with pillars is developed for analyzing the characteristics of the CFHX channels. Figure 8.3 shows the physical model of the high-pressure channel with staggered pillar arrangement. Corresponding to the physical model, two assumptions are predefined: the flow is steady and laminar and the fluid properties are constant. The properties of nitrogen gas are used: at 8.0 MPa for the high-pressure channel and at 0.60 MPa for the low-pressure channel.

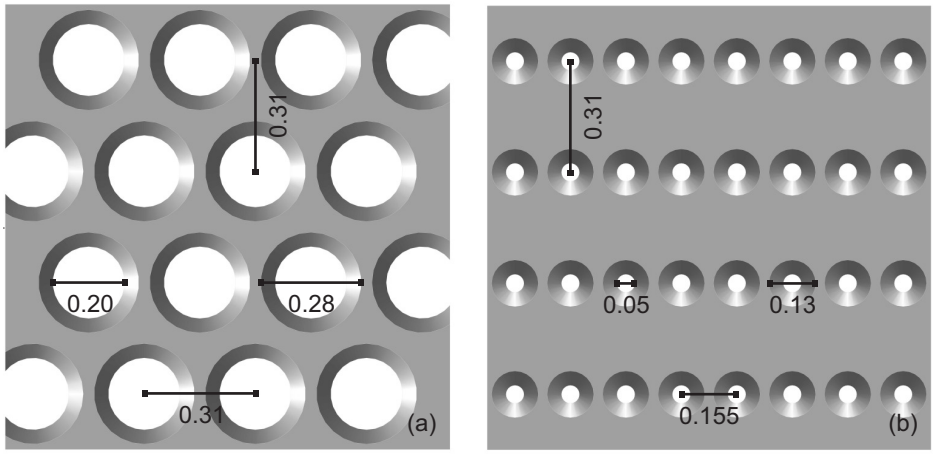

Figure 8.2: Pillar geometry in high-pressure channel (a) and low-pressure channel (b) (dimensions in mm).

The convective heat transfer characteristics closely depend on the thermal boundary conditions. Here, two thermal boundary conditions are considered: isothermal top wall

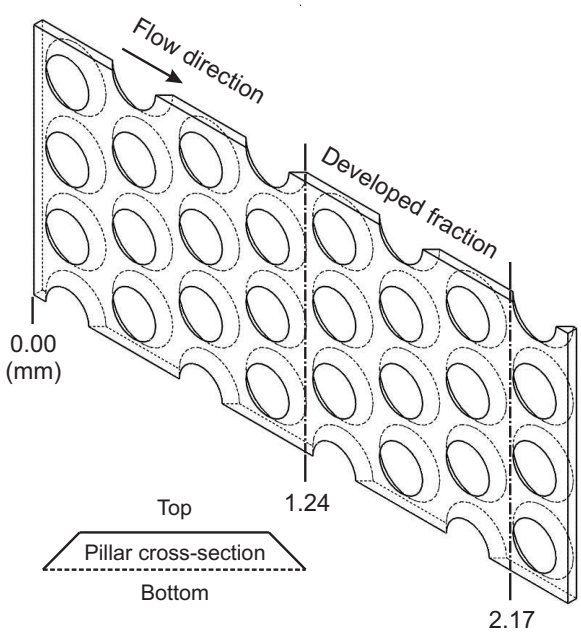

Figure 8.3: Geometry of the high-pressure channel with staggered pillar arrangement.

and isothermal bottom wall. In the former case (isothermal top wall) the surface of the top wall and that of the pillars are set at a fixed temperature whereas the bottom wall and the two side walls of the channel are considered to be adiabatic. In the latter case (isothermal bottom wall) the bottom wall is isothermal and the top wall is adiabatic. The other conditions remain the same. The temperature boundary values obviously affect the thermal and hydraulic behavior but these values are not relevant for the analyzing method itself. Gas inlet temperatures are considered of 300 and 97 K, whereas the isothermal wall is considered to be at 5 K higher temperature. At the outlet, a convective-flux boundary condition ($-k\nabla T = 0$) is applied. The flow boundary conditions are: inlet is at a specified mass-flow rate, and outlet gauge pressure is set at 0 Pa. All walls are set to no slip condition. The length of the model geometry is 2.48 mm, which is much longer than the flow entrance length and the thermal entrance length. The Nusselt number for fully developed laminar flow is obtained from the fully developed fraction (from 1.24 to 2.17 mm as shown in Figure 8.3). The thermal and hydraulic behaviors of the high-pressure channel with aligned pillars and the low-pressure channel with the two different aligned pillar arrangements are analyzed in the same way.

The length of the channel between the start and the point where the hydraulically and thermally fully developed flow begins is called the entrance length [31]. For a laminar flow, the flow entrance length denoted by L_F is estimated by:

$$L_F = 0.05 Re D_h \tag{8.3}$$

The thermal entrance length, L_T, is a function of the Reynolds number, the Prandtl number and the hydraulic diameter of the channel:

$$L_T = 0.05 Re Pr D_h \tag{8.4}$$

The hydraulic diameter of the rectangular channel with pillars, D_h, is defined as:

$$D_h = 4\varepsilon V / A_w \tag{8.5}$$

where A_w is the wetted area of the channel with pillars, ε is the porosity of the channel with pillars, and V is the total volume of the channel.

8.3 Thermal characteristics

The convective heat transfer is characterized by a dimensionless Nusselt number given by Eq. 2.7. The heat transfer coefficient of the channel with pillars, h, is defined as:

$$h = \frac{\dot{Q}}{A_t \Delta T_m} \tag{8.6}$$

Here, A_t is the total isothermal area, and $\dot{Q}$ is the heat flow transferred to the fluids or absorbed from the fluids, is calculated as:

$$\dot{Q} = \dot{m} c_p \left(T_{m,o} - T_{m,i}\right) \tag{8.7}$$

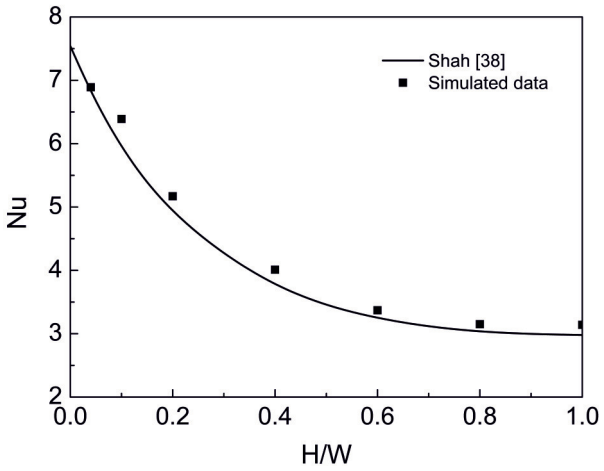

Figure 8.4: Nusselt number in rectangular channel without pillars under constant temperature boundary condition. Modeling results compared to literature data.

where $\dot{m}$ is the mass-flow rate, $T_{m,i}$ and $T_{m,o}$ are the inlet and outlet temperatures of the fully developed fraction in the model geometry. The mean fluid temperatures are weighted average value, which could be obtained from the simulation of Ansys Fluent.

The log mean temperature difference, ΔT_m, is defined by the logarithmic mean as follows:

$$\Delta T_m = \frac{(T_w - T_{m,o}) - (T_w - T_{m,i})}{\ln\left((T_w - T_{m,o}) / (T_w - T_{m,i})\right)} \tag{8.8}$$

Here, T_w is the temperature of the isothermal channel wall.

This numerical method of determining the Nusselt number is validated by considering the case of a rectangular cross-section channel without pillars. The Nusselt number for such a geometry is given by Eq. 8.2 [38]. A rectangular slab is chosen as the model geometry with fixed length (10 mm) and width (1 mm) and various heights (from 0.04 to 1 mm) to cover a wide range of aspect ratios of height-to-width. The thermal and flow boundary conditions of the model are set as follows: Inlet temperature is specified at 300 K, while the outlet is set as convective flux ($-k\nabla T = 0$). The flow condition at the inlet is a specified mass-flow rate, and the outlet gauge pressure is set at 0 Pa. The no slip flow condition is used at all the wall surfaces and these surfaces are assumed to be at a constant temperature of 305 K. Figure 8.4 shows the Nusselt numbers obtained from the modeling and the calculated values based on Eq. 8.2. The relative error between the two values is less than 9%, which means that the numerical modeling method can be used to estimate the Nusselt number in rectangular channels with pillars.

Figure 8.5 shows the increase of the Nusselt number of the high-pressure channel with increasing Reynolds number for flow patterns a and b as depicted in Figure 8.6. The

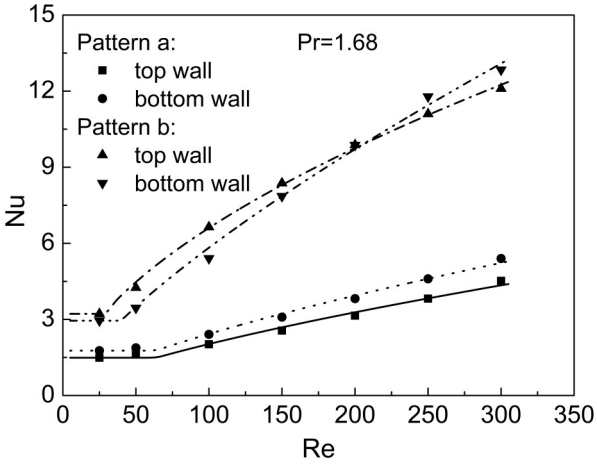

Figure 8.5: Nusselt number in the high-pressure channel as a function of the Reynolds number. Patterns a and b are shown in Figure 8.6.

Nusselt number with aligned arrangement (pattern a) is smaller than that with a staggered arrangement (pattern b) at the same Reynolds number. The larger Nusselt number is caused by flow vortices around the staggered pillars. A. Valencia [123] investigated the heat transfer enhancement in a channel with a built-in rectangular cylinder and indicated that these vortices generated a noteworthy heat transfer enhancement but also a considerable pressure drop increase. The flow separation resulting from these vortices around the pillars are clearly shown in Figure 8.6, depicting the velocity distribution over the high-pressure channel. The pillars in the aligned arrangement hardly cause vortices and the flow is not disturbed. They mainly function as separation wall for the fluid flow. The flow velocity among the pillars in flow direction is quite small, and the heat flux between the fluid and the wall in these regions is limited. As shown in Figure 8.5, the Nusselt number is close to constant as the case of fully developed flow in the rectangular channel without pillars when the Reynolds number is smaller than a critical value (dependent on flow pattern and thermal boundary condition).

Dimensional analysis suggests that the Nusselt number in across flows with staggered and aligned pillar matrices varies with the Reynolds and Prandtl numbers when the Reynolds number is hgher than the critical value. The Nusselt number in this case appeared to fit well to the following correlation:

$$Nu = CRe^{m}Pr^{n} \tag{8.9}$$

The correlations of the Nusselt, the Reynolds, and the Prandtl numbers in the high-pressure channel with different pillar arrangements and boundary conditions in the Prandtl number numbe range $0.76 < Pr < 1.68$ are as follows:

Pattern a with isothermal top wall

$$Nu = \begin{cases} 1.49 & (Re < 60) \\ 0.064 Re^{0.69} Pr^{0.51} & (60 \leq Re < 300) \end{cases} \tag{8.10}$$

Pattern a with isothermal bottom wall

$$Nu = \begin{cases} 1.77 & (Re < 60) \\ 0.076 Re^{0.70} Pr^{0.48} & (60 \leq Re < 300) \end{cases} \tag{8.11}$$

Pattern b with isothermal top wall

$$Nu = \begin{cases} 3.22 & (Re < 30) \\ 0.42 Re^{0.56} Pr^{0.34} & (30 \leq Re < 300) \end{cases} \tag{8.12}$$

Pattern b with isothermal bottom wall

$$Nu = \begin{cases} 2.95 & (Re < 40) \\ 0.16 Re^{0.74} Pr^{0.39} & (40 \leq Re < 300) \end{cases} \tag{8.13}$$

Figure 8.7 shows the Nusselt number in the low-pressure channel with different aligned pillar arrangements. Compared to the flow distribution in the high-pressure channel with the aligned pillar matrix, the dead spot area in the low-pressure channel is smaller because of the smaller pillar diameter. This can be seen by comparing the velocity distributions shown in Figures 8.6 and 8.8. For the thermal boundary condition

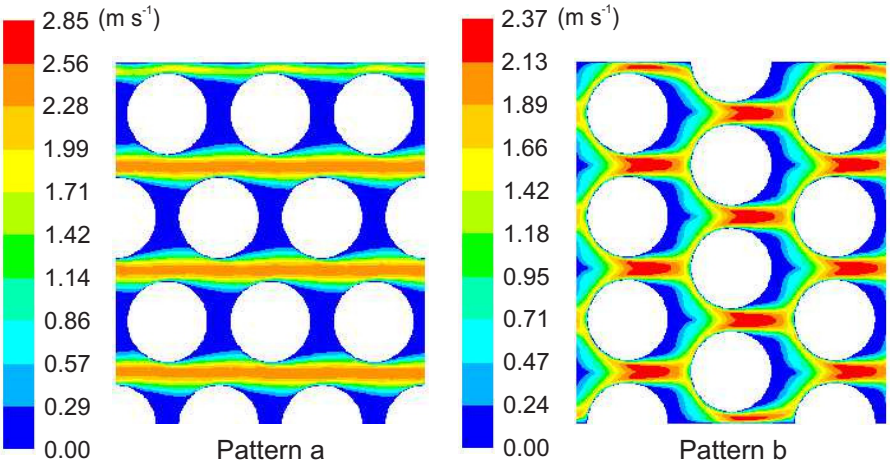

Figure 8.6: Contours of constant velocity in the high-pressure channel with patterns a and b.

of isothermal bottom wall, the Nusselt number of the aligned pattern c is smaller than that of pattern d. The heat transfer enhancement due to disturbed flow in pattern d apparently is larger.

Again, the correlations of the Nusselt, the Reynolds, and the Prandtl numbers in the low-pressure channel were obtained by fitting simulated data. The resulting correlations for pillar matrix of pattern c and d under different boundary conditions in the Reynolds number range $100 < Re < 300$ and Prandtl number numbe range $0.72 < Pr < 0.98$ are as follows:

Pattern c with isothermal top wall

$$Nu = \begin{cases} 2.43 & (Re < 100) \\ 1.35 Re^{0.15} Pr^{0.14} & (100 \leq Re < 300) \end{cases} \tag{8.14}$$

Pattern c with isothermal bottom wall

$$Nu = \begin{cases} 2.92 & (Re < 100) \\ 1.65 Re^{0.14} Pr^{0.14} & (100 \leq Re < 300) \end{cases} \tag{8.15}$$

Pattern d with isothermal top wall

$$Nu = \begin{cases} 3.41 & (Re < 150) \\ 0.19 Re^{0.61} Pr^{0.35} & (150 \leq Re < 300) \end{cases} \tag{8.16}$$

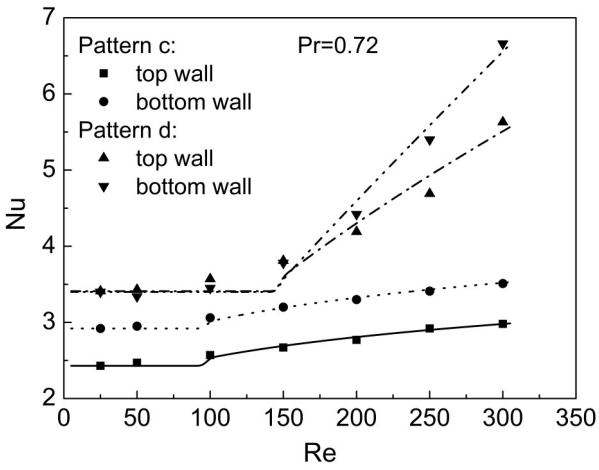

Figure 8.7: Nusselt number of low-pressure channel as a function of Reynolds number. Patterns c and d are shown in Figure 8.8.

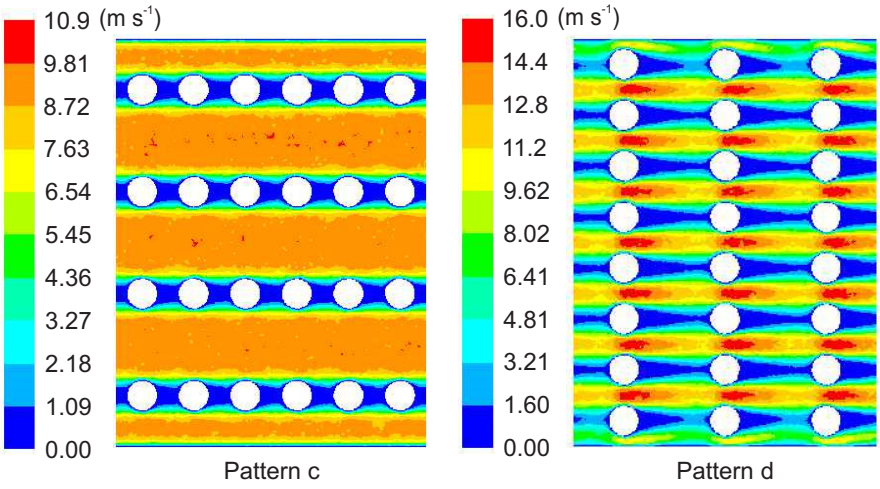

Figure 8.8: Contours of constant velocity in the low-pressure channel with patterns c and d.

Pattern d with isothermal bottom wall

$$Nu = \begin{cases} 3.40 & (Re < 150) \\ 0.051 Re^{0.88} Pr^{0.42} & (150 \leq Re < 300) \end{cases} \tag{8.17}$$

8.4 Hydraulic characteristics

The Darcy-Weisbach friction factor is a dimensionless quantity used in the Darcy-Weisbach equation given in Eq. 2.3, for the description of friction losses in channel flow. The Darcy-Weisbach friction factor of a channel with a pillar matrix is a function of the Reynolds number, given by:

$$f = CRe^{m} \tag{8.18}$$

According to the pressure drop of the fully developed fraction of the three dimensional model, the corresponding Darcy-Weisbach friction factor can be calculated by Eq. 2.3. The result is shown in Figure 8.9. As can be expected, the friction factor of the high-pressure channel with staggered pillars is higher than that of the channel with aligned pillars. The fluid of the channel with aligned pillar flows mainly in straight lines and is not disturbed as in the staggered array (see Figure 8.6). The friction factor of the low-pressure channel with pattern c is smaller than that of pattern d because the physical velocity in pattern d is much higher at the same Reynolds number. The resulting correlations of the Darcy-Weisbach friction factor, and the Reynolds numbers in the range $25 < Re < 300$ are as follows:

Pattern a

$$f = 47.56Re^{-0.78} \tag{8.19}$$

Pattern b

$$f = 24.00Re^{-0.51} \tag{8.20}$$

Pattern c

$$f = 61.76Re^{-0.92} \tag{8.21}$$

Pattern d

$$f = 43.84Re^{-0.73} \tag{8.22}$$

8.5 Impact on microcooler design

By combining Figures 8.5, 8.7, 8.9, it is found that pattern b of the high-pressure channel and pattern d of the low-pressure channel provide a higher heat transfer at the expense of a higher pressure drop. The pressure drop along the high-pressure channel has little influence on the performance of the JT microcooler. However, the pressure drop along the low-pressure channel determines the temperature in the evaporator and it thus affects the lowest temperature that the JT microcooler can reach. So far, our microcoolers were based on patterns a and c and thus the performance of the microcoolers can be improved by replacing the current pattern a of the high-pressure channel with pattern b.

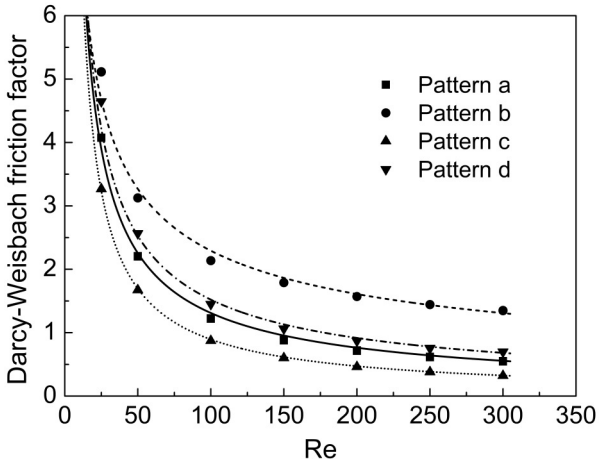

Figure 8.9: Darcy-Weisbach friction factor as a function of the Reynolds number. Patterns a and b shown in Figure 8.6. Patterns c and d shown in Figure 8.8.

Taking the microcooler described in the reference [124] as an example, the flow patterns of the high and low-pressure channels of the microcooler are patterns a and c. The measured cool-down time of the microcooler from 295 to 101 K is about 6.5 minutes when the microcooler is operated with nitrogen gas at a high pressure of 8.0 MPa and a low pressure of 0.60 MPa. The measured net cooling power of the microcooler is 130 mW at 103 K with a mass-flow rate of 16.0 mg s^{-1}. The performance of the microcooler can be predicted based on a dynamic model using the resulting Nusselt number and Darcy-Weisbach friction factor correlations of the corresponding flow pattern. If the pattern a of the high-pressure channel was replaced with pattern b, the microcooler is expected to cool down from 295 to 101 K in 4.0 minutes and have a net cooling power of 170 mW at 103 K with a mass-flow rate of 16.0 mg s^{-1}.

8.6 Conclusions

In this chapter, the thermal and hydraulic performance of the high- and low-pressure channels of CFHXs with pillar matrices are investigated numerically for different patterns. The correlations of the Nusselt number and the Darcy-Weisbach friction factor in the channels with different patterns are obtained from numerical simulation. By using the resulting correlations, the performance of a microcooler with certain patterns can be predicted. In this respect, it was shown that it can be worthwhile to replace an aligned pillar arrangement in the high-pressure line by a staggered arrangement. Thus the heat transfer is improved whereas the increase in fluidic loss is acceptable.

CHAPTER 9

Outlook

This thesis focused on the realization of a 30 K JT cryogenic microcooler by using micromachining technology. Other related issues are also investigated, such as the clogging phenomenon, the utilization, the vacuum packaging and the numerical analysis of the thermal and hydraulic performance of channels with pillar matrices. These issues are summarized in the following chapter, a few promising topics for future research are discussed herein.

9.1 Measures for preventing clogging

A major hurdle in long-term operation of JT microoolers is the clogging caused by the deposition of water that is present as impurity in the working fluid. Ice exhibits strong electronic absorption in the ultraviolet (UV) at wavelengths $\lambda < 170$ nm and strong vibrational absorption in the infrared (IR) region for $3 < \lambda < 150$ μm [125]. If the electromagnetic radiation in the UV and IR regions is not absorbed by the microcooler material (borosilicate glass) or by the working fluid, then it is worthwhile to investigate whether the electromagnetic radiation can be used to remove the ice inside the microcooler without heating up the microcooler.

9.2 Tunable JT restriction

The mass-flow rate of a microcooler is determined by the gas properties (density and viscosity) and by the dimensions of the restriction, following Eq. 4.1. For a microcooler with a fixed restriction, the mass-flow rate increases with decreasing cold-end temperature mostly because the density increases. The microcooler CFHX generally is optimized based on the mass-flow rate at the steady state, which is not efficiently used during the cool-down. A tunable JT restriction allows to adapt the restriction size during the cool-down process. In addition, it facilitates the adjustment of the cooling power during steady-state operation. The restriction deformation can be achieved by an electric field through Piezoelectric effect [24] or a change in temperature through negative thermal expansion materials [126, 127].

9.3 Double-expansion cycle JT cooling

The cold-end temperature of a JT-cooler is determined by the boiling point in the evaporator. The pressure in the evaporator is determined by the outlet pressure of the low-pressure line and the pressure drop along that line. Under the same outlet-pressure condition, a lower cold-end temperature can be obtained by decreasing that pressure drop. Based on Eq. 2.3, the pressure drop through a channel can be reduced by decreasing the mean velocity, the channel length or the Darcy-Weisbach friction factor of the channel or by increasing the hydraulic diameter of the channel. A smaller mean velocity can be obtained by decreasing the mass-flow rate or again by increasing the hydraulic diameter of the channel. Decreasing the mass-flow rate results in a reduction in gross cooling power. A smaller channel length or a larger hydraulic diameter both result in a lower heat exchanger efficiency, which increases the parasitic heat losses and thus will reduce the net cooling power. The Darcy-Weisbach friction factor can, in most cases, only be reduced at the expense of a lower heat transfer in the CFHX.

Using a double-expansion cycle in a JT-cooler is an ingenious way to deal with this issue. In this method, the reduction of the pressure drop is realized by diminishing the mass-flow rate in the low-pressure line, and the reduction in the gross cooling power due to the decreasing mass-flow rate is compensated by lowering the temperature of the high-pressure gas [27]. A JT-cooler with double expansion can be achieved in two different ways as shown in Figure 9.1: an additional JT restriction (R I) in the main stream (a), or in a by-pass return stream (b). In both cases, after the CFHX I the gas flow is divided into two streams. Most of the gas flows back through the low-pressure channel of CFHX I along the non-isobaric line ($3 \rightarrow 8$). Due to the pressure drop in this line, the gas does not follow the isobaric line ($3 \rightarrow 8^{'}$). The other part of the gas continues to the second restriction (R II). Because the amount of gas flowing through the second expansion stage is small, the pressure drop through the return line is relatively small. Therefore, this small amount of gas flow follows the isobaric line ($6 \rightarrow 8$) and thus a lower cold-end temperature can be obtained.

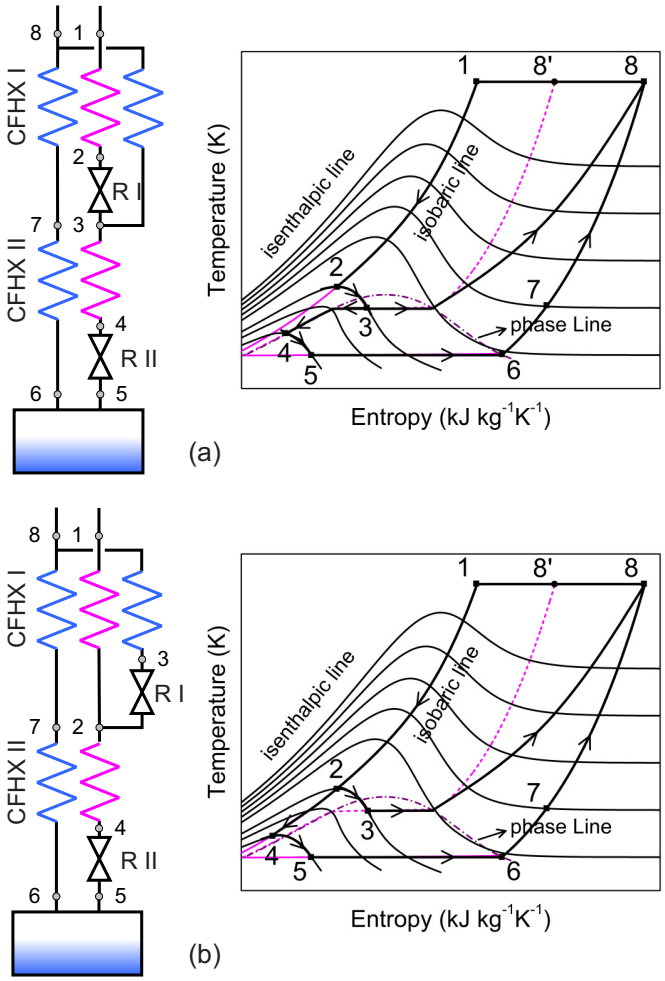

Figure 9.1: Schematic of the Linde-Hampson cooling cycle with double JT expansion. (CFHX: counter flow heat exchanger; R: restriction).

The two different types of JT-coolers with double expansion can be realized by using three glass wafers as shown in Figure 9.2. In the JT-cooler shown in Figure 9.2a, all the high-pressure gas passes through the Restriction I, most of the gas returns to the outlet through the through-holes in the middle wafer. Only a small amount of the gas flows ahead and passes through the Restriction II to reach a lower temperature. In the JT-cooler shown in Figure 9.2b, most of the gas returns to the outlet through the through-holes in the middle wafer and passes the Restriction I before flowing through these holes. The other small amount of the gas only passes through the Restriction II.

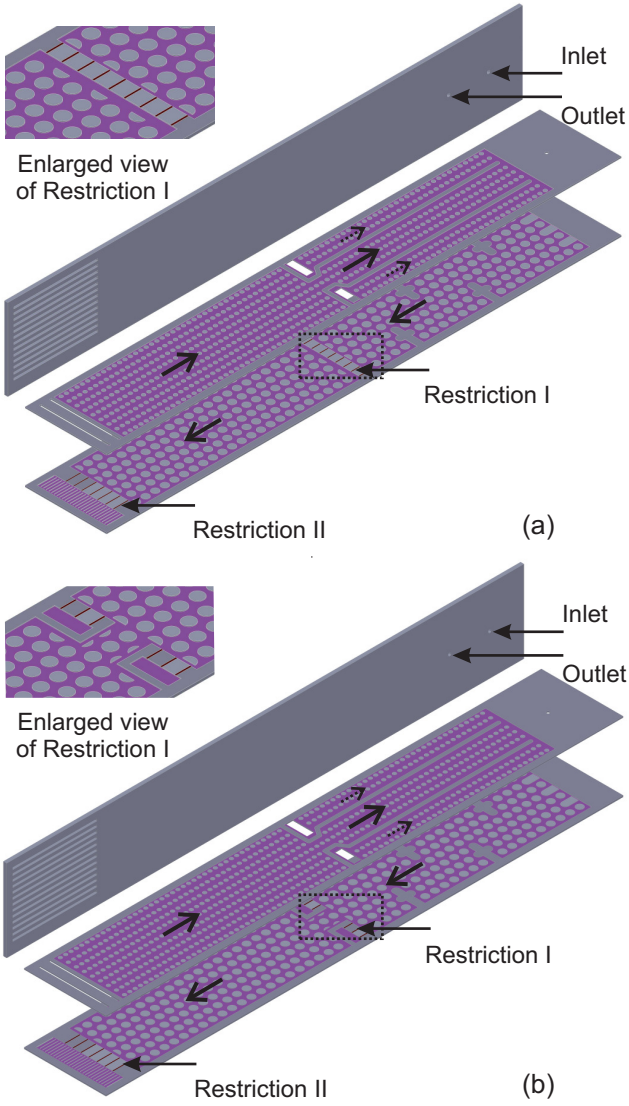

Figure 9.2: Exploded view of the JT-cooler with double expansion.

9.4 Mixed-gas JT cooling

Compared to pure gas, mixed gases provide equivalent cooling power with significantly lower pressure ratio and mass-flow rate. A closed-cycle JT cooling system is easier to realize by combining a compressor with a microcooler using mixed gas as the working fluid. It is feasible to replace nitrogen and hydrogen gas by mixed gases as working fluids

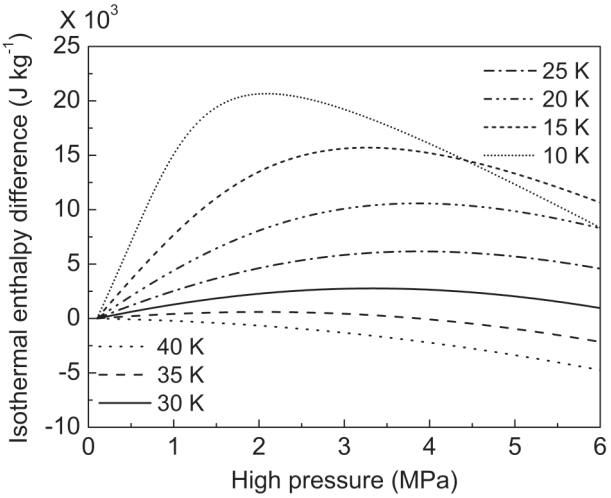

Figure 9.3: Isothermal enthalpy difference versus the high pressure for helium gas with a constant low pressure of 0.10 MPa at different precooling temperatures.

of the 30 K two-stage microcooler. For instance, Maytal [128] used a ternary composition of nitrogen, ethane and propane gas (0.83, 0.10, 0.07 by volume) in a JT cooler. It was found that the JT cooler using mixed gas reached the temperature of nitrogen gas (80 K) but cooled down as fast as argon gas. Sobel [129] explored the possibility of reaching temperatures between 27 and 80 K using mixed gases including 19-40% argon gas and 20.1-80.5% neon gas.

9.5 Three-stage microcooler

30 K is sufficiently cold to cool most electronic devices such as infrared detectors, low-noise amplifiers and high-temperature superconducting devices. To cool superconducting devices based on Nb_3Sn or NbTi, an even lower temperature is required. To reach temperatures near boiling point of helium gas using the JT effect and starting from 300 K, it is necessary to use three stages. A nitrogen stage is used to precool a hydrogen stage, which works as a precool for a helium stage. Figure 9.3 gives the isothermal enthalpy difference of helium gas between varied high pressure and a constant low pressure (0.10 MPa) at different precooling temperatures. With a precooling temperature of 30 K, the maximum isothermal enthalpy difference is $2.77 \cdot 10^3$ J kg^{-1} with a high pressure of 3.3 MPa. Decreasing the precooling temperature can further increase the value of the maximum isothermal enthalpy difference. Aiming at a certain amount of gross cooling power, a higher isothermal enthalpy difference means a lower mass-flow rate, and thus a smaller CFHX.

Appendix

The process of gas permeation and diffusion through vacuum chamber discussed in chapter 7 can be described by the diffusion equations with different boundary and initial conditions. This appendix gives the solution procedure of these equations by the method of separation of variables.

A.1 Permeation

The one-dimensional diffusion equation is:

$$D\frac{\partial^2 c}{\partial^2 x} = \frac{\partial c}{\partial t} \tag{A.1}$$

with the initial and boundary conditions of the permeation process:

$c = 0$	for	$0 \leq x \leq d$	at	$t = 0$
$c = 0$	for	$x = 0$	at	$t > 0$
$c = c_1$	for	$x = d$	at	$t > 0$

First, we need to transform the nonhomogeneous boundary conditions to homogenous ones in order to use the method of separation of variables. Define $w(x,t) = c(x,t) - \frac{x}{d}c_1$ and transform the above problem for $c(x,t)$ into an equivalent problem for $w(x,t)$. So now we have a problem with homogeneous boundary conditions.

$$D\frac{\partial^2 w}{\partial^2 x} = \frac{\partial w}{\partial t} \tag{A.2}$$

with the initial and boundary conditions:

$w = -\frac{x}{d}c_1$	for	$0 \leq x \leq d$	at	$t = 0$
$w = 0$	for	$x = 0$	at	$t > 0$
$w = 0$	for	$x = d$	at	$t > 0$

To solve the equation, we use the method of separation of variables in which we assume that the solution, $w(x,t)$, is the product of two functions, $T(t)$ a function of time only and $X(x)$ a function of the distance x only. With this assumption, our solution becomes:

$$w(x,t) = X(x)\ T(t) \tag{A.3}$$

Since $X(x)$ is a function of x only and $T(t)$ is a function of t only, we obtain the following result when we substitute Eq. A.3 into Eq. A.2:

$$D\frac{\partial^2 w}{\partial^2 x} = DT\frac{\partial^2 X}{\partial^2 x} = \frac{\partial w}{\partial t} = X\frac{\partial T}{\partial t} \tag{A.4}$$

If we divide Eq. A.4 through by the product DXT, we obtain the following equation:

$$\frac{1}{X}\frac{\partial^2 X}{\partial^2 x} = \frac{1}{D}\frac{1}{T}\frac{\partial T}{\partial t} \tag{A.5}$$

The right hand side of Eq. A.5 is a function of t only; the left hand side is a function of x only. The only way that this can be correct is if both sides equal a constant. In order to

simply the solution, we choose the constant to be equal to $-\lambda$. This gives us two ordinary differential equations to solve:

$$\frac{1}{X}\frac{\partial^2 X}{\partial^2 x} = -\lambda \tag{A.6}$$

$$\frac{1}{D}\frac{1}{T}\frac{\partial T}{\partial t} = -\lambda \tag{A.7}$$

The boundary conditions become $w(0,t) = X(0)T(t) = 0$ and $w(d,t) = X(d)T(t) = 0$. Taking $T(t) = 0$ would give $w = 0$ for all time and space (called the trivial solution), which does not satisfy the initial condition. Hence the above equations are only satisfied if:

$$X(0) = X(1) = 0 \tag{A.8}$$

Now, we obtain a boundary value problem for $X(x)$. There are 3 cases: $\lambda < 0$; $\lambda = 0$; $\lambda > 0$.

Case A: $\lambda < 0$, then the general solution to Eq. A.6 is:

$$X(x) = A\exp\left(\sqrt{-\lambda}x\right) + B\exp\left(-\sqrt{-\lambda}x\right) \tag{A.9}$$

Constant A and B found from imposing the boundary conditions Eq. A.8 in Eq. A.9:

$$X(0) = A + B, \quad X(d) = A\exp\left(\sqrt{-\lambda}d\right) + B\exp\left(-\sqrt{-\lambda}d\right) = 0 \tag{A.10}$$

This gives $A = -B$, the second then gives $A\exp\left(2\sqrt{-\lambda}d\right) - 1 = 0$, and since $\sqrt{-\lambda}d > 0$, we have $A = B = w = 0$, which is the trivial solution. Thus we discard the case $\lambda < 0$.

Case B: $\lambda = 0$, then $X(x) = A + Bx$, and the boundary conditions imply $X(0) = A = 0$, $X(d) = Bd = 0$, so that $A = B = w = 0$. We discard this case also.

Case C: $\lambda > 0$, then the general solution to Eq. A.6 is:

$$X(x) = A\cos\left(\sqrt{\lambda}x\right) + B\sin\left(\sqrt{\lambda}x\right) \tag{A.11}$$

The boundary condition $X(0) = 0$ says $A = 0$. The second condition says that $X(d) = B\sin\left(\sqrt{\lambda}d\right) = 0$. To avoid only having the trivial solution, we must have $\sin\left(\sqrt{\lambda}d\right) = 0$. In other words, $\lambda = \lambda_k = \left(\frac{k\pi}{d}\right)^2 (k = 1,2,3,...)$.

Solving the Eq. A.7, we find:

$$T(t) = A\exp\left(-D\lambda t\right) \tag{A.12}$$

Hence we have the general solution:

$$w(x,t) = X(x)T(t) = \sum_{k=1}^{\infty} A_k \exp\left(-\left(\frac{k\pi}{d}\right)^2 Dt\right)\sin\left(\frac{k\pi x}{d}\right) \tag{A.13}$$

The coefficients A_k are to be fixed by the initial conditions:

$$w(x,0) = \sum_{k=1}^{\infty} A_k \sin\left(\frac{k\pi x}{d}\right) = -\frac{x}{d}c_1 \tag{A.14}$$

Note, that this is just the Fourier sine series of $-\frac{x}{d}c_1$. To solve for A_k, we use the property for the eigenfunctions $\sin\left(\frac{k\pi}{d}x\right)$:

$$\int_0^d \sin\left(\frac{k\pi x}{d}\right)\sin\left(\frac{m\pi x}{d}\right)dx = \begin{cases} 0, m \neq k \\ \frac{d}{2}, m = k \end{cases} \tag{A.15}$$

Multiplying both sides of Eq. A.14 by $\sin\left(\frac{m\pi x}{d}\right)$ and integrating from 0 to d gives:

$$\sum_{k=1}^{\infty} A_k \int_0^d \sin\left(\frac{k\pi x}{d}\right)\sin\left(\frac{m\pi x}{d}\right)dx = \int_0^d -\frac{x}{d}c_1 \sin\left(\frac{m\pi x}{d}\right)dx \tag{A.16}$$

Hence we know that:

$$A_k = \frac{2}{d}\int_0^d -\frac{x}{d}c_1 \sin\left(\frac{k\pi x}{d}\right)dx = \frac{2c_1}{k\pi}\cos(k\pi) \tag{A.17}$$

So, the solution to Eq. A.2 satisfying the boundary and initial condition is:

$$w(x,t) = X(x)\,T(t) = \sum_{k=1}^{\infty} \frac{2c_1}{k\pi}\cos(k\pi)\exp\left(-\left(\frac{k\pi}{d}\right)^2 Dt\right)\sin\left(\frac{k\pi x}{d}\right) \tag{A.18}$$

And the solution to Eq. A.1 is:

$$c(x,t) = \frac{xc_1}{d} + \sum_{k=1}^{\infty} \frac{2c_1}{k\pi}\cos(k\pi)\exp\left(-\left(\frac{k\pi}{d}\right)^2 Dt\right)\sin\left(\frac{k\pi x}{d}\right) \tag{A.19}$$

Since $\frac{\cos(k\pi)}{k} = \frac{(-1)^n}{n}$, the equation is equal to:

$$c(x,t) = \frac{xc_1}{d} + \frac{2c_1}{\pi}\sum_{n=1}^{\infty} \frac{(-1)^n}{n}\sin\left(\frac{n\pi x}{d}\right)\exp\left(-\left(\frac{n\pi}{d}\right)^2 Dt\right) \tag{A.20}$$

A.2 Diffusion

The initial and boundary conditions of the diffusion process are:

$c = c_1$	for	$0 \leq x \leq d$	at	$t = 0$
$c = 0$	for	$x = 0$	at	$t > 0$
$c = 0$	for	$x = d$	at	$t > 0$

From the above analysis we know the diffusion equation with this type of initial and boundary conditions have the general solution like Eq. A.13, that is:

$$c(x,t) = \sum_{k=1}^{\infty} A_k \exp\left(-\left(\frac{k\pi}{d}\right)^2 Dt\right) \sin\left(\frac{k\pi x}{d}\right) \tag{A.21}$$

The coefficients A_k in this case are to be fixed by the initial conditions:

$$c(x,0) = \sum_{k=1}^{\infty} A_k \sin\left(\frac{k\pi x}{d}\right) = c_1 \tag{A.22}$$

Similar to the derivation of Eq. A.16, we know that:

$$A_k = \frac{2}{d}\int_0^d c_1 \sin\left(\frac{k\pi x}{d}\right) dx = \frac{2c_1}{k\pi}\left(1-\cos(k\pi)\right) \tag{A.23}$$

So, the solution to the equation satisfying the boundary and initial conditions is:

$$c(x,t) = X(x)\,T(t) = \sum_{k=1}^{\infty} \frac{2c_1}{k\pi}\left(1-\cos(k\pi)\right) \exp\left(-\left(\frac{k\pi}{d}\right)^2 Dt\right) \sin\left(\frac{k\pi x}{d}\right) \tag{A.24}$$

When k is even, the term $1-\cos(k\pi) = 0$, so the solution is equal to:

$$c(x,t) = \frac{4c_1}{\pi} \sum_{n=0}^{\infty} (2n+1)^{-1} \sin\frac{\pi(2n+1)x}{d} \exp\left(-\left(\frac{\pi(2n+1)}{d}\right)^2 Dt\right) \tag{A.25}$$

Bibliography

[1] Rogalski A 2003 Infrared detectors: status and trends *Prog. Quant. Eelectron.* **27** 59-210.

[2] Wadefalk N *et al* 2003 Cryogenic wide-band ultra-low-noise IF amplifiers operating at ultra-low DC power *IEEE Trans. Microw. Theory Tech.* **51** 1705-11.

[3] International Institute of Refrigeration 1976 *New International Dictionary of Refrigeration* (Paris: International Institute of Refrigeration).

[4] Clarke J, Interview with Pulizzi F 2011 SQUIDs for everything *Nat. Mater.* **10** 262-3.

[5] Nisenoff M 1995 Cryocoolers and high temperature superconductors: advancing toward commercial applications *Cryocoolers* **8** 913-7.

[6] Walker G and Bingham R 1990 Micro and nano cryocoolers: speculation on future development *Proceedings of the Sixth International Cryocooler Conference* 363-75.

[7] Burger J 2001 *Cryogenic microcooling: A micromachined cold stage operating with a sorption compressor in a vapor compression cycle* (Enschede: University of Twente).

[8] Lerou P P P M 2007 *Micromachined Joule-Thomson cryocooler* (Enschede: University of Twente).

[9] Derking J H 2011 *Distributed Joule-Thomson microcooling for optical detectors in space* (Enschede: University of Twente).

[10] Foerg W 2002 History of cryogenics: the epoch of the pioneers from the beginning to the year 1911 *Int. J. Refrig.* **25** 283-92.

[11] Radebaugh R 2009 Cryocoolers: the state of the art and recent developments *J. Phys.: Condens. Matter.* **21** 164219.

[12] Callen H B 1985 *Thermodynamics and an Introduction to Thermostatistics* (New York: Wiley), p.160-7.

[13] Lemmon E W, Huber M L and McLinden M O 2007 *Refprop version 8.0, NIST standard reference database 23* (Gaithersburg: U.S. Department of Commerce).

[14] Walker G and Bingham E R 1994 *Low-Capacity Cryogenic Refrigeration* (New York: Oxford University Press Inc.), p.43-102.

[15] Stephens S W 1968 Advanced design of Joule-Thomson coolers for infra-red detectors *Infrared Phys.* **8** 25-35.

[16] Garvey S, Logan S, Rowe R and Little W A 1983 Performance characteristics of a low-flow rate 25 mW, LN_2 Joule-Thomson refrigerator fabricated by photolithographic means *Appl. Phys. Lett.* **42** 1048-50.

[17] Mikulin E, Shevich J, Danilenko T, Solovov N and Veselov V 1992 The miniature Joule-Thomson refrigerator *Cryogenics* **32** 17-9.

[18] Chorowski M, Bodio E and Wilczek M 1994 Development and testing of a miniature Joule-Thomson refrigerator with sintered powder heat exchanger *Adv. Cryog. Eng.* **39** 1475-81.

[19] Holland H J, Burger J F, Boersma N, ter Brake H J M and Rogalla H 1998 Miniature 10-150 mW Linde-Hampson cooler with glass-tube heat exchanger operating with nitrogen *Cryogenics* **38** 407-10.

[20] Lerou P P P M, Veenstra T T, Burger J F, ter Brake H J M and Rogalla H 2005 Optimization of counterflow heat exchanger geometry through minimization of entropy generation *Cryogenics* **45** 659-69.

[21] Lerou P P P M, Venhorst G C F, Berends C F, Veenstra T T, Blom M, Burger J F, ter Brake H J M and Rogalla H 2006 Fabrication of a micro cryogenic cooler using MEMS-technology *J. Micromech. Microeng.* **16** 1919-25.

[22] Lerou P P P M, ter Brake H J M, Burger J F, Holland H J and Rogalla H 2007 Characterization of micromachined cryogenic coolers *J. Micromech. Microeng.* **17** 1956-60.

[23] Lin M H, Bradley P E, Huber M L, Lewis R, Radebaugh R and Lee Y C 2010 Mixed refrigerants for a glass capillary micro cryogenic cooler *Cryogenics* **50** 439-42.

[24] Park J M, Taylor R P, Evans A T, Brosten T R, Nellis G F, Klein S A, Feller J R, Salerno L and Gianchandani Y B 2008 A piezoelectric microvalve for cryogenic applications *J. Micromech. Microeng.* **18** 015023.

[25] Zhu W, Park J M, White M J, Nellis G F and Gianchandani Y B 2011 Experimental evaluation of an adaptive Joule-Thomson cooling system including silicon-microfabricated heat exchanger and microvalve components *J. Vac. Sci. Technol. A* **29** 021005.

[26] Little W A Presented at Cryogenic Engineering Conference, Los Angeles, 1989, private communication, 2012, February 18.

[27] Little W A 1990 Advances in Joule-Thomson cooling *Adv. Cryog. Eng.* **35B** 1305-14.

[28] Gad-el-Hak M 1999 The fluid mechanics of microdevices—The Freeman Scholar Lecture *J. Fluids Eng.* **121** 5-33.

[29] Faghri A, Zhang Y and Howell J 2010 *Advanced Heat and Mass Transfer* (Columbia: Global Digital Press), p.23-4.

[30] Kaka S, Liu H and Pramuanjaroenkij A 2012 *Heat Exchangers: Selection, Rating, and Thermal Design* (New York: CRC Press), p.159.

[31] Bejan A 1993 *Heat Transfer* (New York: Wiley), p.290-334.

[32] Wu P Y and Little W A 1983 Measurement of friction factors for the flow of gases in very fine channels used for microminiature Joule-Thomson refrigerators *Cryogenics* **23** 273-7.

[33] Peng X F and Peterson G P 1996 Convective heat transfer and flow friction for water flow in microchannel structures *Int. J. Heat Mass Transfer* **39** 2599-608.

[34] Mala G M and Li D 1999 Flow characteristics of water in microtubes *Int. J. Heat Fluid Flow* **20** 142-8.

[35] Sharp K V and Adrian R J 2004 Transition from laminar to turbulent flow in liquid filled microtubes *Exp. Fluids* **36** 741-7.

[36] Hetsroni G, Mosyak A, Pogrebnyak E and Yarin L P 2005 Fluid flow in micro-channels *Int. J. Heat Mass Transfer* **48** 1982-98.

[37] Moody L F and Princeton N J 1944 Friction factors for pipe flow *Trans. ASME* **66** 671-84.

[38] Shah R K and London A L 1978 *Laminar Flow Forced Convection in Ducts: A Source Book for Compact Heat Exchanger Analytical Data* (New York: Academic Press), p.196-222.

[39] Dittus F W and Boelter L M K 1930 *Heat Transfer in Automobile Radiators of the Tubular Type* (Berkeley: University of California press), p.443-61.

[40] Gnielinski V 1976 New equations for heat and mass transfer in turbulent pipe and channel flow *Int. Chem. Eng.* **16** 359-68.

[41] Palm B 2001 Heat transfer in microchannels *Microscale Thermophys. Eng.* **5** 155-75.

[42] Wu P Y and Little W A 1984 Measurement of the heat transfer characteristics of gas flow in fine channel heat exchangers used for microminiature refrigerators *Cryogenics* **24** 415-20.

[43] Koo J and Kleinstreuer C 2004 Viscous dissipation effects in microtubes and microchannels *Int. J. Heat Mass Transfer* **47** 3159-69.

[44] Yang C, Li D and Masliyah J H 1998 Modeling forced liquid convection in rectangular microchannels with electrokinetic effects *Int. J. Heat Mass Transfer* **41** 4229-49.

[45] O'Hanlon J F 2003 *A User's Guide to Vacuum Technology* (New York: Wiley), p.20-1.

[46] Cao H S, Lerou P P P M, Mudaliar A V, Holland H J, Derking J H, Zalewski D R and ter Brake H J M 2011 Analysis of multi-stage Joule-Thomson microcoolers *Cryocoolers* **16** 481-7.

[47] MathWorks, Natick, USA, ⟨http://www.mathworks.com⟩.

[48] Cao H S, Vanapalli S, Holland H J, Vermeer C H and ter Brake H J M 2013 Clogging in micromachined Joule-Thomson coolers: Mechanism and preventive measures *Appl. Phys. Lett.* **103** 034107.

[49] Cao H S, Mudaliar A V, Derking J H, Lerou P P P M, Holland H J, Zalewski D R, Vanapalli S and ter Brake H J M 2012 Design and optimization of a two-stage 28 K Joule-Thomson microcooler *Cryogenics* **52** 51-7.

[50] Wu M K, Ashburn J R, Torng C J, Hor P H, Meng R L, Gao L, Huang Z J, Wang Y Q and Chu C W 1987 Superconductivity at 93 K in a new mixed-phase Y-Ba-Cu-O compound system at ambient pressure *Phys. Rev. Lett.* **58** 908-10.

[51] Derking J H, Holland H J, Lerou P P P M, Tirolien T and ter Brake H J M 2012 Micromachined Joule-Thomson cold stages operating in the temperature range 80-250 K *Int. J. Refrig.* **35** 1200-7.

[52] Little W A 1984 Microminiature refrigeration *Rev. Sci. Instrum.* **55** 661-80.

[53] Zhu W B, White M J, Nellis G F, Klein S A and Gianchandani Y B 2010 A Si/Glass Bulk-Micromachined Cryogenic Heat Exchanger for High Heat Loads: Fabrication, Test, and Application Results *J. Microelectromech. Syst.* **19** 38-47.

[54] Lerou P P P M, ter Brake H J M, Holland H J, Burger J F and Rogalla H 2007 Insight into clogging of micromachined cryogenic coolers *Appl. Phys. Lett.* **90** 064102.

[55] Derking J H, Holland H J, Tirolien T and ter Brake H J M 2012 A miniature Joule-Thomson cooler for optical detectors in space *Rev. Sci. Instrum.* **83** 045117.

[56] Poling B E, Prausnitz J M and O'Connell J P 2001 *The Properties of Gases and Liquids* (New York: McGraw-Hill), p.11.1-11.55.

[57] Riazi M R and Whitson C H 1993 Estimating diffusion coefficients of dense fluids *Ind. Eng. Chem. Res.* **32** 3081-8.

[58] Neufeld P D, Janzen A R and Aziz R A 1972 Empirical Equations to Calculate 16 of the Transport Collision Integrals $\Omega^{(l,s)*}$ for the Lennard-Jones (12–6) Potential *J. Chem. Phys.* **57** 1100-2.

[59] Pitzer K S 1955 The volumetric and thermodynamic properties of fluids. I. Theoretical basis and virial coefficients *J. Am. Chem. Soc.* **77** 3427-33.

[60] Hertz H 1882 Ueber die Verdunstung der Flüssigkeiten, insbesonderedes Quecksilbers, im luftleeren Raume *Ann. Phys.* **253** 177-193.

[61] Knudsen M 1915 Die maximale Verdampfungsgeschwindigkeit des Quecksilbers *Ann. Phys.* **352** 697-708.

[62] Langmuir I 1913 The Vapor Pressure of Metallic Tungsten *Phys. Rev.* **2** 329-342.

[63] Haynes D R, Tro N J and George S M 1992 Condensation and evaporation of H_2O on ice surfaces *J. Phys. Chem.* **96** 8502-9.

[64] Chaix L, van den Bergh H and Rossi M J 1998 Real-time kinetic measurements of the condensation and evaporation of D_2O molecules on ice at 140 K $<$ T $<$ 220 K *J. Phys. Chem. A* **102** 10300-9.

[65] Fraser H J, Collings M P, McCoustra M R S and Williams D A 2001 Thermal desorption of water ice in the interstellar medium *Mon. Not. R. Astron. Soc.* **327** 1165-72.

[66] Delval C and Rossi M J 2004 The kinetics of condensation and evaporation of H_2O from pure ice in the range 173-223 K: a quartz crystal microbalance study *Phys. Chem. Chem. Phys.* **6** 4665-76.

[67] Pratte P, van den Bergh H and Rossi M J 2006 The kinetics of H_2O vapor condensation and evaporation on different types of ice in the range 130-210 K *J. Phys. Chem. A* **110** 3042-58.

[68] Lerou P P P M Micro-cooling device, EP2444769 A1 (2010).

[69] Carilli C L and Rawlings S 2004 Motivation, key science projects, standards and assumptions *New Astron. Rev.* **48** 979-84.

[70] Cappy A 1988 Noise modeling and measurement techniques [HEMTs] *IEEE Trans. Microw. Theory Techn.* **36** 1-10.

[71] Pospieszalski M W 2005 Extremely low-noise amplification with cryogenic FETs and HFETs: 1970-2004 *IEEE Microw. Mag.* **6** 62-75.

[72] Pospieszalski M W 1989 Modeling of noise parameters of MESFETs and MODFETs and their frequency and temperature dependence *IEEE Trans. Microw. Theory Techn.* **37** 1340-50.

[73] Risacher C and Belitsky V 2003 GaAs HEMT low-noise cryogenic amplifiers from C-band to X-band with 0.7-K/GHz noise temperature *IEEE Microw. Wireless Compon. Lett.* **13** 96-8.

[74] Weinreb S, Bardin J C and Mani H 2007 Design of cryogenic SiGe low-noise amplifiers *IEEE Trans. Microw. Theory Techn.* **55** 2306-12.

[75] Schleeh J, Wadefalk N, Nilsson P A, Starski J P and Grahn J 2013 Cryogenic broadband ultra-low-noise MMIC LNAs for radio astronomy applications *IEEE Trans. Microw. Theory Techn.* **61** 871-7.

[76] Schreuder F and Bij De Vaate J G 2006 Localized LNA cooling in vacuum *Proceedings of the 12th International Workshop on Thermal investigation of ICs and systems* 175-9.

[77] Maytal B Z, Van Sciver S W and McMahon P D 1990 Thermodynamic Analysis of Mixed Fluid Joule-Thomson Cryocoolers *Proceedings of the 6th International Cryocoolers Conference* 111-35.

[78] Cao H S, Holland H J, Vermeer C H, Vanapalli S, Lerou P P P M, Blom M and ter Brake H J M 2013 Micromachined cryogenic cooler for cooling electronic devices down to 30 K *J. Micromech. Microeng.* **23** 025014.

[79] Thierauf S C 2004 *High-speed circuit board signal integrity* (Norwood: Artech House), p.185-207.

[80] Gooch R and Schimert T 2003 Low-cost wafer-level vacuum packaging for MEMS *MRS Bull.* **28** 55-9.

[81] Anthony T R 1983 Anodic bonding of imperfect surfaces *J. Appl. Phys.* **54** 2419-28.

[82] Cheng Y T, Hsu W T, Najafi K, Nguyen C T C and Lin L W 2002 Vacuum packaging technology using localized aluminum/silicon-to-glass bonding *J. Microelectromech. Syst.* **11** 556-65.

[83] Sparks D R, Massoud-Ansari S and Najafi N 2004 Reliable vacuum packaging using NanoGetters^{TM} and glass frit bonding *Reliability, Testing and Characterization of MEMS/MOEMS III, Proceedings of SPIE* **5343** 70-8.

[84] Sparks D R, Massoud-Ansari S and Najafi N 2003 Chip-level vacuum packaging of micromachines using NanoGetters *IEEE Trans. Adv. Packag.* **26** 277-82.

[85] Mitchell J S and Najafi K 2009 A detailed study of yield and reliability for vacuum packages fabricated in a wafer-level Au-Si eutectic bonding process *The 15th International Conference on Solid-state Sensors, Actuators and Microsystems* 841-4.

[86] O'Hanlon J F 2003 *A User's Guide to Vacuum Technology* (New York: Wiley), p.57-77.

[87] Danielson P 2001 Desorbing water in vacuum systems: bakeout or UV? *R&D Mag.* **43** 57-9.

[88] Dobrozemsky R 1987 Sorption dynamics of water vapor under atmospheric conditions *J. Vac. Sci. Technol. A* **5** 2520-1.

[89] Dobrozemsky R 1995 Reduction of water adsorption on technical surfaces in the atmosphere *Vacuum* **46** 789-92.

[90] Redhead P A 1995 Modeling the pump-down of a reversibly adsorbed phase. I. Monolayer and submonolayer initial coverage *J. Vac. Sci. Technol. A* **13** 467-75.

[91] Elsey R J 1975 Outgassing of vacuum materials I : A paper in our education series: The theory and practice of vacuum science and technology in schools and colleges *Vacuum* **25** 299-306.

[92] Moraw M and Prasol H 1998 The influence of readsorption on the measurement of outgassing kinetics of metals *Vacuum* **49** 353-8.

[93] Calder R and Lewin G 1967 Reduction of stainless-steel outgassing in ultra-high vacuum *Br. J. Appl. Phys.* **18** 1459-72.

[94] Perkins W G 1973 Permeation and outgassing of vacuum materials *J. Vac. Sci. Technol.* **10** 543-56.

[95] Louthan Jr M R and Derrick R G 1975 Hydrogen transport in austenitic stainless steel *Corros. Sci.* **15** 565-77.

[96] Rogers W A, Buritz R S and Alpert D 1954 Diffusion coefficient, solubility, and permeability for helium in glass *J. Appl. Phys.* **25** 868-75.

[97] Choa S H 2005 Reliability of MEMS packaging: vacuum maintenance and packaging induced stress *Microsys. Technol.* **11** 1187-96.

[98] Hositrad, Hoevelaken, The Netherlands, ⟨http://www.hositrad.com⟩.

[99] Welch K M 2003 Major advances in capture pumps in the last 50 years *J. Vac. Sci. Technol. A* **21** S19-24.

[100] Gupta A K and Leck J H 1975 An evaluation of the titanium sublimation pump *Vacuum* **25** 362-72.

[101] Ferrario B, Figini A and Borghi M 1985 A new generation of porous non-evaporable getters *Vacuum* **35** 13-7.

[102] Lafferty J M 1998 *Foundations of Vacuum Science and Technology* (New York: Wiley), p.275-97.

[103] O'Hanlon J F 2003 *A User's Guide to Vacuum Technology* (New York: Wiley), p.247-61.

[104] Barosi A Gettering structure, US3926832 (1975).

[105] Barosi A and Giorgi T A 1973 A non-evaporable getter for low temperatures *Vacuum* **23** 15-9.

[106] Park C D, Chung S M and Manini P 2011 Combination of compact nonevaporable getter and small ion pumps for ultrahigh vacuum systems *J. Vac. Sci. Technol. A* **29** 011012.

[107] MKS Instruments, HPS Products, Boulder, USA, ⟨http://www.mksinst.com⟩.

[108] Saes Pure Gas Inc., San Luis Obispo, USA, ⟨http://www.saespuregas.com⟩.

[109] Tuzi Y, Tanaka T, Takeuchi K and Saito Y 1996 Effect of surface treatment on the adsorption kinetics of water vapor in a vacuum chamber *Vacuum* **47** 705-8.

[110] Shiokawa Y and Ichikawa M 1998 Measurement and control of sticking probability of H_2O on stainless steel surfaces *J. Vac. Sci. Technol. A* **16** 1131-6.

[111] Cao H S, Holland H J, Vermeer C H, Vanapalli S, Lerou P P P M, Blom M and ter Brake H J M 2013 Characterization of a two-stage 30 K Joule-Thomson microcooler *J. Micromech. Microeng.* **23** 065022.

[112] Kosar A and Peles Y 2006 Thermal-hydraulic performance of MEMS-based pin fin heat sink *J. Heat Transfer* **128** 121-31.

[113] Metzger D E, Berry R A and Bronson J P 1982 Developing heat transfer in rectangular ducts with staggered arrays of short pin fins *J. Heat Transfer* **104** 700-6.

[114] Nakagawa S, Senda M, Kikkawa S, Wakasugi H and Hiraide A 1998 Heat transfer in channel flow around a rectangular cylinder *Heat Transfer Jpn. Res.* **27** 84-97.

[115] Li Q, Chen Z, Flechtner U and Warnecke H J 1998 Heat transfer and pressure drop characteristics in rectangular channels with elliptic pin fins *Int. J. Heat Fluid Flow* **19** 245-50.

[116] Jeng T M 2006 Thermal performance of in-line diamond-shaped pin fins in a rectangular duct *Int. Commun. Heat Mass* **33** 1139-46.

[117] Jeng T M and Tzeng S C 2007 Pressure drop and heat transfer of square pin-fin arrays in in-line and staggered arrangements *Int. J. Heat Mass Transfer* **50** 2364-75.

[118] Poulikakos D and Bejan A 1982 Fin geometry for minimum entropy generation in forced convection *J. Heat Transfer* **104** 616-23.

[119] Khan W A Culham J R and Yovanovich M M 2005 Optimization of pin-fin heat sinks using entropy generation minimization *Trans. Comp. Packag. Technol.* **28** 247-54.

[120] Khan W A, Culham J R and Yovanovich M M 2006 The role of fin geometry in heat sink performance *J. Electron. Packaging* **128** 324-30.

[121] Park K, Choi D H and Lee K S 2004 Numerical shape optimization for high performance of a heat sink with pin-fins *Numer. Heat Transfer, Part A* **46** 909-27.

[122] ANSYS, Canonsburg, USA, ⟨http://www.ansys.com⟩.

[123] Valencia A 1995 Heat transfer enhancement in a channel with a built-in rectangular cylinder *Heat Mass Transfer* **30** 423-7.

[124] Derking J H, Zalewski D W, Garcia M, Holland H J, Mudaliar A V, Cao H S, Lerou P P P M and ter Brake H J M 2011 Progress in Joule-Thomson microcooling at the University of Twente *Cryocoolers* **16** 463-71.

[125] Warren S G, Brandt R E and Grenfell T C 2006 Visible and near-ultraviolet absorption spectrum of ice from transmission of solar radiation into snow *Appl. Optics* **45** 5320-34.

[126] Mary T A, Evans J S O, Vogt T and Sleight A W 1996 Negative thermal expansion from 0.3 to 1050 Kelvin in ZrW_2O_8 *Science* **272** 90-2.

[127] Grima J N, Oliveri L, Ellul B, Gatt R, Attard D, Cicala G and Recca G 2010 Adjustable and negative thermal expansion from multilayered systems *Phys. Status Solidi Rapid Res. Lett.* **4** 133-5.

[128] Maytal B Z 2010 Open cycle Joule-Thomson cryocooling by mixed coolant *Cryocoolers* **16** 489-95.

[129] Sobel L Mixed gas refrigerant system for sensor cooling below 80 K, US20070209371 A1 (2007).

Summary

For many electronic devices, colder is better. At lower temperatures, electronic devices such as infrared detectors and low-noise amplifiers (LNAs) operate with a higher signal-to-noise ratio and better overall performance than they do at room temperature. Superconducting devices such as superconducting quantum interference devices (SQUIDs) need extremely cold temperatures to operate. However, existing cryogenic coolers are very large compared to sizes of these devices to be cooled and mismatch the small cooling power requirements of these devices. In order to allow more widespread use of these electronic devices, micro-sized cryogenic coolers need to become cheaper and more reliable. Addressing this challenge, this thesis focuses on the design, optimization and fabrication of a 30 K (-243 °C) micro-sized cryocooler. The microcooler is fabricated using only micromachining technology. This technology offers high fabrication accuracy and the possibility of batch processing, which opens the opportunity to mass production. Besides, the electronic devices to be cooled could be easily integrated with the microcooler production process.

In the microcooler, refrigeration is obtained by the Joule-Thomson (JT) effect through the expansion of high-pressure gas over a flow restriction. The gas may be cooled to such a low temperature that it liquefies and the liquid can cool the electronic device mounted on the cold end. However, cooling only occurs if the temperature of the gas, prior to JT-expansion, is below its so-called inversion temperature. A temperature of 30 K can be reached by using hydrogen or neon gas as the working fluid, but their inversion temperatures are lower than ambient temperature. Therefore, it is necessary to use a two-stage microcooler in which hydrogen or neon gas is precooled to a temperature below

their inversion temperatures using a JT stage operating with a gas of which the inversion temperature is above ambient temperature. By maximizing the coefficient of performance of the two-stage microcooler, hydrogen gas is selected as the optimum working fluid for the stage reaching 30 K and nitrogen gas as that for the precooling stage.

In the design, the microcooler consists of a stack of only three glass wafers in which microstructures are etched. Compared to earlier seven-wafer-stack designs, this substantially improves the fabrication yield of two-stage microcoolers. The evaporator of the nitrogen stage is a meandering channel in which the liquid nitrogen that is produced exchanges heat with part of the hydrogen-stage counter flow heat exchanger (CFHX). The dimensions of the microcooler are optimized based on a trade-off between fluidic and thermal losses. Parasitic losses due to heat conduction from ambient to the cold parts, thermal radiation on the cold surface, and pressure drop due to gas flow in the channels are considered in designing the microcooler. Considering all the above losses, the dimensions of the CFHXs and restrictions are optimized. The overall dimensions of the microcooler are 90.0 x 20.4 x 0.72 mm^3. The height of the gas channels in the CFHX is 40 μm. The restrictions of the nitrogen and hydrogen stages consist of 21 and 10 parallel rectangular slits, respectively, with a height of 1.1 μm.

The microcooler is fabricated by etching microstructures in glass wafers that are later stacked and bonded together. Separate microcoolers are obtained by dicing the bonded wafers. This approach allows the fabrication of many such microcoolers at low cost. A 0.2 μm layer of gold is deposited on the microcooler to increase the reflectivity of the surface thereby lowering the thermal radiation heat load on the microcooler.

The application potential of the microcooler coupled with electronic devices has been demonstrated by cooling an yttrium barium copper oxide (YBCO) film through its superconducting phase transition. The nitrogen and hydrogen stages cool down to about 94 and 30 K, respectively. The nitrogen stage is typically operated at a low-pressure of 0.11 MPa and a high-pressure of 8.5 MPa. The hydrogen stage has a low pressure of 0.57 MPa, whereas the high pressure is varied between 4.5 and 6.0 MPa. In changing the pressure settings, the cooling power can more or less be exchanged between the two stages. These typically range from 21 to 84 mW at 95 K at the nitrogen stage, corresponding to 30 to 5 mW at 31-32 K at the hydrogen stage.

A major hurdle in the long-term operation of the microcooler is the clogging of the nitrogen stage caused by the deposition of water that is present as impurity in the nitrogen gas. By using a single-stage microcooler operating with nitrogen gas, the mechanism of clogging is investigated through experimental observation and theoretical analysis. It is found that the position and the rate of the deposition of water molecules in the single-stage microcooler mainly depend on the inlet partial pressure of water and the temperature profile along the single-stage microcooler. By using a getter filter, most impurities (especially water) from nitrogen gas are removed to a minimum value of about 1.0 parts per billion (ppb). By changing the temperature profile along the single-stage microcooler using a high-thermal conductivity silicon piece, the operating time of a

single-stage microcooler under test at 105 K could be increased by a factor of 5.

The performance of an antenna system can be improved by cooling the LNA stage in order to reduce the noise figure. Cooling the LNA locally can decrease the noise figure with low cooling power since not the whole system has to be cooled. Localized LNA cooling using a single-stage microcooler has been demonstrated. The noise figure of the LNA under study drops by about 0.33 dB from 0.83 to 0.50 dB in the frequency range between 0.65 and 1.05 GHz with its operating temperature decreasing from 295 to 115 K. Due to the decreasing operating temperature, the gain improvement varies in the range of 0.6 to 1.5 dB, dependent on the frequency. The length of radio frequency (RF) lines along the printed circuit board (PCB) should be further reduced in order to decrease the loss before the LNA and therefore the noise figure.

The microcooler requires a vacuum environment to reduce the parasitic loss that is due to the heat flow from the warm environment via the surrounding gas. The possible sources of gas, the evolution mechanisms and their corresponding effects on the vacuum pressure have been discussed theoretically. Experimental results show that the pressure inside a test chamber (volume $3.6{\cdot}10^{-5}$ m^3 and inner area $8.1{\cdot}10^{-3}$ m^2) with a getter can stay below about 0.05 Pa for at least 2 years. Combining theoretical analysis and experiment reveals that it is necessary to reduce the monolayer chemisorbed water on the chamber surface and hydrogen dissolved in the chamber wall through a baking process for a stainless steel chamber. For a glass chamber, a helium gas permeation barrier such as titanium coating is essential.

Counter flow heat exchangers (CFHXs) are crucial elements for JT microcoolers. The thermal and hydraulic performance of the high- and low-pressure channels of CFHXs with pillar matrices are investigated numerically for different patterns. The correlations of the Nusselt number and the Darcy-Weisbach friction factor in the channels with different pillar patterns are obtained from numerical simulation. The resulting correlations can be used for predicting the performance of a microcooler. It is found that the microcooler performance can be improved by replacing the aligned pillar array in the high-pressure channel with a staggered pillar array.

Samenvatting

Voor veel elektronica geldt: kouder is beter. Bij een lagere temperatuur hebben elektronische instrumenten zoals infrarood detectoren en ruisarme versterkers een hogere signaal-ruisverhouding en presteren ze beter dan bij kamertemperatuur. Supergeleidende elektronische instrumenten zoals “Superconducting Quantum Interference Devices”-(SQUIDs) hebben, om te kunnen werken, een extreem lage temperatuur nodig. Bestaande cryogene koelers zijn echter veel te groot in afmetingen en in koelvermogen voor deze te koelen elektronica. Om een brede toepassing van gekoelde elektronica mogelijk te maken is het nodig dat kleine cryogene koelers goedkoper en betrouwbaarder worden. Dit proefschrift gaat deze uitdaging aan en focust op het ontwerp, de optimalisatie en de fabricatie van een 30 K (-243 °C) micro cryokoeler. In de fabricage van deze microkoeler is alleen gebruik gemaakt van micromechanische productie technologie. Deze technologie biedt behalve een hoge precisie ook de mogelijkheid van serieproductie, hetgeen de weg opent naar massaproductie. Bovendien kunnen de elektronische instrumenten die gekoeld moeten worden gemakkelijk worden gentegreerd met het productieproces van de microkoeler.

De werking van de microkoeler berust op het Joule-Thomson effect: de expansie van een hogedruk gas over een stromingsweerstand: de JT-restrictie. Het gas kan hierbij zover afkoelen dat het vloeibaar wordt. Deze vloeistof koelt de elektronische component, die gemonteerd wordt op het koude uiteinde. Dit koeleffect treedt echter alleen op als de temperatuur van het gas, voordat het expandeert, onder de zogenaamde inversietemperatuur ligt. Een temperatuur van 30 K kan worden gehaald met waterstof- of neongas als werkgas, maar hun inversietemperaturen liggen onder kamertemperatuur.

Daarom is het noodzakelijk om een tweetraps microkoeler te gebruiken. Hierin wordt de waterstof of neon eerst voorgekoeld naar een temperatuur beneden de inversietemperatuur, met een ander gas waarvan de inversietemperatuur boven kamertemperatuur ligt. Voor een maximale efficiëntie van de tweetraps microkoeler is waterstofgas geselecteerd als werkgas voor de 30 K trap en stikstofgas voor de voorkoeltrap.

De microkoeler is opgebouwd uit slechts 3 glasplaatjes waarin microstructuren zijn geëtst. Vergeleken met eerdere 7-laags ontwerpen voor tweetraps microkoelers, verbetert dit ontwerp de productie opbrengst substantieel. De verdamper van de stikstof trap is een meanderend kanaal waarin de geproduceerde vloeibare stikstof warmte uitwisselt met een deel van de waterstof tegenstroomwarmtewisselaar. De afmetingen van de microkoeler zijn geoptimaliseerd, waarbij de som van de thermische en hydraulische verliezen geminimaliseerd is. Ook parasitaire verliezen -de warmtegeleiding van kamertemperatuur naar de koude zijde, de warmtestraling naar het koude oppervlak en de drukval door de gasstromen in de kanalen- zijn meegenomen in het ontwerp van de koeler. Vanuit deze genoemde verliezen zijn de optimale afmetingen van zowel de tegenstroomwarmtewisselaar als de JT restricties bepaald. De afmetingen van de microkoeler zijn 90.0 x 20.4 x 0.72 mm^3 en de hoogte van de geëtste gaskanalen is 40 μm. De stromingsweerstanden van de stikstof en waterstof trap bevatten respectievelijk 21 en 10 parallelle rechthoekige nauwe kanalen met een hoogte van 1.1 μm.

Voor de productie van de microkoeler zijn de microstructuren chemisch geëtst in de drie glasplaatjes en vervolgens op elkaar gebond. Separate microkoelers worden verkregen door de glaswafer te zagen. Deze aanpak maakt de productie van veel van deze microkoelers mogelijk tegen lage kosten. Een 0.2 μm dikke goudlaag is op de microkoeler aangebracht om de reflectie aan het oppervlak te vergroten en daarmee de thermische stralingsbelasting te beperken.

De toepassingsmogelijkheden van de microkoeler gekoppeld aan elektronische instrumenten is gedemonstreerd door een supergeleidende dunne laag yttrium-barium-koperoxide (YBCO) tot onder zijn kritische temperatuur te koelen. De stikstof- en waterstoftrap koelen respectievelijk tot ongeveer 94 K en 30 K. De lage druk van de stikstoftrap is gewoonlijk 0.11 MPa en voor de hoge druk zijde 8.5 MPa. De waterstof trap heeft een lage druk van 0.57 MPa, terwijl de hoge druk gevarieerd kan worden tussen 4.5 en 6.0 MPa. Door de druk te variëren, kan het koelvermogen min of meer tussen de twee trappen worden uitgewisseld. Het koelvermogen van de stikstoftrap ligt hierbij tussen 21 en 84 mW bij 95 K, corresponderend met 30 tot 5 mW bij 31-32 K voor de waterstoftrap.

Een belangrijk obstakel bij het langdurig koud houden van een microkoeler is het verstopt raken van de stikstoftrap door het vastvriezen van water, dat aanwezig is als verontreiniging in het stikstofgas. Door gebruik te maken van een ééntraps koeler, werkend op stikstofgas, is het mechanisme van verstopping onderzocht met experimentele observaties en theoretische analyses. Het blijkt dat de locatie en de depositiesnelheid van watermoleculen in een ééntraps koeler met name afhangt van de partiële druk

van water aan de inlaatzijde en het temperatuursprofiel in de ééntraps microkoeler. Met behulp van een getterfilter zijn de verontreinigingen, met name water, in het stikstofgas geminimaliseerd tot een niveau van 1 deeltje per miljard gasdeeltjes. Door het temperatuursprofiel in de ééntraps koeler te veranderen met behulp van een zeer goed thermische geleidend silicium schijfje kon de werkingsduur van een ééntraps koeler, bij 105 K, met een factor 5 verlengd worden.

De signaal-ruis verhouding van een antenne systeem kan worden verbeterd door een ruisarme versterker te koelen. Door alleen de ruisarme versterker te koelen kan dit met een laag koelvermogen aangezien niet het gehele systeem afgekoeld hoeft te worden. Het lokaal koelen van de ruisarme versterker is gedemonstreerd met een ééntraps microkoeler. Het ruisgetal van de geteste ruisarme versterker daalt met 0.33 dB van 0.83 naar 0.50 dB in het frequentiegebied van 0.65 tot 1.05 GHz als zijn temperatuur daalt van 295 naar 115 K. Dankzij de lagere temperatuur kan een versterkingsverbetering worden bereikt variërend van 0.6 tot 1.5 dB, afhankelijk van de frequentie. De lengte van de hoogfrequente lijnen op de printplaat kan verder worden geoptimaliseerd zodat de verliezen voor de ruisarme versterker, en daarbij het ruisgetal, verder kunnen worden gereduceerd.

De microkoeler vereist een vacuüm omgeving waardoor de parasitaire verliezen, door warmtestromen van de warme omgeving via het omringende gas, worden verminderd. De mogelijke bronnen van dit gas, de druk-opbouw mechanismen en het bijbehorende effect op de vacuümdruk zijn theoretisch behandeld. Experimentele resultaten wijzen uit dat de druk in een vacuümkamer (volume $3.6{\cdot}10^{-5}$ m^3 en inwendig oppervlak $8.1{\cdot}10^{-3}$ m^2) met een getter onder 0.05 Pa kan blijven voor minimaal 2 jaar. Door de theoretische analyse en experimentele resultaten te combineren blijkt dat het voor roestvrijstaal nodig is om zowel de monolaag chemisch gebonden water op het oppervlak als de waterstof opgenomen in het roestvrijstaal van de vacuümkamer sterk te reduceren via een uitstookproces. Bij glazen vacuümkamers is een barrire voor heliumgaspermeatie essentieel, bijvoorbeeld door een dunne laag titanium aan te brengen.

Tegenstroomwarmtewisselaars zijn cruciale elementen voor Joule-Thomson microkoelers. Het thermische en hydraulische gedrag van de hoge- en lagedruk kanalen van de tegenstroomwarmtewisselaars met daarin een patroon met steunpilaren zijn numeriek onderzocht voor verschillende patronen. De correlaties tussen het Nusselt getal en de Darcy-Weisbach frictiefactor zijn voor de verschillende pilaarpatronen bepaald met behulp van numerieke simulaties. Deze correlaties kunnen worden gebruikt om de prestatie van een microkoeler te voorspellen. Uit de analyse blijkt dat de efficiëntie van de microkoeler verder kan worden verbeterd door het uitgelijnde pilaren patroon in het hoge-druk kanaal te vervangen door een verspringend patroon.

List of publications

Journal Papers

Cao H S, Witvers R H, Vanapalli S, Holland H J and ter Brake H J M, Cooling a low noise amplifier with a micromachined cryogenic cooler, accepted for publication in *Rev. Sci. Instrum.*

Cao H S, Vanapalli S, Holland H J, Vermeer C H and ter Brake H J M 2013 Clogging in micromachined Joule-Thomson coolers: mechanism and preventive measures *Appl. Phys. Lett.* **103** 034107.

Cao H S, Holland H J, Vermeer C H, Vanapalli S, Lerou P P P M, Blom M and ter Brake H J M 2013 Characterization of a two-stage 30 K JouleThomson microcooler *J. Micromech. Microeng.* **23** 065022.

Cao H S, Holland H J, Vermeer C H, Vanapalli S, Lerou P P P M, Blom M and ter Brake H J M 2013 Micromachined cryogenic cooler for cooling electronic devices down to 30 K *J. Micromech. Microeng.* **23** 025014.

Cao H S, Mudaliar A V, Derking J H, Lerou P P P M, Holland H J, Zalewski D R, Vanapalli S and ter Brake H J M 2012 Design and optimization of a two-stage 28 K Joule-Thomson microcooler *Cryogenics* **52** 51-7.

Conference Papers

Cao H S, Derking J H, Holland H J, Zalewski D R, Vermeer C H, Vanapalli S, Lerou P P P M, Tirolien T, Crook, M R and ter Brake H J M 2012 Two stage pure gas and single stage mixture gas microcooler developments at University of Twente, *Cryocoolers* **17** 371-6.

ter Brake H J M, Cao H S, Derking J H, Holland H J, Zalewski D R, Vermeer C H, Vanapalli S, Lerou P P P M, Tirolien T and Crook, M R 2012 Two-stage and mixed-gas single-stage microcooler developments, In: Proceedings ICEC 24-ICMC, Fukuoka, Japan, p. 319-24.

Cao H S, Lerou P P P M, Mudaliar A V, Holland H J, Derking J H, Zalewski D R and ter Brake H J M 2011 Analysis of multi-stage Joule-Thomson microcoolers, *Cryocoolers* **16** 481-7.

ter Brake H J M, Derking J H, Cao H S, Holland H J, Garcia M, Mudaliar A V and Lerou P P P M 2010 Microcooling developments at the University of Twente, In: Proceedings ICEC 23-ICMC, Wroclaw, Poland, p. 67-72.

Manuscripts

Cao H S, Vermeer C H, Vanapalli S, Holland H J and ter Brake H J M, A long-life micro vacuum chamber for a micromachinned cryogenic cooler, in preparation.

Acknowledgements

The word ‘cryogenics’ was proposed by a Dutch physicist and Nobel prize winner Kamerlingh Onnes from the Greek words ‘kryos’ meaning ‘frost’ and ‘genic’ meaning ‘to produce’. It is my honor to have this unique opportunity to do research in the field of cryogenics in the Netherlands. The work described in this thesis takes almost four years to complete. It could easily take another four years without the help and encouragement of many people whom I would like to express our heartfelt gratitude to.

My gratitude, first and foremost, goes to my promoter, Prof. Marcel ter Brake, who offers me the opportunity to pursue my PhD study in the Energy, Materials and Systems group (EMS). During the PhD study, we had regular meetings and you gave me continuous advice and support, which are invaluable to me. Marcel, you always encourage me to try new things and give me lots of confidence. When I presented our two-stage microcooler at the Dutch Technology Foundation (STW) Annual Congress in 2012, you emailed me from Portland the following words: “*Do not be too humble, you are doing a great job and the microcoolers have a bright future and you need to make people aware of that.*” This makes me more confident not only at the congress but also in other public places.

I would also like to thank my assistant promoter, Dr. Srinivas Vanapalli. Srini, you spend a lot of time on correcting my papers, and I learn a lot from your comments. You advise me to attend more conferences and summer schools to widen my vision, broaden my mind and improve my communicative skills, which I highly appreciate.

I am grateful to Harry Holland and Cris Vermeer. Harry, I enjoy the time with you, not only the leisure time in New York, but also the working time in the lab. Thanks for

your help with my experiments and for the discussions we have on microcooling. Cris, you visit more famous cities in China than I do. However, I visited the Dutch windmill village, Zaanse Schans, where you have never been. I greatly appreciate your help in realizing the two-stage microcooler characterization set-up.

I would like to thank Pieter Lerou, Ashvin mudaliar and Hendrie Derking. Pieter, thanks for sharing your knowledge and experience in developing the single-stage microcooler. Ashvin, thanks for your help and advice when I developed the two-stage microcooler dynamic model in the first year of my PhD study. Hendrie, thanks for your assistance in the two-stage microcooler characterization experiments.

Thanks to Marko Blom, Gunter Venhorst, Jeroen Haneveld, Bastiaan Janssen, Peter Tijssen of Micronit, for your help during the fabrication of the two-stage microcooler.

Thanks to several people of the Interfaces and Correlated Electron systems group (ICE) at University of Twente, Hans Hilgenkamp and Frank Roesthuis for providing YBCO films and discussions on resistance measurements; Dick Veldhuis for showing me how to use the thermosonic bonding machine.

Thanks to Roel Witvers of Astron for the discussions we had on the localized low-noise amplifier cooling using a microcooler.

Thanks to Dhirendra Tiwari of the Physics of Complex Fluids group (PCF) at University of Twente, for providing assistance in imaging the clogging phenomenon in microcoolers.

Working in EMS group is enjoyable because of all the friendly members. Here I would like to thank Marc, Arend, Hennie, Sander, Ruben, Rutger, Harrie, Erik, Konstantyn, Wilco, Gonzalo, Gabriella, Edwin, Tim, Tymen and Bram for the enjoyable leisure time in the social corner and the fruitful discussions at the fortnightly colloquium. I would also like to thank former members of EMS group, Johannes, Dawid, Robert Jan for all your help.

I am grateful to our secretaries Ans and Inke, who always offer kind and timely assistance in arranging many things during my time in EMS group.

Apart from my research life on campus, the friends I met in Enschede make my daily life much easier and happier. I met WangMeng, WeiHua and QiWei when I was dragging my luggage at the roadside around ten o'clock on the first night when I arrived at Enschede. You picked me up and took me to Logica. I met XiaoFeng and LiXian on that night, and you shared your experience at University of Twente. I met CuiYang (special to me), TakShing, LvSheng, DanChao and XinFu when I lived in Macandra. We prepared dinner together, had barbecue at Ruthbeek Lake, played basketball in Volkspark, etc. Thanks you guys for sharing so many happy moments with me, especially in stressful time of the first two years of my PhD study. TakShing, I admire your lifestyle and attitude towards life. I wish you enjoy your life in your physics and painting world. DanChao and XinFu, may your family have a peaceful and happy life. I lived alone in Macandra for a while after you all graduated and left. Then, a funny guy, WangZhao, came into my life. We went to open market and played basketball almost every Saturday. WangZhao, I wish

you complete your postgraduate study smoothly and then enjoy your life with BianCe when you return to China. Through you, I can get together regularly with WanShu, WangLei, FangWei and Michel. I will miss you guys and the amazing food you made.

Thanks to my 'lunch partners' YingZhe, LiuLi, ZhouChao and GaoPeng, we often have lunch together after we move to Carré. During the lunch time, we talk about various issues in China. Sometimes, we argue with each other on some issues but we do hope our compatriot living in China can have a better life.

I would also like to thank TakShing's roomates: YiHan, XiaoChen and QiaoYu for organizing so many parties and making lots of delicious food. Many thanks also go to ZhouJie, XiaoLin, GongZheng, XuNing, XiuLi, YingYing, Rena, XiaoYan, Mehran, Aga, Avijit, XiaoKui, DongShuang, BinLong, TaoYin, MaSong, JinPeng, YangHuan, LuZhou, JianFeng and many others. We had a wonderful time together and I wish you guys a bright future full of peace and prosperity.

I am greatly indebted to my parents Cao ZhenXin and Li ZuoHua, and my younger sister Cao LiJuan, for your love, constant support and patience for all these years. Last but not least, I am deeply grateful to my girlfriend CuiYang for your love, smile  , patience and encouragement. I hope we can have a future that is beautiful and exciting as you imagine.

Haishan Cao
Enschede 2013

About the Author

Haishan Cao was born on 09 November 1981, in Inner Mongolia, China. After graduating from high school in Chifeng, he entered Zhejiang University in 2002. In 2006, he obtained his Bachelor of Science degree in Chemical Engineering with the award of excellent graduation thesis. After his graduation, he was recommended for admission to be a postgraduate at Dalian Institute of Chemical Physics, Chinese Academy of Sciences. His Master's research focused on the design of microchannel heat exchangers. In 2009, he obtained his Master of Science degree in Chemical Engineering under the supervision of Prof. Guangwen Chen and Prof. Quan Yuan. In September 2009, he joined the Energy, Materials and Systems group at University of Twente, the Netherlands, as a PhD student under the supervision of Prof. Marcel ter Brake. His PhD research subject is Joule-Thomson (JT) cooling for low-temperature electronic devices. The main activities include: two-stage 30 K JT microcooler design, microcooler utilization in cooling superconducting devices and low-noise amplifiers, mechanism of clogging phenomenon in microcoolers, and vacuum packaging for microcoolers. The results of this four year doctoral research are described in this thesis.

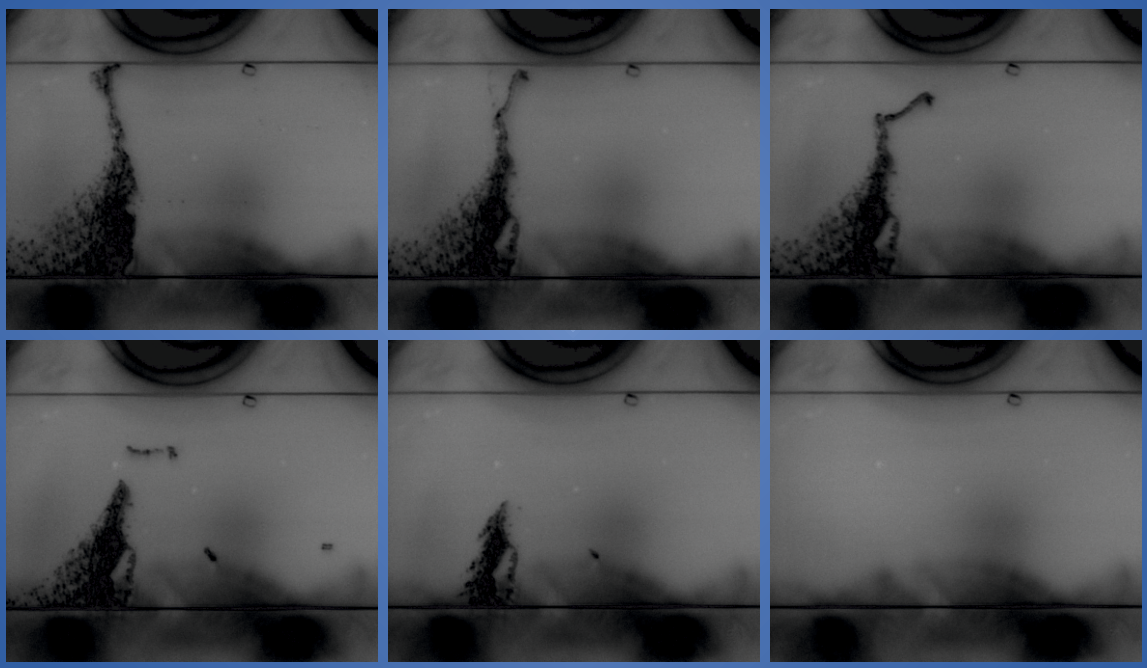

ISBN: 978-90-365-0139-2